Dehydrogenation of methanol to formaldehyde using sodium-based catalysts on a mini-plant scale

Zur Erlangung des akademischen Grades einer

DOKTORIN DER INGENIEURWISSENSCHAFTEN

von der KIT-Fakultät für Chemieingenieurwesen und Verfahrenstechnik des Karlsruher Instituts für Technologie (KIT)
genehmigte

DISSERTATION

von
M.Sc. Marta Kamienowska-Orsini
aus Sosnowiec, Polen

Tag der mündlichen Prüfung: 30.06.2025

Erstgutachter: Prof. Dr.-Ing. Thomas Wetzel

Zweitgutachter: Prof. Dr.-Ing. Jörg Sauer

Dla śp. Aleksandry Turchan z domu Racibor

FOREWORDS

I would like to offer my sincere appreciation to all those who have contributed to the completion of this thesis.

I wish to express my deepest gratitude to Prof. Dr.-Ing. Thomas Wetzel, whose expert guidance and support were crucial throughout the development of this thesis. In addition, I am also sincerely thankful to Prof. Dr.-Ing. Jörg Sauer for his valuable co-supervision and constructive contributions. Furthermore, I extend my heartfelt appreciation to Dr.-Ing. Klarissa Niedermeier. Without her constant support and guidance, this dissertation would not have been possible. My profound thanks also go to Dr. Michael Bender for his significant involvement throughout this project. His expertise and invaluable input were instrumental in shaping both the direction and finalization of this thesis.

Ich bin all meinen Kollegen am Karlsruher Flüssigmetall-Labor für ihre Unterstützung und Freundschaft zutiefst dankbar. Insbesondere möchte ich Christopher Hofberger, Peter Miodek und Kurt Wittemann für ihre unschätzbare Hilfe im Laboralltag danken. I would also like to thank the entire team at the KIT Institute of Catalysis Research and Technology (IKFT) for their support and fruitful scientific discussions. Special thanks go to the team at KIT Technik-Haus, especially Daniel Kuntz and Joachim Konrad, for their technical expertise throughout the project. I would like to thank Vanessa Trouillet (KIT Institute for Applied Materials) for the XPS measurements, analysis and constructive discussion of the results.

I would like to acknowledge Max Deutschmann, Estelle Emig and Damian Mertens for their exceptional and diligent student research contributions, which greatly facilitated the preparation of this thesis.

Chciałabym wyrazić moją głęboką wdzięczność dla mojej rodziny, zwłaszcza dla rodziców i dziadków, za ich bezcenne wsparcie na każdym kroku mojej ścieżki naukowej.

Vorrei ringraziare mio marito per il suo infinito sostegno e comprensione durante il mio lavoro di dottorato.

KURZFASSUNG

Formaldehyd, einer der wichtigsten Rohstoffe der chemischen Industrie, kann durch verschiedene Verfahren hergestellt werden die sich in ihrer Effizienz und den damit verbundenen Herausforderungen unterscheiden. Die vorgestellte Dissertation untersucht eine dieser Methoden im Detail: die Dehydrierung von Methanol zu Formaldehyd in der Gasphase. Der Schwerpunkt dieser Arbeit liegt auf dem katalytischen Potenzial von Natrium und Natriumcarbonat. Darüber hinaus wird der Stand der Technik der Formaldehydproduktion zusammengefasst und die Notwendigkeit innovativer Ansätze zur Deckung des wachsenden Bedarfs unter zunehmenden Umweltschutzanforderungen hervorgehoben.

Kern dieser Arbeit ist ein speziell entwickelter und konstruierter Versuchsaufbau, die MEDENA-Anlage. Diese ermöglichte die Durchführung von Experimenten und lieferte wichtige Erkenntnisse über das Verhalten von Substraten, Produkten und Katalysatoren. Als Katalysatoren wurden Natriumdampf und Natriumcarbonat für die direkte Dehydrierung von Methanol zu Formaldehyd untersucht. Besonderes Augenmerk lag auf dem Dosiersystem für den Natriumdampf, welches erfolgreich in Betrieb genommen wurde und zeigte, dass der Einsatz von Natrium hohe Formaldehyd- und Wasserstoffausbeuten ermöglicht.

Zusätzlich wurde für diese Reaktion eine neuartige Beheizungstechnik untersucht. Im Gegensatz zu herkömmlichen Heizmethoden, welche indirekt oder konvektive Wärme in den Katalysator übertragen, wird bei der neu untersuchten Technik der Katalysatorkörper gleichzeitig als Widerstandsheizer eingesetzt und somit direkt beheizt. Hierbei wird elektrischer Strom durch den Katalysatorkörper geleitet, was eine schnelle und gleichmäßige Erwärmung des Katalysatorbetts gewährleistet, Wärmeverluste minimiert und optimale Reaktionsbedingungen schafft. Die dadurch erreichte hohe Effizienz führt sowohl zu wirtschaftlichen als auch zu ökologischen Vorteilen.

Insgesamt ist das Ziel dieser Forschung, die Lücke zwischen traditionellen Verfahren und neu entwickelten Methoden zu verkleinern. Diese Arbeit ebnet den Weg für eine umweltfreundliche, effiziente und nachhaltige Formaldehyd-Produktion.

ABSTRACT

Formaldehyde, an important chemical precursor in many industrial processes, is produced by various methods, each with their own efficiency and challenges. The presented thesis provides an in-depth investigation of the gas-phase dehydrogenation of methanol to formaldehyde, focusing on the potential of sodium compounds, particularly sodium and sodium carbonate, as catalysts. Furthermore, it presents the state of the art in formaldehyde production, highlighting the need for innovative approaches to meet growing industrial demands and increased environmental concerns.

A specially designed and constructed experimental setup, the MEDENA mini-plant, is at the center of this thesis, allowing reaction tests to be carried out and providing important insights into the behavior of substrates, products, and catalysts. Sodium metal and sodium carbonate were studied as catalysts for the direct dehydrogenation of methanol to formaldehyde. Additionally, particular attention was given to the evaluation of the sodium dosing system. The results indicated that sodium vapor can be dosed continuously while at the same time, obtaining high formaldehyde and hydrogen yields.

Moreover, a novel heating method for the dehydrogenation of methanol to formaldehyde was examined. Unlike traditional heating techniques, which often employ indirect or convective heat transfer, direct resistance heating applies electrical current through the catalyst body. This direct approach ensures rapid and uniform heating, minimizing potential heat losses and ensuring the most favorable reaction conditions. Due to its efficiency, the direct resistance heating concept has the potential to transform conventional methods of formaldehyde production, offering both economic and environmental benefits.

In summary, this research aimed to improve formaldehyde production techniques by bridging the gap between conventional routes and newly developed approaches. This work paves the way for environmentally friendly, efficient and sustainable formaldehyde production, thereby preparing the ground for future industrial applications.

TABLE OF CONTENTS

NOMENCLATURE

Latin Symbol	Unit	Definition
A	m^2	Area
C	$mol\ m^{-3}$	Molar concentration
c_p	$J\ kg^{-1}\ K^{-1}$	Specific heat capacity
D	$m^2\ s^{-1}$	Diffusion coefficient
d	m	Diameter
E_A	$J\ mol^{-1}$	Activation energy
L	m	Length
k	$mol\ m^{-3}\ s^{-1}$	Rate coefficient of the process
$\tilde{M}$	$mol\ kg^{-1}$	Molar mass
$\dot{m}$	$kg\ s^{-1}$	Mass flow
N	mol	Amount of substance
$\dot{N}$	$mol\ h^{-1}$	Molar flow
n	$-$	Component n
P	W	Power
p	Pa	Pressure
$\dot{Q}$	W	Heat flow rate
r	m	Radius
S	$-$	Selectivity
T	$°C$	Temperature
t	s	Time
V	m^3	Volume
v	$m\ s^{-1}$	Velocity
w	$kg\ m^{-3}$	Mass concentration
X	$\%$	Conversion
x	$-$	Mole fraction of the component in the liquid phase
Y	$\%$	Yield
y	$-$	Mole fraction of the component in the gas phase

Greek Symbol	Unit	Definition
α	$\mathrm{W\,m^{-2}\,K^{-1}}$	Heat transfer coefficient
β	$\mathrm{1\,K^{-1}}$	Thermal expansion coefficient
β_{Diff}	$\mathrm{m\,s^{-1}}$	Diffusive mass transfer coefficient
δ	m	Diffusion path
Δ	$-$	Difference to a reference value
ε	$-$	Relative volume change
λ	$\mathrm{W\,m^{-1}\,K^{-1}}$	Thermal conductivity
μ	$\mathrm{kg\,m^{-1}\,s^{-1}}$	Dynamic viscosity
ν	$\mathrm{m^2\,s^{-1}}$	Kinematic viscosity
ν	$-$	Stoichiometric coefficient
ρ	$\mathrm{kg\,m^{-3}}$	Density
τ	$\mathrm{N\,m^{-1}}$	Surface tension
τ	s	Space time

Subscripts

Symbol	Definition
0	Starting point
A	Educt
Ar	Argon
B	Bubble
el	Electrical power
i	Component index
i	Inner
in	Inlet
mix	Mixture
Na	Sodium
O	Orifice
o	Outer
out	Outlet
P	Product
Ph	Phase

Abbreviations

Symbol	Definition
Cat	Catalyst
CSTR	Continuously stirred tank reactor
DRH	Direct resistance heating
FC	Flow controller
GC	Gas chromatograph
MEDENA	Methanol dehydrogenation to formaldehyde with sodium (Na)
MeOH	Methanol
NAMOSYN	Nachhaltige Mobilität durch synthetische Kraftstoffe
OGP	Off-gas purification
PC	Pressure controller
SEM	Scanning electron microscopy
XPS	X-ray photoelectron spectroscopy

Dimensionless quantities

Symbol	Definition
Eo	Eötvös Number
Fr	Froude Number
Mo	Morton Number
Nu	Nusselt Number
Re	Reynolds Number
We	Webber Number

Constants

Symbol	Value	Unit	Definition
g	9.810	$\mathrm{m\,s^{-2}}$	Gravity of Earth
$\mathrm{N_A}$	$6.022 \cdot 10^{23}$	$\mathrm{mol^{-1}}$	Avogadro's constant
R	8.314	$\mathrm{J\,mol^{-1}K^{-1}}$	Universal gas constant
π	3.142	-	Archimedes' constant

1. INTRODUCTION

Formaldehyde is one of the most predominant chemicals, which finds applications in more than 50 industrial sectors, mainly as aqueous solutions and formaldehyde-based resins. The demand for formaldehyde production has been growing steadily. In 2011, the global output was 31.4 million tons per year, rising to 46.6 million tons per year in 2022 and is estimated to reach 70.8 million tons per year in 2030 [1]. Industrially produced formaldehyde is in the form of an aqueous solution. Yet for many processes, it is advantageous to use highly concentrated gaseous formaldehyde, for example, in the production of diesel fuel substitutes, namely, polyoxymethylene dimethyl ethers (OMEn) or in the formation of polyacetal resins.

Efforts to limit global warming require a significant reduction in carbon dioxide (CO_2) emissions, of which the transportation sector contributes approximately 20% [2]. While electric vehicles offer a solution to CO_2 reduction in that sector, they are not feasible for all means of transport, such as trucks, planes and ships, which are more difficult to electrify. The NAMOSYN (*Nachhaltige Mobilität mit synthetischen Kraftstoffen*) research project is addressing this challenge [3]. The goal is to develop and test sustainable synthetic fuels for use in conventional engines. In this context, the development of green and synthetic fuels such as OMEn is crucial. This doctoral thesis was conducted within the framework of the NAMOSYN project, focusing on the development of anhydrous formaldehyde production, which is essential for synthesizing OMEn. One promising enhancement in this area is the application of sodium vapor as the catalyst, which shows the potential to increase the efficiency and selectivity of nonoxidative formaldehyde production. Within this work, the sodium dosing concept was developed and tested to further understand and optimize its role in the process.

In addition, the increasing electrification of the industry, caused by the more common use of renewable energy, will make the engineering of chemical reactions more important. Electrical energy can be introduced directly or indirectly as heat into reactors. Industrial applications include electrochemical energy storage, electrolysis, and both plasma and electrically heated reactors [4, 5]. Direct resistance heating (DRH) is a type of heating in which an electric current (DC or AC) flows directly into an

object to be heated. In terms of electrification of the chemical industry, the DRH concept seems to be a reasonable choice because it ensures high heating uniformity and the possibility of concentrating large thermal energy releases in a small area. With the aim of the production of water-free formaldehyde and valuable hydrogen by means of the DRH concept, a particular reactor concept was developed and implemented within this doctoral thesis.

1.1 Motivation

Recently, there has been a significant increase in the use of green energy sources as a means of meeting global CO_2 reduction targets [6]. In the area of renewable and environmentally friendly technologies, a great deal of attention has been given to innovative production methods of chemicals, among others, for formaldehyde, especially those that avoid energy-intensive processes. The use of DRH, which can be powered directly from green energy resources, is a promising route to sustainable formaldehyde production (Figure 1).

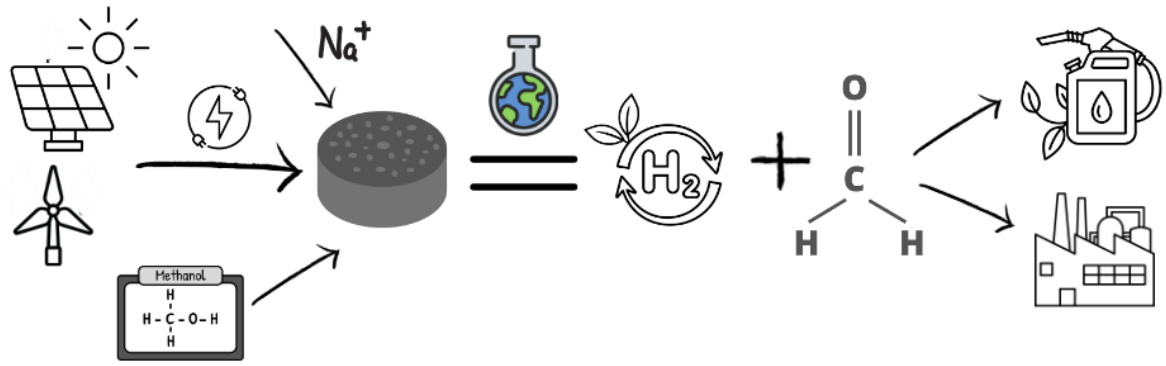

Figure 1. Graphical illustration of the research topic

In parallel with research on the DRH method, another potent approach was investigated: the use of sodium vapor as the catalyst for the direct dehydrogenation of methanol to formaldehyde. The motivation for this approach stems from the potential of sodium vapor to reduce the activation energy of the reaction, thereby increasing the yield and efficiency of formaldehyde production. In addition, sodium is widely available, inexpensive and could provide a commercially viable alternative to traditional catalysts, in line with the industry's drive towards sustainable solutions.

Over the years, there has been continuous interest in exploring alternative methods for the production of formaldehyde, due to its key role in various industries. One

promising approach that has attracted the attention of researchers is the direct dehydrogenation of methanol to anhydrous formaldehyde. While numerous studies have explored different process concepts and catalysts [7–12], sodium compounds have emerged as particularly advantageous catalysts for this reaction, as reported in several reports [13–17]. Despite this progress, a recurring problem is that many of the findings are based on laboratory-scale studies, leaving certain mechanical and engineering aspects of the process unresolved. The literature reveals a notable lack of detailed evaluations of sodium vapor catalysts, even in the context of mini-plant operations. The aim of this research is to explore in greater depth the challenges and intricacies associated with scaling up the sodium vapor catalyst dosing system, with the goal of creating fundamental principles for its potential implementation on an industrial scale. Furthermore, as the demand for formaldehyde continues to rise, there is a growing need to innovate and improve existing production processes. Thus, in addition to enhancing the sodium vapor concept, the DRH method, which employs a sodium carbonate catalyst, is proposed. To date, this technique has not been the subject of any research for anhydrous formaldehyde production, yet it aligns with current industry trends.

1.2 Research questions

In response to the growing demand for sustainable formaldehyde production methods, this thesis addresses the following research questions:

1. Effectiveness of sodium vapor as a catalyst
    - Can sodium metal vapor be used as a catalyst in the production of anhydrous formaldehyde at a mini-plant scale?
2. Prospect of using a direct resistance heating concept
    - Can direct resistance heating be used for the production of water-free formaldehyde at a mini-plant scale?
3. Suitability of impregnated ceramic sponges as catalyst bodies
    - Can impregnated ceramic sponges serve as effective catalyst bodies in the production of formaldehyde?

Essentially, the aim of this work is to evaluate the potential of sodium compounds as catalysts and to explore the feasibility of direct resistance heating as a means of improving the efficiency and scalability of anhydrous formaldehyde synthesis.

1.3 Research tasks

Based on the motivation discussed above, the following tasks were defined for this thesis:

- Completion of a comprehensive literature review and compare the findings with the existing knowledge in the field (Chapter 2 and Sections 5.3 & 6.7)
- Development of the alkali metal sodium dosage method (Section 3.1)
- Construction and testing of a pressureless apparatus for endothermic MeOH dehydrogenation using seed gas dosing of the alkali metal (Section 3.1 & 3.2)
- Design of a theoretical apparatus concept for the electrical heating of formaldehyde synthesis (Section 3.3)
- Selection of the most catalytically active species to optimize the reaction under the given conditions, as well as the development of a suitable reactor concept (Chapter 5 & 6)

In summary, the main aim of this doctoral thesis is to develop a method for anhydrous formaldehyde production using sodium compounds as catalysts at the mini-plant scale. For this purpose, the MEDENA (*Me*thanol *De*hydrogenation to Formaldehyde *with sodium Na*) mini-plant was designed, constructed and evaluated through testing. The outline of this thesis is shown in Figure 2.

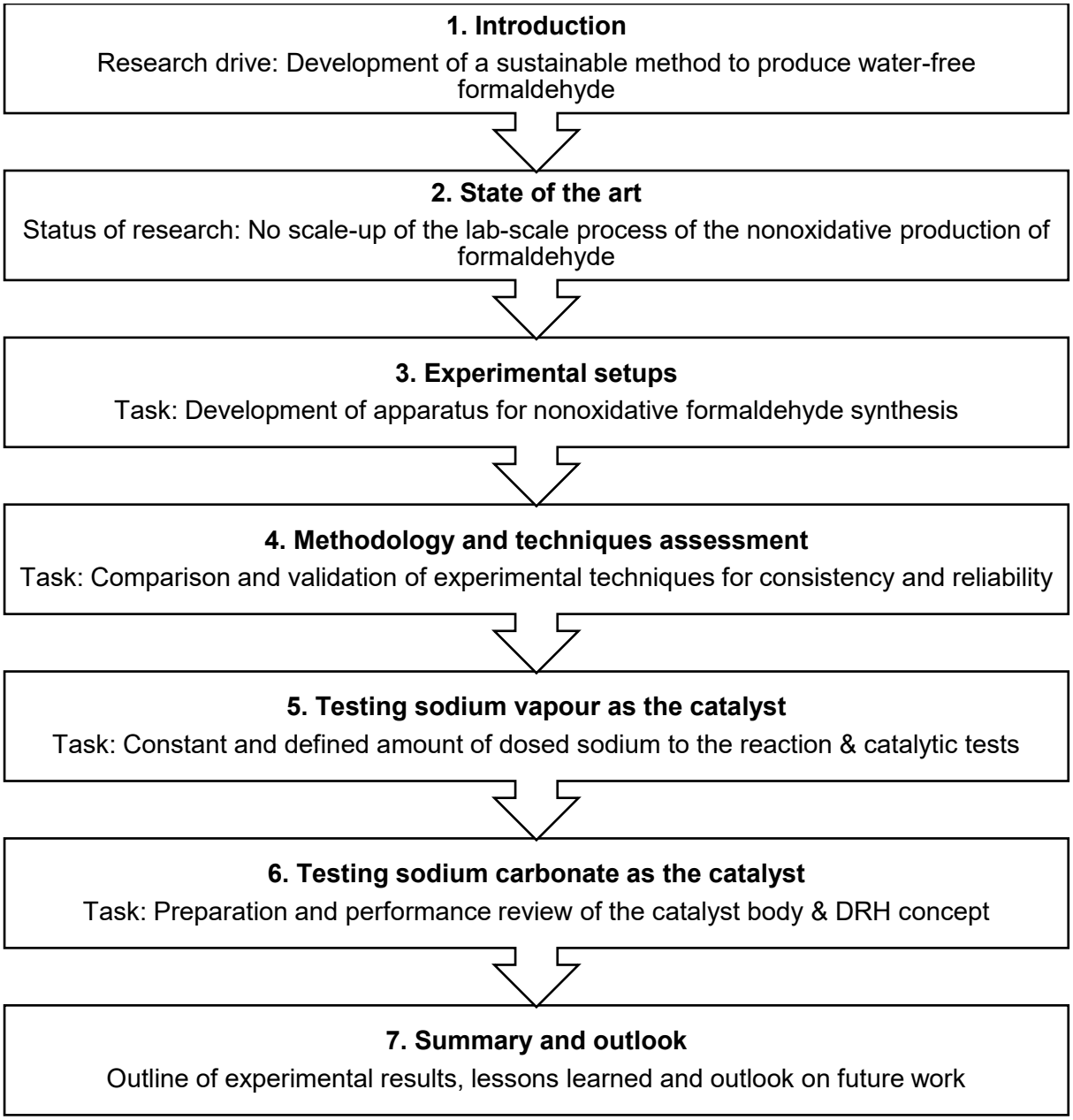

Figure 2. Overview of this doctoral thesis

2. STATE OF THE ART

This chapter provides a comprehensive overview of the current knowledge and developments relevant to the study of formaldehyde production and the role of sodium-based catalysts. It addresses various topics, starting with formaldehyde production methods, with particular emphasis on industrial-scale approaches and the direct dehydrogenation of methanol. Furthermore, the chapter discusses the behavior and applications of sodium in its various forms, including sodium vapor, sodium methoxide, sodium carbonate, and the important topic of sodium's corrosion behavior. Finally, the concept of direct resistance heating and the use of ceramic sponges in chemical processes are presented. Collectively, these sections form the foundation for understanding the experimental and theoretical approaches used in this work and provide insights into the utilization of sodium-based catalysts in the direct dehydrogenation of methanol to anhydrous formaldehyde.

2.1 Formaldehyde

Formaldehyde (CH_2O), in its monomeric state, is a colorless, toxic gas characterized by a pungent odor and flammability [18]. It is the simplest representative of the aldehyde group. Beyond its monomeric form, formaldehyde is known to exist in three other common forms. Formalin, the first of these, is an aqueous solution typically containing 37% by weight of formaldehyde, although concentrations can range from 30–55% by weight [19]. To prevent polymerization of formaldehyde and the formation of methylene glycol, up to 10% by weight of methanol is added to the solution as a stabilizer. Paraformaldehyde, the second form, is a polymer formed by the spontaneous polymerization of monomeric formaldehyde. It can be synthesized by the distillation of the aqueous solutions of formaldehyde and is a white crystalline solid. The third form, trioxane, is a cyclic trimer produced by the acid-catalyzed trimerization of aqueous formaldehyde solutions and is solid at room temperature [18]. Industrial formaldehyde production predominantly involves methanol as the substrate, and three main processes are used [20]. Each of these methods is discussed in the following section.

2.1.1 Industrial production methods

The silver catalyst process serves as the basis for the first two methods, each representing different variations of this fundamental approach [20]. The first, known as the BASF process, allows the almost complete conversion of methanol. The second enables partial conversion, integrating a distillation process with the subsequent recycling of methanol. In both approaches, methanol undergoes partial oxidation and dehydrogenation. In particular, reactions R1, R2, and R3 occur in the presence of the silver catalyst, as described in [18, 21].

$$CH_3OH \rightleftharpoons CH_2O + H_2,\ \Delta H_R^0 = +84\,\frac{kJ}{mol} \qquad \text{R1}$$

$$H_2 + \frac{1}{2}O_2 \rightarrow H_2O,\ \Delta H_R^0 = -243\,\frac{kJ}{mol} \qquad \text{R2}$$

$$CH_3OH + \frac{1}{2}O_2 \rightarrow CH_2O + H_2O,\ \Delta H_R^0 = -159\,\frac{kJ}{mol} \qquad \text{R3}$$

The detailed reaction mechanism for the reaction of methanol to formaldehyde, using a silver catalyst, is not yet fully understood. Recent investigations have provided a deeper understanding of the underlying mechanism, highlighting how different atomic oxygen species affect the route and selectivity of the reaction [18, 22].

Figure 3 shows a schematic diagram of the BASF process [21]. A mixture of methanol and water, together with air, is first fed into an evaporator. A gaseous mixture of air, methanol and water subsequently passes through a reactor containing a thin bed of silver catalyst crystals. The ensuing reaction takes place at temperatures between 600–720 °C under atmospheric pressure. The reaction products are then immediately cooled to 150 °C. In the final step, this gas is passed through an absorption column where formaldehyde is absorbed in water. The resulting product exits the column as an aqueous formaldehyde solution of approximately 50% by weight.

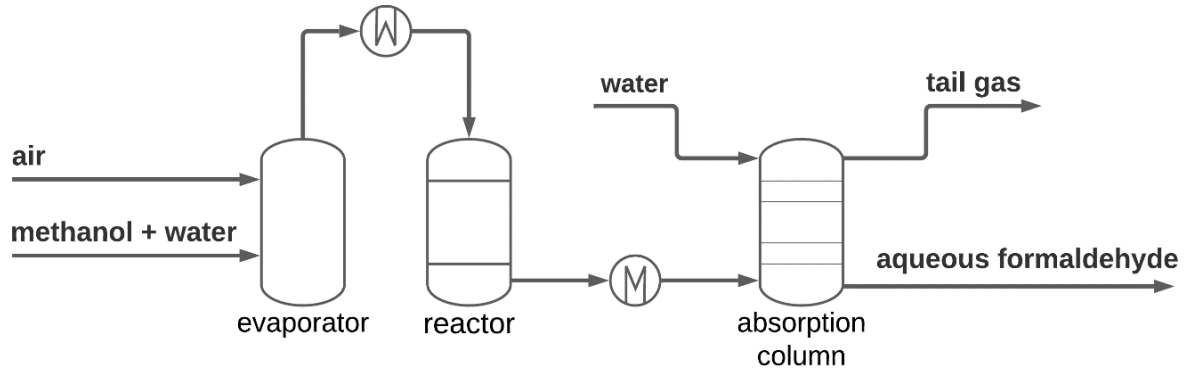

Figure 3. Silver catalyst process at the BASF: scheme prepared by [23][1], adapted from [21]

Figure 4 illustrates a simplified model of the incomplete conversion process. In this method, methanol and air are introduced into an evaporator, and the gas is then mixed with steam. Once heated, this gas mixture flows through a reactor containing a catalyst bed where the reaction takes place at temperatures between 590 and 650 °C [18]. After the reaction, the products are rapidly cooled. Next, the gas enters an absorption column where the formaldehyde and methanol are stripped with water. The mixture of formaldehyde, methanol and water is then fed to a distillation column where the methanol is collected and recycled. An aqueous solution of formaldehyde goes through an anion exchange unit to minimize the concentration of formic acid present in the solution.

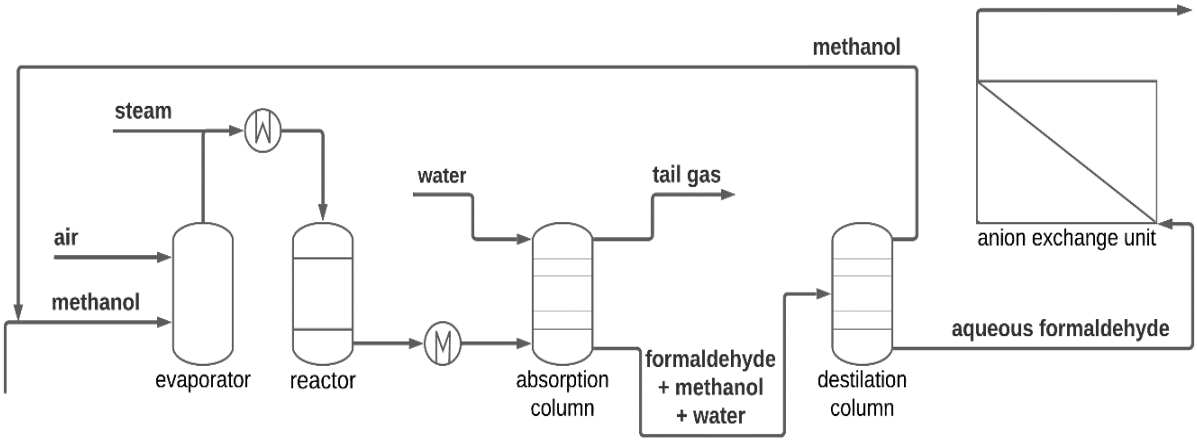

Figure 4. Silver catalyst process with incomplete conversion; scheme prepared by [23][1], adapted from [22, 24]

[1] Bachelor thesis of D. Mertens supervised at ITES in the framework of this study

Next, the Formox process operates at ambient pressure and at temperatures of between 250 and 400 °C, using excess air and achieving methanol (MeOH) conversions exceeding 99%. In addition, the process yields ranged between 88% and 92% formaldehyde [25]. A simplified process route is shown in Figure 5. Methanol and air are first fed into an evaporator. The gas mixture then passes through the reactor, which is filled with the catalyst, and before entering an absorption column, the gases are cooled. The solution then passes through an anion-exchange unit, where the formic acid concentration decreases, before leaving the process [18]

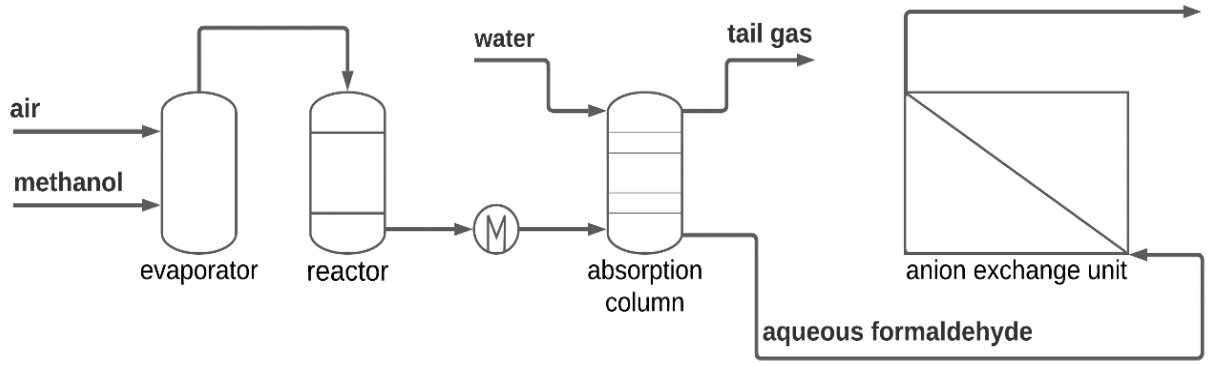

Figure 5. Formox process; scheme prepared by [23][1], adapted from [18, 24]

In the Formox process, methanol undergoes oxidation in the presence of a metal oxide catalyst (R4, R5 and R6) [18]. Oxides of iron, molybdenum and vanadium are typically employed in the process. The catalyst changes its state between oxidized (K_{ox}) and reduced (K_{red}).

$$CH_3OH + K_{ox} \rightarrow CH_2O + H_2O + K_{red} \quad \text{R4}$$

$$K_{red} + \frac{1}{2}O_2 \rightarrow K_{ox},\ \Delta H_R^0 = -159\,\frac{kJ}{mol} \quad \text{R5}$$

$$CH_2O + \frac{1}{2}O_2 \rightleftharpoons CO + H_2O,\ \Delta H_R^0 = -215\,\frac{kJ}{mol} \quad \text{R6}$$

The catalyst used in the Formox process primarily consists of $Fe_2(MoO_4)_3$, supplemented with MoO_3 to obtain an atomic Mo/Fe ratio between 1.5 and 3 [26]. During the oxidation of CH_3OH over the MoO_3-$Fe_2(MoO_4)_3$ catalyst, surface oxygen is consumed. Subsequently, the vacancies created are filled by oxygen anions from O_2 in the feed stream, which is known as the Mars–van Krevelen mechanism [27]. However, Mo-containing catalysts face a significant challenge. Over time, they deactivate due to the formation of volatile Mo species as a reaction takes place between MoO_3 and CH_3OH. This problem is particularly noticeable at higher

temperatures and increased CH_3OH concentrations, limiting the catalyst lifespan to approximately six to eight months [25].

In summary, conventional formaldehyde production methods are increasingly seen as unsustainable due to their high energy requirements. In addition, the generation of secondary pollutants complicates waste management and reduces overall process performance. With the growing demand for sustainability in chemical industry, more efficient and eco-friendly methods of formaldehyde production have been sought [19, 26, 28].

2.1.2 Direct dehydrogenation of methanol to formaldehyde

The reaction of the direct dehydrogenation of methanol (R7), is considered to be a promising alternative to the production routes listed in Section 2.1.1 [10]. However, there are still some obstacles to overcome. This reaction is endothermic and therefore requires a supply of heat. Furthermore, this process is reversible, and equilibrium only favors formaldehyde formation at temperatures above 470 °C. For higher conversions, temperatures must exceed 580 °C. In addition to R7, several other reactions may occur, resulting in by-products such as CO, CH_4, H_2O and others [29]. The most important side reaction is the decomposition of formaldehyde to carbon monoxide and hydrogen since formaldehyde is thermodynamically unstable (R8) [18].

$$CH_3OH \rightleftharpoons CH_2O + H_2,\ \Delta H_R(900K) = +92\,\frac{kJ}{mol} \qquad \text{R7}$$

$$CH_2O \rightarrow CO + H_2,\ \Delta H_R(900K) = +13\,\frac{kJ}{mol} \qquad \text{R8}$$

Furthermore, other decomposition reactions are possible, as described in [30]:

$$2CH_2O \rightarrow HCOOH + H_2 + C,\ \Delta H_R(900K) = -137\,\frac{kJ}{mol} \qquad \text{R9}$$

$$2CH_2O \rightarrow CH_3OH + CO,\ \Delta H_R(900K) = -79\,\frac{kJ}{mol} \qquad \text{R10}$$

$$CH_2O \rightarrow H_2O + C,\ \Delta H_R(900K) = -122\,\frac{kJ}{mol} \qquad \text{R11}$$

$$2CH_2O \rightarrow CH_4 + CO_2,\ \Delta H_R(900K) = -234\,\frac{kJ}{mol} \qquad \text{R12}$$

$$2CH_2O \rightarrow C + CO_2 + 2H_2,\ \Delta H_R(900K) = -146\,\frac{kJ}{mol} \qquad \text{R13}$$

During the process of dehydrogenation, the following reactions may also occur [30]:

$$2CH_3OH \rightarrow CH_2O + H_2O + CH_4,\ \Delta H_R(900K) = -28\,\frac{kJ}{mol}$$ R14

$$CH_3OH \rightarrow C + H_2O + H_2,\ \Delta H_R(900K) = -31\,\frac{kJ}{mol}$$ R15

$$2CH_3OH \rightarrow CH_3OCH_3 + H_2O,\ \Delta H_R(900K) = -19\,\frac{kJ}{mol}$$ R16

$$2CH_3OH \rightarrow HCOOCH_3 + 2H_2,\ \Delta H_R(900K) = +70\,\frac{kJ}{mol}$$ R17

$$CH_3OH \rightarrow CO + H_2,\ \Delta H_R(900K) = +105\,\frac{kJ}{mol}$$ R18

A thermodynamic analysis of the uncatalyzed dehydrogenation of methanol was carried out in Aspen Plus® 14. The main aim of this study was to find differences between the thermodynamic predictions and actual experimental observations with many possible reactions involved (R7-R18). Using Aspen Plus simulation with a Gibbs reactor, a multi-component system of methanol, formaldehyde, carbon monoxide, carbon dioxide, carbon, methane and hydrogen was studied. In this analysis, the system was supplied with a steady stream of 10 kmol h^{-1} of methanol. The resulting molar flows of each component are shown in Figure 6. It was found that between 200 °C and 1200 °C, almost all of the methanol input decomposed. Notably, only traces of formaldehyde were observed at approximately 525 °C. At lower temperatures, production is characterized mainly by methane, water and carbon dioxide. However, as the temperature increases, there is a marked shift towards the formation of hydrogen and carbon monoxide.

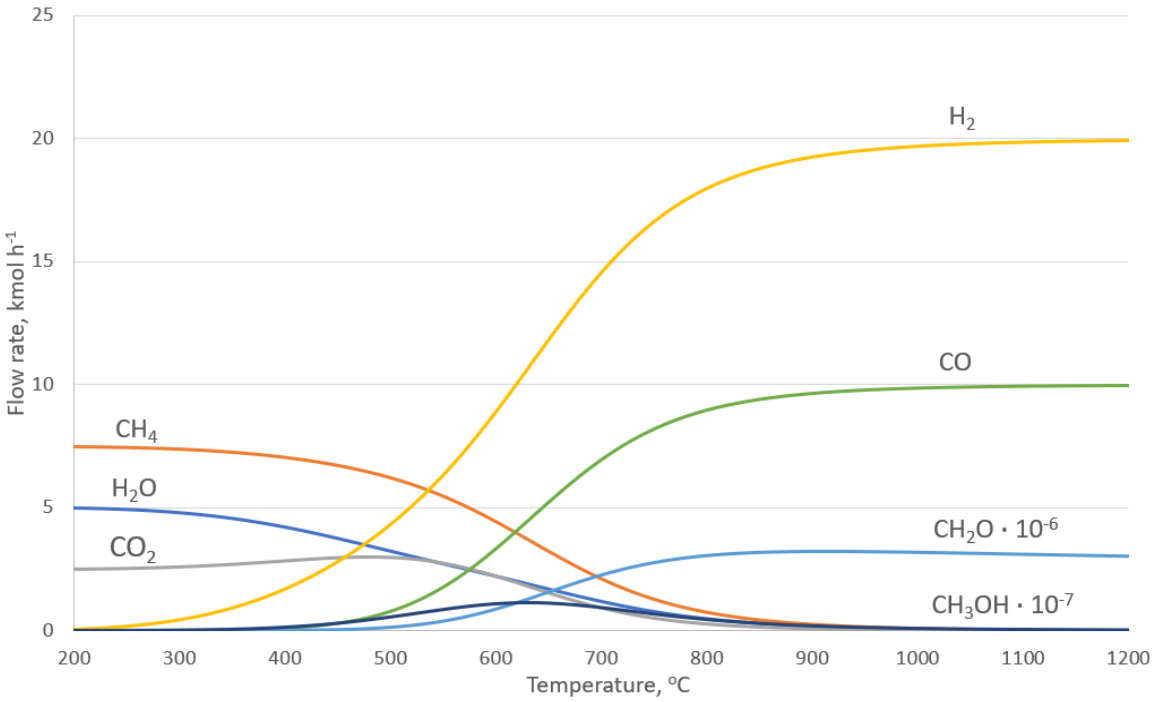

Figure 6. Thermodynamic evaluation of the uncatalyzed dehydrogenation of methanol

The thermodynamic model suggests that the decomposition of methanol should lead mainly to carbon monoxide and hydrogen, with only small amounts of formaldehyde. However, actual experimental observations contrast with these predictions [29, 31]. Under practical conditions, the dominant products of methanol decomposition are methanol (unreacted), formaldehyde, carbon monoxide and hydrogen, with only negligible amounts of methane and carbon dioxide. This difference indicates that, in practice, some reactions are dominated more by kinetics than by thermodynamics. As a result, while certain products may be thermodynamically favored, kinetic rates may hinder their formation and support the synthesis of formaldehyde instead. Overall, the direct dehydrogenation of methanol to formaldehyde requires specific process conditions. These include high temperatures above 580 °C, short residence time (preferably below 1 s), rapid cooling and a catalyst that is highly selective towards formaldehyde [29]. Additionally, a high rate of methanol conversion is desired because any reactant remaining in the product is difficult to separate.

In literature, numerous studies have explored various process concepts and catalysts for the dehydrogenation of methanol to water free formaldehyde [9, 10, 14, 17, 25, 29, 32–34]. Research into catalysts for methanol dehydrogenation dates back to the 1960s and focused on the study of various elements and their compounds. Compounds containing elements such as silver, copper, zinc, indium, lithium and sodium proved to

be particularly active [10]. Initial studies focused on silver and silver-copper catalyst combinations [21, 33]. However, these reactions require the presence of oxygen to achieve significant conversions. Without oxygen, the dehydrogenation process proceeds at a slow pace [34, 35]. Various attempts to improve the reaction, including the addition of oxidic substances such as silicon, or copper, had no effect [36]. Similarly, the introduction of elements such as selenium, tellurium or sulfur did not lead to significant improvements due to their volatility [10]. It was found that oxidic catalysts were rapidly reduced by methanol, whereas metallic catalysts required high temperatures to achieve significant methanol conversion. Although zinc, in both its metallic and oxidic forms showed some promise, its activity was short-lived, especially in its molten or alloyed state [37]. Zinc oxide demonstrated slightly greater catalytic performance than its metallic form [36, 38]. However, its effectiveness was limited due to its reduction by methanol. Other transition metals were also evaluated, but none led to results that could be considered suitable for industrial applications [10]. In addition, sodium-containing compounds such as Na_2CO_3, $NaMoO_3$ and $NaAlO_2$ were also identified as potential catalysts for the reaction of methanol dehydrogenation to formaldehyde. The main active component in these substances appears to be elemental sodium. Notable contributions in this area have been made by Sauer and Emig [9, 31, 39], Ruf [13, 29, 40], Zaza, Su, Maurer, Meyer and Renken [11, 14, 15, 17, 30, 36].

Sauer [31] investigated two reactor configurations: a catalyst-coated tube wall reactor (TWR) and a traditional fixed bed reactor. The catalysts used were aluminates of the alkali metals, sodium and lithium ($LiAlO_2 \cdot NaAlO_2$). In the fixed bed reactor, the catalyst bed was supported by a grid inside an alumina ceramic reactor tube. Regarding the TWR, the inner surface was coated with the catalyst over a length of 50 to 200 mm. The experimental results showed comparable conversion (~97%) and selectivity (~68%) for both reactor types. Observations indicated that an increased feed concentration decreased the conversion, but higher temperatures increased the conversion, while the selectivity remained relatively constant.

Ruf [40] conducted experiments in a tube reactor with an inner diameter of 8 mm and a reaction zone length of 450 mm. In his experimental approach, elemental sodium was used as the catalyst. The crucible was heated in a ceramic tray placed near the reactor inlet. A stream of nitrogen was used to carry the vaporized sodium.

Simultaneously, methanol was introduced via a separate nitrogen stream. These two streams were then mixed directly at the reactor inlet. The velocity of the stream had a direct effect on the reaction dynamics. As the velocity increased, the space-time duration of the reaction shortened. Notably, both velocities exhibited a laminar flow profile. In addition, by adjusting the temperature of the ceramic tray, the amount of sodium that vaporized and subsequently fed to the reaction was varied. This adjustment resulted in a corresponding increase or decrease in both methanol conversion and formaldehyde selectivity. When the reactor temperature was further increased, a maximum formaldehyde yield of approximately 83% was achieved.

As a further step, a new technique was developed to ensure a constant supply of sodium and prevent its passivation [13]. This method involved melting sodium in a heated tank. Nitrogen was fed into this tank via two different tubes. One long tube extended directly into the molten sodium, while a shorter tube introduced nitrogen above the liquid sodium, creating an inert environment. The vaporized sodium was then carried into the reactor, driven by the stream of nitrogen. Upon entry into the reactor, this sodium-nitrogen stream merged with another stream containing methanol. The amount of sodium supplied was adjusted by changing the temperature of the tank. The velocity and space-time within the reactor were controlled by the methanol-nitrogen stream. By varying both the tank and reactor temperatures, the peak of the formaldehyde yield was 72%. It was also observed that an increased fluid velocity combined with a higher methanol concentration at the inlet resulted in a reduction in methanol conversion.

For the direct dehydrogenation of methanol, Renken and Meyer [14] studied various catalysts, mainly alkali carbonates. Among them, sodium carbonate showed the highest selectivity, ranging between 55 and 65% for conversions less than 60%. The catalyst showed signs of deactivation in the first six hours due to coke accumulation, but it was possible to regenerate it. To further improve the selectivity, indium was doped into sodium carbonate, increasing the selectivity to 75%. Sodium carbonate was compared with other alkali salts and transition metal catalysts such as zinc, selenium, tellurium and silver. Although these other catalysts can be active, they face issues such as volatility and limited operational lifespans due to the evaporation of active compounds at high temperatures. Sodium carbonate, on the other hand, remains

stable and offers consistent performance, making it a more reliable choice for continuous processes.

Zaza, de la Torre and Renken [11] presented a fluidized bed reactor for methanol dehydrogenation using a sodium carbonate catalyst with particle sizes between 50 and 80 μm. The reaction temperature was adjusted from 600 to 800 °C, and the porosity was varied. The results showed that the conversion improved with increasing temperature but was not affected by the variation in porosity. Conversely, the selectivity decreased at higher temperatures due to formaldehyde decomposition. However, using a higher porosity, i.e., reduced catalyst presence, resulted in increased selectivity. Specifically, a porosity of 97% achieved a conversion and selectivity similar to those of a fixed bed reactor of 70% and 55% respectively, while for the porosity of 0.995 the selectivity increased to 80%. Zaza et al. found that sodium carbonate supported on activated carbon is an effective catalyst for the dehydrogenation of methanol to formaldehyde, achieving high activity and selectivity at elevated temperatures [41]. However, the process is hindered by significant gas phase reactions which reduce formaldehyde selectivity in a continuous fixed bed reactor with external recycling. Research showed that hydrogen, methoxy and hydroxymethyl intermediates are strongly adsorbed on the catalyst surface and play a critical role in the reaction mechanism. In addition, the presence of activated carbon enhances the activity of the catalyst through a hydrogen spillover effect, facilitating hydrogen desorption and improving overall efficiency. These findings contribute to a better understanding of the reaction kinetics.

Maurer and Renken developed a microstructure reactor system with channels less than 1 mm in diameter [17]. This approach aimed to achieve fast mixing, efficient heating and cooling, short space-time and precise temperature control, all of which can promote high formaldehyde yields. Given the small size of the reactor, the high surface area-to-volume ratio allowed a robust heat transfer coefficient of approximately 10 kW m^{-2} K^{-1}. A unique heater was designed for the junction between the reactor and the cooling micro heat exchanger, which improved the temperature distribution throughout the reactor. After careful optimization of the system, a peak formaldehyde yield of 80% was achieved at a temperature of 825 °C and a space-time of 0.205 seconds by using sodium as the catalyst.

2.2 Sodium

Sodium is the most commonly known and widely produced alkali metal, belonging to group 1 of the periodic table and is characterized by an atomic number of 11 and an atomic mass of 22.9898 u. Sodium metal is distinguished by its extensive range of applications [42]. Elemental sodium plays a crucial role in various industrial processes, from pharmaceutical preparations to the manufacture of inorganic chemicals. Its properties allow easy liquefaction, extending its utility in metallurgical processes and other physical applications. The properties of sodium derive directly from its atomic structure [43]. Its electronic configuration is described as $1s^2$ $2s^2$ $2p^6$ $3s^1$. Consequently, sodium has a large atomic volume, and the cohesive forces in its lattice are comparatively weak. The enhanced reactivity of sodium is also due to its electronic structure, as sodium has a single electron ($3s^1$) in its outer shell, which is weakly bound to the nucleus. Sodium, together with other alkali metals, exhibits properties such as lower density, decreased hardness and lower melting and boiling points compared to alkaline earth metals. It also has lower sublimation, evaporation and dissociation energies [44]. Sodium solidifies in a body-centered cubic crystal structure. It exhibits typical metallic properties such as high thermal and electrical conductivity. In fact, the electrical conductivity of sodium at 20 °C is approximately one-third that of copper. Sodium remains liquid over a wide temperature range, from 97.8 °C to 881.4 °C at atmospheric pressure [43]. In its gaseous form, sodium predominantly exists as single atoms (monatomic). However, clusters of two (dimers) and four (tetramers) sodium atoms are also observed.

Sodium reacts with hydrogen at approximately 200–300 °C to form sodium hydride. In NaH, hydrogen is present as a hydride ion [43]. In the realm of organic synthesis, sodium hydride primarily exhibits minimal reducing abilities, the most defining characteristic of which is its high basicity. In particular, sodium hydride serves as a strong base, reacting with all acids and with both organic and inorganic compounds containing an active hydrogen atom. Its basicity exceeds that of sodium amide. Under certain conditions, such as in molten NaOH or eutectic salt mixtures, NaH acts as a powerful reducing agent, especially against metal salts and oxides.

When sodium interacts with oxygen, it can form several different oxides: sodium monoxide (Na_2O), peroxide (Na_2O_2) and superoxide (NaO_2). In addition, under certain

conditions, the formation of the ozonide compound NaO_3 is observed. As sodium reacts with oxygen to form monoxide and peroxide, energy is released. Comprehensive studies were carried out to understand the structure and chemical properties of oxygen compounds formed with alkali metals [42]. When exposed to typical atmospheric air, molten sodium has the potential to ignite at temperatures above 115 °C. However, a higher ignition temperature is required in dry air. The combustion process is energetic and produces significant amounts of smoke. As the reaction progresses, an intense white-yellow light is emitted, and the formation of both Na_2O and Na_2O_2 is observed.

When sodium comes into contact with water, it reacts to form sodium hydroxide and hydrogen gas. If the released hydrogen combines with air, the resulting gas mixture can become explosive and potentially detonate with great force. In addition, when an excess of sodium interacts with high-pressure steam in the absence of air, sodium hydroxide and sodium hydride are formed [43].

The chemical industry relies heavily on many products that originate from sodium metal [36, 37, 38, 39]. Sodium, especially in its liquid form, has gained significant importance in the nuclear energy sector as a heat transfer medium. It is used throughout the world as a coolant in fast breeder reactors [42, 43]. Some power plants contain several thousand tons of sodium. The choice of sodium for fast breeder core cooling is due to its excellent thermal and neutronic properties, especially where there is a high heat flux. Moreover, sodium is used extensively in various industries [46]. It serves as a critical component in the production of sodium hydroxide through the electrolysis of molten sodium chloride, which is essential in the manufacture of a wide range of products from gasoline additives to synthetic rubber and polymers such as nylon. Sodium is also used in metal refining processes where it acts as a reducing agent to produce metals such as titanium and zirconium from their respective chlorides. In the field of lighting, sodium vapor lamps use the distinctive yellow emission of sodium for street lighting due to its energy efficiency and intensity. Sodium also plays an important role in organic chemistry, particularly in Birch reduction, a process used to create complex organic compounds. There are many other ways in which sodium can be applied, one of which is the use of sodium as a catalyst, which is described in the following section.

2.2.1 Sodium vapor

The studies mentioned in section 2.1.2 identified sodium-based catalysts as the most potent for methanol dehydrogenation, as detailed in [10, 13 ,14, 31]. In alignment with these findings, Sauer and Emig [9] showed that when reducing gases such as hydrogen and methanol are passed through an alkali aluminate layer, catalytically active species are released. They hypothesized that the volatilized sodium would play a crucial role in the radical reaction of methanol, leading to an increased rate of methanol conversion, as described in R19. In addition, they proposed that the sodium atoms may also have trapped hydrogen radicals (R20 and R21), which helped to prevent the decomposition of the formaldehyde produced during the process. Their results suggest that the solid sodium compounds in the reactor act as a primary catalyst and that the actual catalyst is produced by evaporation. This mechanism facilitates the generation of an active gaseous catalyst from a solid catalyst, contributing to the efficiency and selectivity of the chemical reaction.

$$Na^{\cdot} + CH_3OH \rightarrow C^{\cdot}H_2OH + NaH \qquad \text{R19}$$

$$Na^{\cdot} + H^{\cdot} \rightarrow NaH \qquad \text{R20}$$

$$2NaH \rightarrow 2Na^{\cdot} + H_2 \qquad \text{R21}$$

Ruf et al. [13] revised their earlier experiments involving the evaporation of sodium from a crucible bypassed by a methanol stream. The authors convincingly argued that the reaction is catalyzed by sodium vapor. This was further substantiated by the introduction of sodium methoxide as a catalyst instead of sodium vapor, which gave similar results to previous experiments. Ruf's research [13] shed new light to the possible chemical pathways for the direct dehydrogenation of methanol to formaldehyde catalyzed by sodium compounds. He proposed that sodium methoxide serves as the key intermediate in the sodium-catalyzed reaction and decomposes into methoxy radicals. This proposal marked a significant shift from the previously held belief that hydroxymethyl radicals were the intermediates in this reaction. His proposal regarding the role of sodium methoxide was encouraged by the experiment with methane instead of methanol. This setup showed no activity even at high temperatures up to 950 °C. Therefore, it was concluded that methoxy species are present. In addition to these experiments – both with sodium methoxide and methane – the heat of formation and the bond strengths of the radicals involved needed to be analyzed to

prove the reaction (Table 1). It can be concluded that methane does not react in the presence of sodium, even at high temperatures such as 950 °C, because the strength of the carbon-hydrogen bond is greater, and the heat of formation for methyl radicals is significantly greater than that for hydroxymethyl radicals. This difference in bond strength and heat of formation suggests that the reaction behaviors of methane and methanol in the presence of sodium are not directly comparable [47].

Table 1. Bond strength and heat of radical formation [48]

Bond	Bond strength, kJ mol^{-1}	Radical formation heat, kJ mol^{-1}
$H\text{-}CH_2OH$	402	-17 ($C^{\cdot}H_2OH$)
$CH_3O\text{-}H$	440	21 ($CH_3O^{\cdot}$)
$CH_3\text{-}OH$	385	37.5 ($^{\cdot}OH$)
$H\text{-}CH_3$	439	147 ($^{\cdot}CH_3$)
H-CHO	368	43 ($^{\cdot}CHO$)

Additionally, sodium plays a dual role in this chemical reaction. Firstly, it serves as a promoter for the reaction that leads to the formation of formaldehyde. Secondly, sodium acts as an inhibitor by trapping hydrogen radicals. By doing so, sodium effectively reduces the rate of formaldehyde decomposition, thereby stabilizing it. This dual functionality of sodium highlights its importance in both enhancing the production of a desired chemical (in this case, formaldehyde) and maintaining the integrity of that product by inhibiting its degradation. In order to determine the exact underlying mechanism of the methanol dehydrogenation reaction, detailed in-situ experiments need to be carried out.

In light of the findings presented in the current state of the art, and with the aim of further advancing this knowledge base, this thesis looks into the direct evaporation of sodium as a preferred method of the catalyst dosing for the direct methanol dehydrogenation to formaldehyde reaction. The primary objective was to develop a stable catalyst dosage system (Section 3.1) and to determine the optimal material selection which can mitigate the corrosive nature of sodium (discussed in the subsequent sections 2.2.2 and 4.2). In addition, sodium catalytic performance under a variety of reaction conditions is described in Section 5.3.

2.2.2 Corrosion behavior of sodium

Sodium, which is widely used in fast breeder reactors, has been the subject of extensive research [49–54], particularly due to its corrosion-inducing properties. Corrosion caused by liquid sodium is a major challenge in the design and maintenance of steel alloys used in harsh environments, such as nuclear reactors and heat exchangers. When exposed to sodium, steel undergoes both uniform dissolution, which erodes the surface uniformly, and selective leaching, which preferentially dissolves certain alloying elements [53]. The integrity of the steel is further compromised by sodium penetrating through microscopic flaws or grain boundaries, potentially causing internal damage and contributing to liquid metal embrittlement. In addition, impurities such as oxygen and carbon can initiate additional corrosive processes, including oxidation and changes in carbon content through carburization or decarburization. These processes not only result in material loss but also lead to a restructuring of the alloy microstructure and changes at the surface level, affecting the mechanical properties of the material. The effects of these corrosion mechanisms are particularly critical in thin-walled components or heat exchanger tubes that must withstand high temperatures and demanding hydrodynamic conditions [55].

Understanding the process of corrosion and the extent of damage is essential to determine the appropriate materials to be used and their expected service life, ensuring that the components can function reliably within the specified operating limits [52, 53]. It is known that oxygen concentrations must be very low (< 3 wppm) for stainless steel 316 to be unaffected by corrosion caused by sodium. Cold traps are commonly used in sodium coolant systems to maintain low oxygen levels by crystallizing sodium oxide from the liquid sodium [56]. The corrosion rate can be influenced by the presence of dissolved oxygen, as sodium can react with elements such as chromium and iron to form compounds such as sodium chromite ($NaCrO_2$) or Na-Fe-O compounds e.g., Na_3FeO_4 (consisting of $2Na_2O$ and FeO). While the formation of sodium chromite and its thermodynamic properties were observed and characterized in studies, the existence and specific nature of the Na-Fe-O compound have not yet been conclusively established [53].

Section 4.2, provides a comprehensive selection of methods and techniques to mitigate sodium induced corrosion. This section not only identifies the methods

selected for the MEDENA mini-plant, but also outlines the lessons learned from their implementation and emphasizes the importance of maintaining system purity to ensure long-term effectiveness.

2.3 Sodium methoxide

Sodium methoxide (CH_3ONa) is a versatile white solid compound extensively utilized in both industrial and laboratory applications [57]. It is a strong base used as a catalyst in organic synthesis, particularly in the transesterification of vegetable oils for biodiesel production [58]. Sodium methoxide is also present in the synthesis of pharmaceuticals, agrochemicals and as an intermediate in the production of flavors and fragrances. Sodium methoxide is highly corrosive and reacts strongly with water to form methanol and sodium hydroxide. It is sensitive to air and moisture, absorbing carbon dioxide to form sodium carbonate [59]. There are 4 main methods for producing sodium methoxide, each with distinct advantages and challenges [60]:

1. Sodium amalgam: This traditional method involves using a sodium amalgam, which is an alloy of mercury and sodium. It is a by-product of the caustic-chlorine process. Methanol vapor strips sodium from the amalgam in a packed column. While cost-efficient, this process tends to be phased out due to environmental concerns related to mercury use.
2. Sodium metal: Sodium methoxide is produced by reacting of molten sodium with methanol in a highly exothermic reaction. This method yields high-purity sodium methoxide but requires careful control due to the reactivity of sodium and the risk of explosion from hydrogen gas production.
3. Sodium hydroxide: This safer method uses caustic soda and methanol in a reactive stripping column, with methanol vapor driving the methoxylation reaction. Although it requires more energy for methanol-water separation, it uses cheaper raw materials.
4. Sodium acetate: Involves electrodialysis to produce sodium methoxide and acetic acid from sodium acetate and methanol. This method offers high purity but is energy-intensive and not yet commercially viable.

As mentioned in Section 2.2.1, sodium methoxide was also evaluated as a potential catalyst for the direct dehydrogenation of methanol to formaldehyde. The assessment and analysis of this approach are comprehensively discussed in Section 4.3.

2.4 Sodium carbonate

Sodium carbonate (Na_2CO_3), also known as soda ash, is a neutral sodium salt derived from carbonic acid and is a key raw material in the chemical industry [61]. In addition to the anhydrous form of Na_2CO_3, there are several hydrated forms. These include sodium carbonate monohydrate ($Na_2CO_3 \cdot H_2O$), sodium carbonate heptahydrate ($Na_2CO_3 \cdot 7H_2O$) and sodium carbonate decahydrate ($Na_2CO_3 \cdot 10H_2O$) [61]. Sodium carbonate undergoes thermal decomposition into sodium oxide and carbon dioxide when exposed to a vacuum without chemical activating agents, such as water vapor. This decomposition starts at approximately 1000 °C. Sodium carbonate also has hygroscopic properties [62]. When exposed to air with a relative humidity of 96%, it can increase its weight by approximately 1.5% in just 30 minutes. When stored in a humid environment, the alkalinity of sodium carbonate decreases due to the absorption of moisture and carbon dioxide from the surrounding air. This absorption results in a chemical reaction (R22), as described in [61]:

$$Na_2CO_3 + H_2O + CO_2 \rightarrow 2NaHCO_3 \qquad \text{R22}$$

This equation shows how sodium carbonate reacts with water and carbon dioxide to form sodium bicarbonate. Above approximately 400 °C, water vapor reacts with sodium carbonate, leading to the formation of sodium hydroxide and carbon dioxide. The chemical reaction can be represented as (R23) [61]:

$$Na_2CO_3 + H_2O \rightarrow 2NaOH + CO_2 \qquad \text{R23}$$

Furthermore, sodium carbonate has superior catalytic activity in the direct dehydrogenation of methanol to anhydrous formaldehyde compared to K_2CO_3 and Cs_2CO_3, as demonstrated in previous research [10]. Some alkali catalysts are listed in Table 2. It is important to note that the comparison of the results of these experiments should be performed carefully, as numerous other factors, which are not listed, can significantly influence the conversion and selectivity. Variables such as the time on the stream, the concentration of methanol and the amount of catalyst used are just a few examples. Each of these factors can have a different effect on the process and its efficiency, so it is necessary to consider them individually when analyzing the data and drawing conclusions. Nevertheless, it is evident that sodium carbonate is one of the most promising catalysts among those listed.

Table 2. Results of selected previous research on alkali catalysts [10]

Catalyst	Reaction conditions	Conversion of MeOH, %	Selectivity of CH_2O, %	Reference
Na_2CO_3	650 °C ~ 0.1 mol CH_3OH in N_2	60	57	[14]
K_2CO_3		55	30	
Cs_2CO_3		45	10	
NaY	500 °C ~ 0.14 mol CH_3OH in He	8	15	[59]
Na_2CO_3/NaY		31	9	
Na_2CO_3 + C (75 wt%)	700 °C ~ 0.1 mol CH_3OH in Ar	50	90	[15]
Na_2CO_3 + Fe (3.5 wt%)		35	93	
Na_2CO_3 + Ni (3.5 wt%)		61	81	

As discussed and outlined above, as well as in Section 2.1.2, sodium carbonate is identified as one of the most potent catalysts for the nonoxidative dehydrogenation of methanol, with the aim of producing water-free formaldehyde and hydrogen. The effectiveness of sodium carbonate in this role can be attributed to a number of factors, including its ability to selectively promote the formation of formaldehyde while minimizing side reactions and the co-production of hydrogen, which is valuable as a clean energy carrier. Furthermore, the stability and non-toxicity of sodium carbonate make it an attractive catalyst due to its potential ease of handling in industrial applications. Consequently, sodium carbonate was selected for testing in the DRH reactor, as detailed in Sections 3.3. Its performance under various reaction conditions was examined comprehensively in Section 6.

Reaction mechanism

The comprehensive reaction mechanism was previously elucidated by Su [16]. The experimental results indicate that during the catalytic dehydrogenation of methanol, atomic hydrogen has a strong affinity for adsorption on the surface [16]. Once adsorbed, it tends to recombine and slowly desorb in the form of hydrogen gas.

Conversely, the associated species, $\cdot OCH_3$ or $\cdot CH_2OH$, when adsorbed, are observed to desorb more rapidly. In addition, it is suggested that free radicals, generated from surface reactions, could initiate gas-phase chain reactions, leading to the production of formaldehyde and other compounds. Based on these observations, it was hypothesized that the initial step in the dehydrogenation of methanol on sodium carbonate involves the dissociation of the $H - CH_2OH$ bond. This dissociation leads to the formation of surface hydrogen and a gas-phase $\cdot CH_2OH$ radical, which then participates in a series of chain reactions. This mechanism is shown by a series of equations proposed by Su et al. [16]. On the surface, the reactions involve various transformations of methanol, including its conversion to different intermediates and radicals (R24–R30) [16]. These include the formation of $\cdot CH_2OH$ and $\cdot OCH_3$ species as well as hydrogen radicals, among others.

$CH_3OH_g = CH_3OH_s$ R24

$CH_3OH_s = \cdot CH_2OH_g + \cdot H_s$ R25

$CH_3OH_s = \cdot OCH_{3s} + \cdot H_s$ R26

$\cdot OCH_{3s} \rightarrow CO_g + H_{2g} + \cdot H_s$ R27

$\cdot OCH_{3s} \rightarrow CH_2O_g + \cdot H_s$ R28

$CH_3OH_s + \cdot H_s \rightarrow H_{2g} + \cdot CH_2OH_g$ R29

$\cdot H_s + \cdot H_s \rightarrow H_{2g}$ R30

In the gas phase, the suggested reactions (R31–R45) are as follows [16]:

$CH_2O_g + CH_2O_g = \cdot CHO_g + \cdot CH_2O_g$ R31

$CH_3OH_g + M^* \rightarrow \cdot CH_{3g} + \cdot OH_g + M$ R32

$\cdot CH_2OH_g + M \rightarrow \cdot H_g + CH_2O_g + M^*$ R33

$\cdot CH_2OH_g + CH_2O_g \rightarrow \cdot CHO_g + CH_3OH_g$ R34

$\cdot CHO_g + M \rightarrow \cdot H_g + CO_g + M^*$ R35

$\cdot CHO_g + CH_3OH_g \rightarrow C\,H_2O_g + \cdot CH_2OH_g$ R36

$\cdot CHO_g + CH_2O_g \rightarrow CO_g + \cdot CH_2OH_g$ R37

$\cdot H_g + CH_3OH_g \rightarrow \cdot CH_2OH_g + H_{2g}$ R38

$\cdot H_g + CH_3OH_g \rightarrow H_2O + \cdot CH_{3g}$ R39

$\cdot H_g + CH_2O_g \rightarrow \cdot CHO_g + H_{2g}$ R40

$\cdot H_g + CH_2O_g \rightarrow \cdot CH_2OH_g$ R41

$\cdot CH_{3g} + CH_3OH_g \rightarrow CH_{4g} + \cdot CH_2OH_g$ R42

$\cdot CH_{3g} + CH_2O_g \rightarrow CH_{4g} \cdot CHO_g$ R43

$\cdot OH_g + CH_2O_g \rightarrow H_2O + \cdot CHO_g$ R44

$\cdot OH_g + CH_3OH_g \rightarrow H_2O + \cdot CH_2OH_g$ R45

Su et al. [16] suggested that the gas phase $\cdot CH_2OH_g$ is formed by the $H - CH_2OH$ bond breaking on the surface of the catalyst (as shown in R25). Reactions 26–28 are proposed for the direct formation of carbon monoxide and formaldehyde, which is particularly important for fresh catalysts [63]. However, these reactions are minor when compared to gas-phase chain reactions. Hydrogen recombination and desorption from the surface (R30) is assumed to be the rate-determining step. This is based on the observation that purging the catalyst with methanol significantly increased the conversion but did not change the formaldehyde selectivity. This implies that highly adsorbed hydrogen accumulates on the catalyst and inhibits $H - CH_2OH$ bond cleavage by blocking active sites. Enhanced desorption of hydrogen during purging frees these sites, allowing faster bond cleavage until hydrogen saturation prevails. Catalytic activity can be improved by accelerating hydrogen desorption, which is observed when carbonate is mixed with active carbons or transition metals, such as iron, increasing activity without affecting selectivity [63]. Formaldehyde decomposes considerably without a catalyst, while the thermal decomposition of methanol is minor. Therefore, in the model, R31 is faster than R32. Formaldehyde decomposition at the surface is excluded because it is less significant than homogeneous reactions above 500 °C, the typical temperature for methanol dehydrogenation. In the gas phase, radical reactions (R38 to R40) are the key propagation steps, with the ·H radical being

the most active. This mechanism is consistent with the observed product distributions of H_2, CH_2O, CO, CH_4 and H_2O, where CO is mainly produced by gas-phase formaldehyde decomposition. Methane formation via R39 occurs parallel to CH_2O formation (R38). Since the thermal decomposition of methanol (R32) is negligible, the methane selectivity depends on the rates of R39 and R40. R39 is significantly slower than R38.

These observations emphasize the significance of surface reactions on the catalyst, specifically how the accumulation of hydrogen can block active sites and hinder further reactions. It underscores the importance of managing surface conditions to optimize catalytic performance. By identifying hydrogen desorption as an important process, this chapter suggests that improving it, possibly through catalyst modifications such as mixing sodium carbonate with active carbon materials or transition metals, can effectively improve catalytic activity. This provides a compelling basis for further research in this field.

The deactivation of the carbonate catalyst can be related to two main factors: the consumption of sodium during the reaction process and the accumulation of coke on the catalyst surface [63]. Both processes lead to a decrease in the amount of sodium released at a given temperature, which affects the effectiveness of the catalyst. As reported in [64] sodium carbonate is stable even in temperatures up to 850 °C, therefore the coke formation comes mostly from the side reaction during the process. To effectively recover the catalyst, a method involving the use of a mixture of oxygen and an inert gas can be used to burn off coke deposits. This process is essential for restoring the activity of the catalyst. The oxygen in the mixture reacts with the carbonaceous coke material on the catalyst surface, effectively removing it. The experimental utilization of these findings can be found in 6.5.

2.5 Direct resistance heating and ceramic sponges

Industrial production processes account for approximately one-third of the global energy demand [65]. Industries such as food, paper, chemicals, refining and metallurgy, in particular, are high-energy consumers. Heating for industrial applications is achieved by the combustion of various fuels, which can be solid, liquid or gaseous. Commonly used sources include fossil fuels, such as oil, natural gas and coal; and biomass sources, such as vegetable oil, wood chips, cellulose and ethanol

[66]. The temperatures generated by these fuels can range from 150 °C to more than 1600 °C [67, 68]. The efficacy of a process heating system is contingent upon its ability to deliver the desired product quality within specified parameters, such as high capacity and rapid response time. In essence, an optimal system will provide a high-quality product at the lowest cost, while an energy-efficient system will do so with the least amount of energy.

DRH is an excellent alternative to conventional heating methods in industrial applications. This technique uses an electric current, which flows through a resistor and converts electrical energy into thermal energy. DRH is almost 100% energy efficient, as it converts nearly all the electrical energy into heat [69]. This high efficiency translates to significant energy savings, with some applications reporting up to 80% energy savings compared to traditional heating methods [70]. In addition, one of the key benefits of the DRH is its ability to achieve a rapid heating rate. The heating process can also be easily regulated by changing the electrical current, allowing precise temperature control [69]. Moreover, the DRH can be particularly beneficial when combined with renewable energy sources, offering a synergistic approach to sustainable and efficient heating in various industrial applications. This combination offers advantages such as creating a more environmentally friendly and cost-effective heating solution [4, 71–73]. As the direct dehydrogenation of methanol to formaldehyde is an energy-intensive process and requires precise temperature control, the DRH concept was chosen to be tested within this work. A detailed description of the reactor can be found in Section 3.3.

Porous sponges represent a promising substitute for conventional internal components used in process engineering equipment including chemical reactors and separation columns [74]. These highly porous, three-dimensional structures, typically manufactured from ceramic compounds such as alumina (Al_2O_3), mullite ($3Al_2O_3 \cdot 2SiO_2$), or silicon carbide (SiC), but also metallic materials like nickel (Ni) or copper (Cu), offer a combination of properties that make them particularly suitable for the enhancement of heat and mass transfer processes [75]. Their structure offers a large surface area relative to their volume, which makes them ideal for applications requiring high surface interactions, such as filtration, catalytic reactions, and heat exchangers. Compared with widely used standard fillings, they exhibit low-pressure drops and outstanding heat transfer properties [76].

Ceramic sponges can be produced by several methods, such as direct foaming, the sacrificial template method and the replica technique [77]. The replica method is the most popular process for the production of open-cell ceramic foams [78]. The process starts with the utilization of an open-cell polymer foam, typically derived from polyurethane, which serves as the template. The polymer foam is initially submerged in a ceramic slurry, thereby enabling the slurry to adhere to the foam's internal structure. Once any residual slurry is removed, the coated foam is subjected to a drying process in preparation for the subsequent stage. The crucial phase of the production process occurs during sintering, whereby the polymer is burned off, leaving behind a rigid ceramic structure that replicates the original foam's porous architectural design. The sintering process not only solidifies the ceramic material but also creates a network of interconnected pores, resulting in a highly porous material with a significant surface area. The final ceramic sponge retains the three-dimensional network of the polymer template, thereby ensuring permeability to fluids and suitability for a range of applications in process engineering. The properties of the ceramic sponges, including their porosity and structural integrity, can be modified by modifying the composition of the ceramic slurry and the parameters of the sintering process.

Nowadays, 3D printing of ceramic sponges is also an innovative technique that enables the production of highly customized porous materials with precise control over their structure [79]. The process starts with the design of a 3D model of the desired sponge, followed by the preparation of a ceramic slurry consisting of ceramic powders, binders and additives to improve printability. During the printing phase, the ceramic material is deposited layer by layer according to the 3D model using methods such as direct ink writing, stereolithography or robocasting. After printing, the structure is dried to remove solvents and then usually subjected to debinding and sintering, which burns away the organic components to form a dense ceramic sponge with interconnected pores. This process allows the formation of complex geometries and tailored porosity, making 3D printed ceramic sponges suitable for a variety of applications including catalysis, filtration and effective heat management. The benefits of this approach include the ability to create intricate designs that are difficult to achieve with traditional manufacturing techniques [80].

Nevertheless, ceramic sponges are not without their own peculiar characteristics and inherent limitations. The compressive strength of ceramic sponges is relatively low due

to their high porosity [81]. The installation of ceramic sponges in large reactors can present some challenges e.g. a sponge must be tightly sealed to prevent liquid/gas bypasses. Furthermore, the current manufacturing processes, which are primarily focused on single-use metal melt filters, can result in variations in, for example, cell diameters.

Ceramic sponges made from silicon-infiltrated silicon carbide (SiSiC) were chosen to be used in the DRH concept due to their remarkable heat transfer properties and high mechanical strength at elevated temperatures [82–84]. The continuous solid phase of ceramic sponges enables efficient heat conduction, both radially and axially, consequently reducing heat transfer resistances and eliminating cold spots in the reactor. Moreover, SiSiC exhibits excellent resistance to most acids and alkalis, making it suitable for use in chemically aggressive environments while remaining chemically inert towards substrates and products [85, 86].

To conclude, a sponge has a dual function, not only is it a resistor for the DRH, but it is also used as a support (body) for the catalyst (Na_2CO_3) in the direct dehydrogenation of methanol to water-free formaldehyde process. Further information regarding sponges and experimental methodology can be found in Section 3.3. The test procedure and results of the SiSiC sponges and the DRH reactor are described in Chapter 6.

3. EXPERIMENTAL SETUPS

For the purpose of experimental research, the sodium evaporation and condensation system and the Medena mini-plant were constructed. Next, modifications (DRH concept) to the setup were undertaken. Detailed descriptions of these units are provided in the following.

3.1 Sodium evaporation and condensation setup

When developing a process that requires the use of a catalyst, establishing a reliable catalyst dosing system is a critical step. In the vapor catalyst dosing approach, it is essential to accurately determine the amount of evaporated sodium and ensure its uniform distribution over time. As previously mentioned in Section 2.2.1, the sodium catalyst dosing system has not yet been evaluated in detail. To address this, a sodium evaporation and condensation apparatus was designed and constructed. Its primary function is to effectively control the sodium amount during the reaction. Figure 7 shows a simplified technical illustration of the sodium evaporation and condensation unit. This demonstrates its main components and provides a basic overview of its operation. In general, the setup consists of a sodium evaporator (bubble column) and sodium condenser. The liquid sodium was first heated up under an inert atmosphere, then argon was bubbled through the column, and finally sodium vapor was condensed in the second vessel.

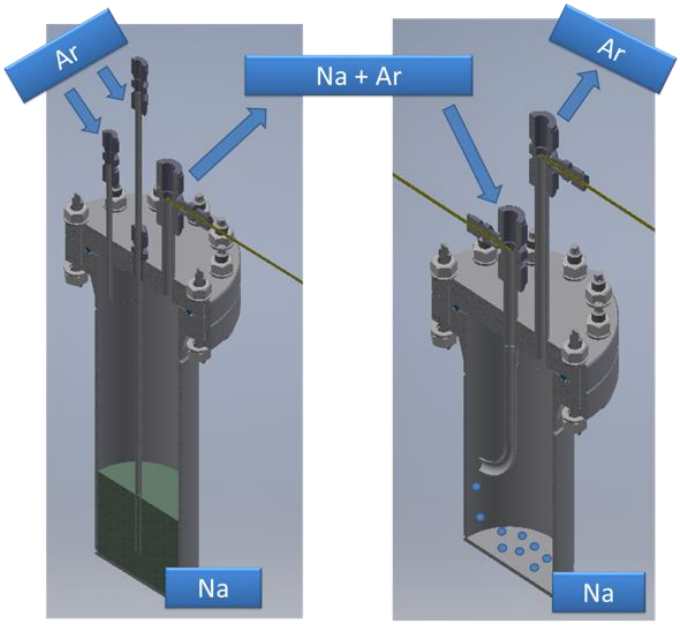

Figure 7. Technical illustration of the sodium bubble column and condenser, CAD drawings by M. Daubner

Figure 8 shows the process flow diagram of the system:

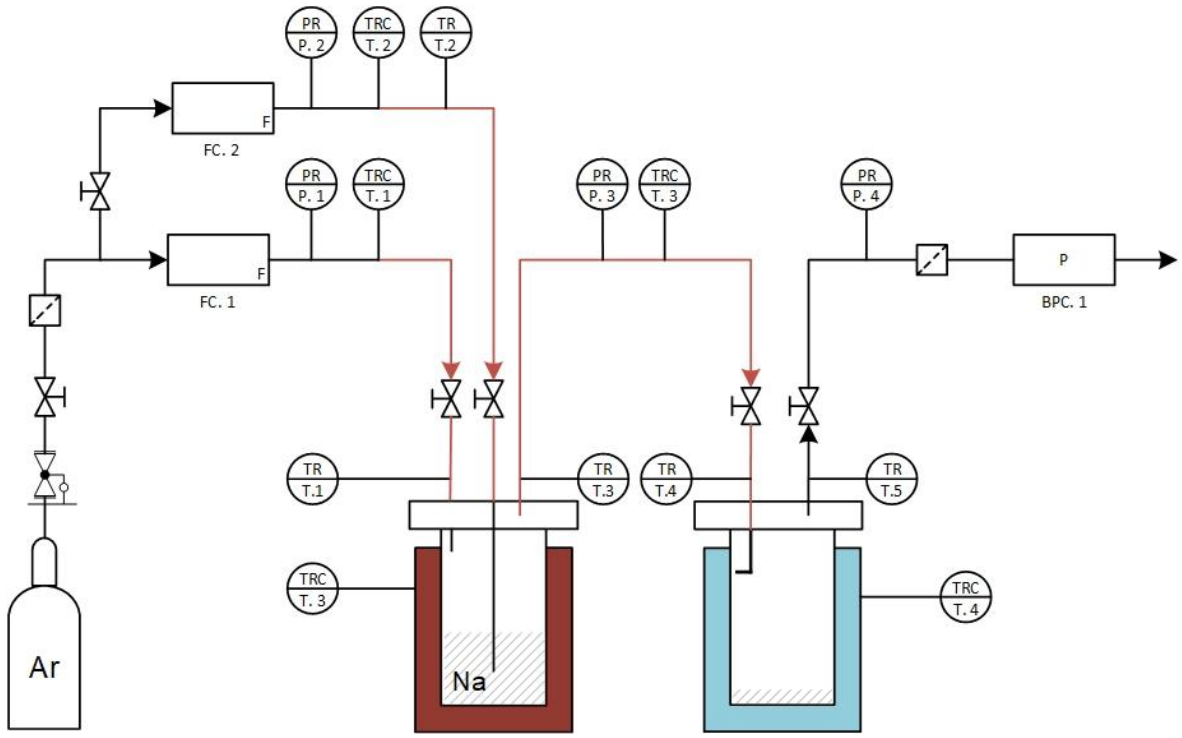

Figure 8. Process flow diagram of the sodium evaporation and condensation units

The evaporation unit (dark red) consists of a 1.3-litre bubble column in which sodium was heated by a 700 W heating jacket. The argon flow, which is critical to the process, is controlled by two independent flow regulators, specifically the Bronkhorst model F- 201CV-2K0-PGD-33-K. One regulator is dedicated to a shortened pipe (referred to as FC.1), while the other controls the flow for the primary bubble pipe (FC.2). In the next stage of the process, after the sodium has evaporated, it is condensed in a specially designed vessel (light blue). This container was placed in a cooling bath (ThermoFlex 350) filled with silicone oil at -20 °C. This arrangement ensures efficient condensation of the sodium vapor back into a solid form. At the end of each experiment, a thorough inspection of the condenser was carried out. Typically, sodium was observed to either deposit at the bottom of the condenser, adhere to the inner wall or exhibit a combination of both behaviors, as shown in Figure 9. To quantify the efficiency and effectiveness of the evaporation and condensation process, the total amount of sodium that had evaporated and then condensed was measured by weighing. This step is crucial in assessing the performance of the system and making any necessary adjustments to optimize the process.

Figure 9. Photograph of sodium in the condenser after an experiment, photograph: M. Kamienowska-Orsini

To ensure accurate temperature monitoring within the system, Class 1 IEC 60584 Type K thermocouples, encased in Inconel 600 with MgO insulation and a 3 mm outside diameter, are placed inside the pipes and at both the inlet and outlet points of the containers. The pipelines are heated by means of heating tapes from Horst GmbH. The pressure was monitored using a Rosemount 2051 inline pressure transmitter from Emerson. In addition, a Bronkhorst back pressure controller BPC.1 (P-502C-1K1R-PGD-39-K + F-001AV-LFU-33-K) allows the system pressure to be set in the mini-plant.

The sodium bubble column tested in this work was originally based on the concept developed by Ruf [29]. However, to improve the process stability and verify the actual amount of evaporated sodium, modifications were made. Furthermore, to meet the increased capacity requirements of mini-plants, a scale-up of the bubble column was performed. These modifications are given in Table 3. which provides details of the changes made to the original design to accommodate the extended scope of operation.

Table 3. Comparison between the previously tested column and our own work

Sodium bubble column	**This work**	**Ruf** [29]
Volume, l	1.3	0.1
Height, mm	248	120
Inner diameter, mm	82.5	34
Inert gas dosing	2 flow controllers	1 flow controller
Purification system	Zr foil	none
Sodium loading	up to 800 g	up to 60 g

The integration of a secondary flow controller into the system is an important enhancement for managing the gas flow through the bubble pipe. By maintaining a stable flow, the secondary flow controller contributes significantly to the overall operational stability of the system. In addition to the flow controller, a back pressure controller has also been incorporated. This controller is key for adjusting the pressure within the system. This ensures that the operating parameters are not only maintained consistently but also kept within the specified optimum ranges and safety thresholds. Such precise pressure control is important to the proper operation and stability of the system.

3.2 MEDENA mini-plant

A self-constructed laboratory setup, shown in Figure 10, was used for the experimental methanol dehydrogenation tests. The process flow diagram for methanol dehydrogenation in this experimental setup, as shown in Figure 11, includes a series of steps:

1. Preheating and feeding: methanol & argon (feed), together with sodium & argon (catalyst) were preheated and then fed into the reactor. Argon was controlled by a flow controller (FC. 3) and passed through a particulate filter. Methanol (99.9 %, AcroSeal) was supplied via a mass flow controller (FC. 4) to an evaporator type W-202A-330-K (CEM) whose temperature was set at 120 °C. Argon and methanol flows were then mixed in CEM. The SS 316 tubes for the methanol stream were coated with Silcolloy 1000 (made of high-purity silicon, providing temperature

stability and preventing corrosion). The methanol flow rate was set between 8 and 20 g h^{-1}, accompanied by an appropriate amount of argon flow. Different amounts of catalyst were tested, ranging from 0.0 to 0.5 g h^{-1}.

2. Reactor: The dehydrogenation reaction was carried out in a tubular reactor with an internal diameter of 10 mm and a length of 45 cm, the reactor pipe was made of Alloy 625 (2.4856). The reactor pipe was heated by a three-zone oven with a total power output of 3000 W. Reaction conditions were maintained at a temperature of 500–950 °C and a pressure of 1.2–1.5 bar. Detailed temperature evaluation in MEDENA mini-plant is described in Section 4.5.
3. Measurement and control: The temperatures inside the tubes and the reactor were measured using thermocouples. The system pressure was monitored using the equipment described in Section 3.1, and a back pressure regulator was used for partial pressure control. The unanalyzed product stream was absorbed in a water solution in a gas scrubber (Buechi - Gas scrubber DN50 / 6 l) to ensure safe handling of the chemicals. The product stream was analyzed using a gas chromatograph (ARNEL 6453, Perkin Elmer) equipped with a main column (Molesieve 5A) and a precolumn (Plot U). The system used a backflush-to-vent mechanism in a heated external oven to remove contaminants. The gas chromatograph was equipped with a thermal conductivity detector, a methanizer and a flame ionization detector. The carrier gas, argon (99.9999 %, Air Liquide), was further purified by various traps. A flow controller (FC. 5) ensured constant flow through the valves of the gas chromatograph.

Figure 10. Picture of the MEDENA setup, photograph: M. Kamienowska-Orsini

A significant modification to the catalyst system in MEDENA is the absence of the sodium condenser. While sodium evaporation and condensation experiments were essential to determine stable catalyst dosing, the use of a condenser as a cooler is not a viable option for the main product stream, which consists mainly of hydrogen and formaldehyde. The rapid and uncontrolled cooling of this stream would result in formaldehyde decomposition, which occurs at temperatures below 140 °C [31]. Consequently, the recovery of the catalyst was not pursued during the experiments detailed in this thesis. However, developing an effective method for recovering sodium is essential for scaling up the process to an industrial scale.

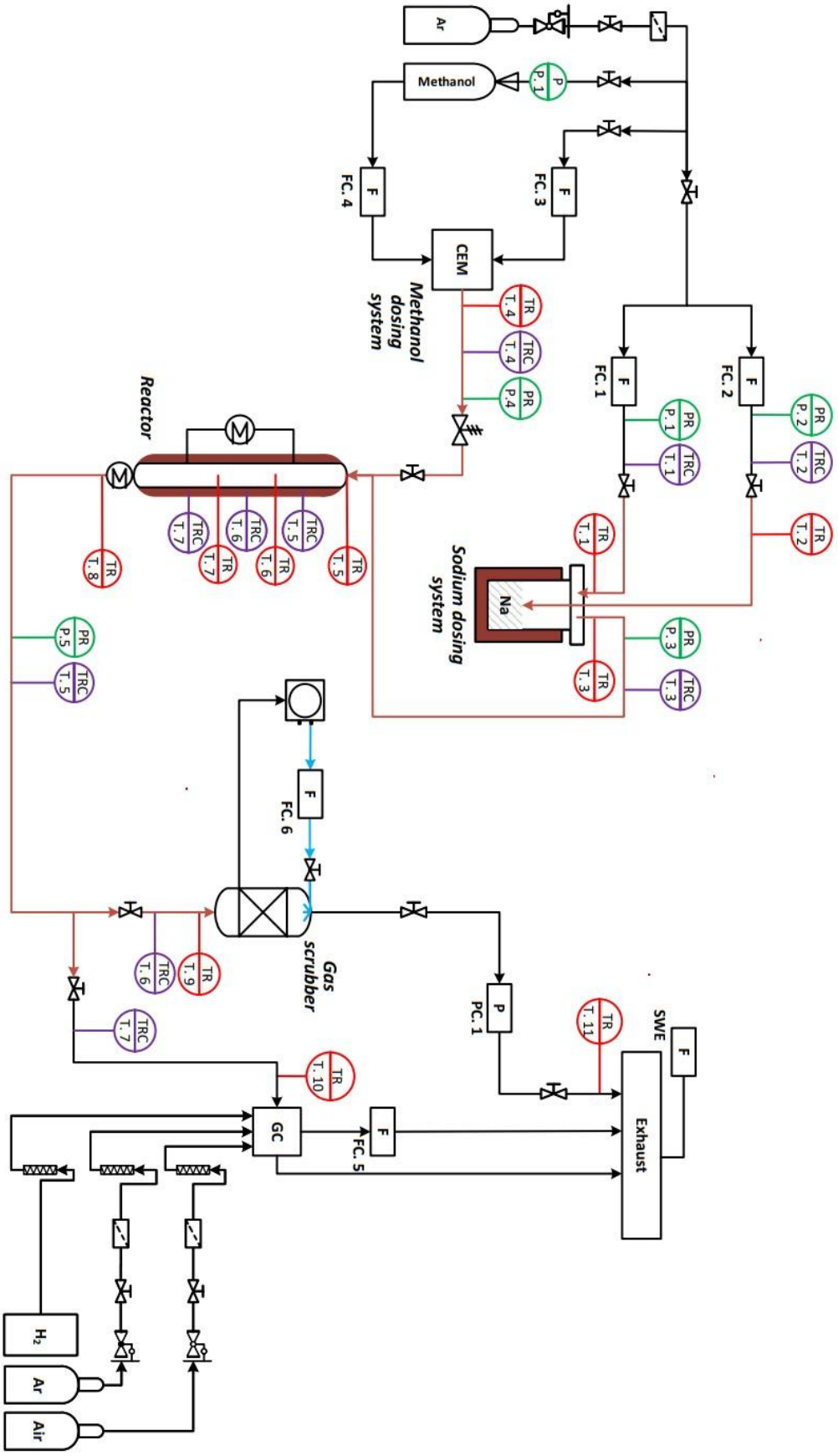

Figure 11. Process flow diagram of the MEDENA mini-plant

The process parameters in the MEDENA mini-plant were set and controlled by a programmable logic controller (PLC) system. The Siemens PLC enabled both the configuration and real-time monitoring of key process variables such as temperatures, pressures and flow rates, directly via the control panel interface (Figure 12). In addition, automated alarm thresholds and emergency shutdown functions were programmed for each parameter to ensure operational safety. When a value approached or exceeded these limits, the system autonomously initiated corrective adjustments and triggered visual and audible alarms. Furthermore, monitoring of the off-gas composition (H_2, CO, and CH_2O) was also integrated into the control system. The process data were systematically recorded at one-second intervals and stored for subsequent analysis.

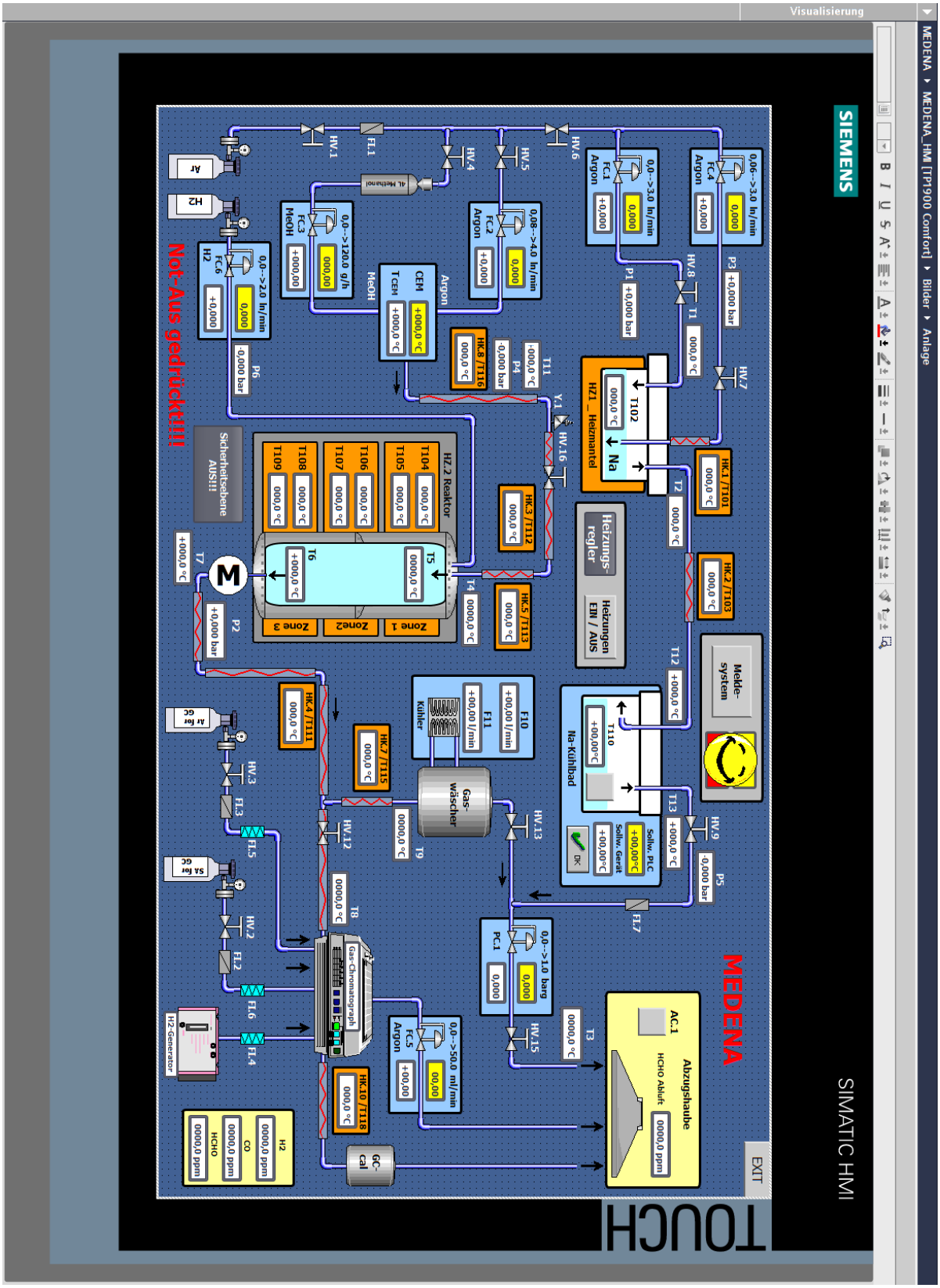

Figure 12. Control panel of the mini-plant

3.3 MEDENA mini-plant with direct resistance heating reactor

To evaluate and test the DRH reactor, several modifications were implemented in the MEDENA mini-plant. The process flow diagram is shown in Figure 13. The experimental tests of methanol dehydrogenation were conducted in a self-constructed laboratory setup, equipped with a DRH reactor (material: 2.4663, ID 44 mm, OD 54 mm). The temperatures inside the reactor were measured with thermocouples (type K, class 1 according to IEC 60584; Inconel 600; insulation MgO; and OD 3 mm) protected by a macro material insulating sleeve. The reactor contains two nickel Helicoflex seals supplied by the Technetics Group. The power supply was provided by a Voltcarft DPPS-32-30, possible output 1–32 VDC, 0–30 A, with an input of 220–240 V, 50/60 Hz. Feedthrough adapters (pin/conductor material - nickel, temperature range: 269 °C to 450 °C, withstanding maximum pressure at 20 °C: 103 bar; maximum current: 31.5 A; manufactured by Hositrad) were used to supply power from the electricity source to the nickel wires. The argon and methanol dosing units remained unchanged, as did the gas scrubber and the GC system.

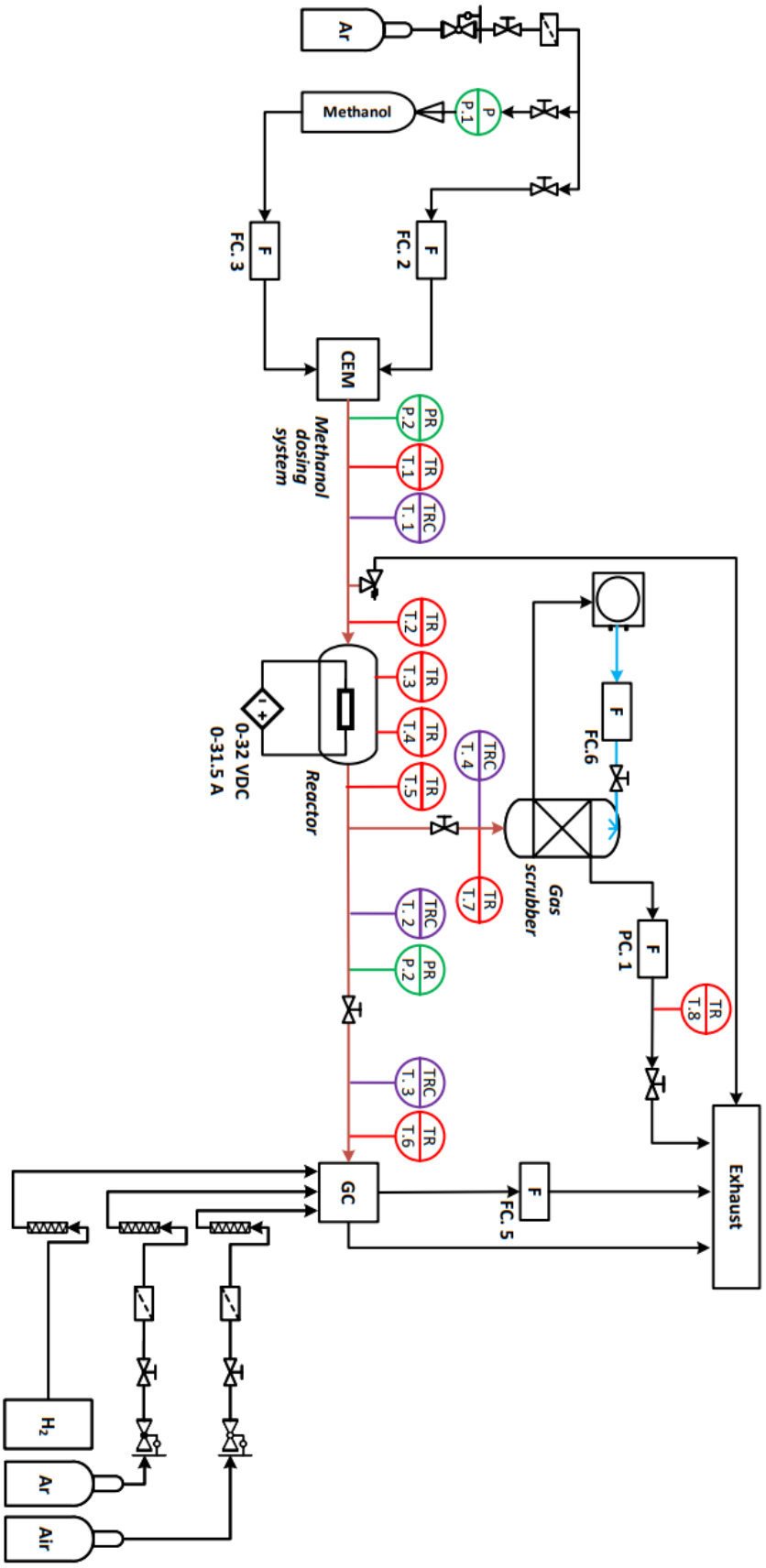

Figure 13. Diagram of the MEDENA mini-plant for tests using the DRH concept

As described in Section 2.5., ceramic sponges were chosen to be tested in the MEDENA mini-plant with DRH system. The sponges presented in this thesis can be classified into two main categories: those produced using the replica technique and those created through 3D printing. The 10, 20 and 30 PPI silicon-infiltrated silicon carbide sponges (Figure 14) were produced by EngiCer SA (replication method). Additionally, a 20 PPI sponge (Figure 15) with a solid layer (5 mm) was 3D-printed by an Engicer SA. The principal objective was to ascertain whether the potential for creating a customized 3D-printed structure would indeed enhance the performance during the dehydrogenation process in the DRH concept. In addition, the primary goal of the solid layer surrounding the sponges was to facilitate tighter contact between the sponge surface and the nickel rings/plates, as detailed in the subsequent section.

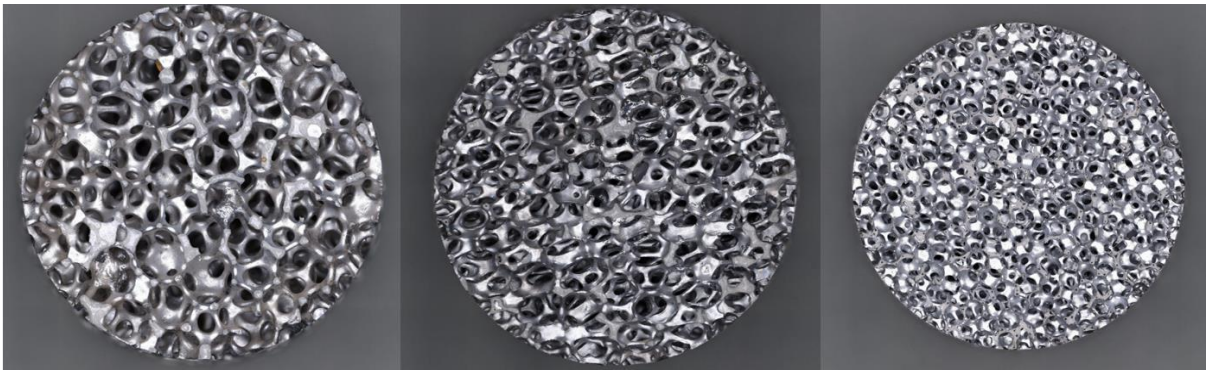

Figure 14. 10, 20 and 30 PPI SiSiC ceramic sponges (OD: 38 mm), photographs: M. Kamienowska-Orsini

Figure 15. 20 PPI SiSiC 3D-printed sponge (OD: 38 mm), photograph: M. Kamienowska-Orsini

Design of the direct resistance heating reactor

The integration of a directly heated sponge into a reactor requires a particular design approach. The initial concept, developed at the KIT Technik Haus, is shown in the technical drawing in Figure 16. This design consists of nickel rings to supply current to the sponge and the special macro-insulation structure, which was custom made for the

size of the reactor and sponge. During the preliminary trials, the high temperature resulted in deformation of the nickel rings, which subsequently lost contact with the sponge and caused a discontinuation of the current flow. Images of this concept are shown in Figure 17.

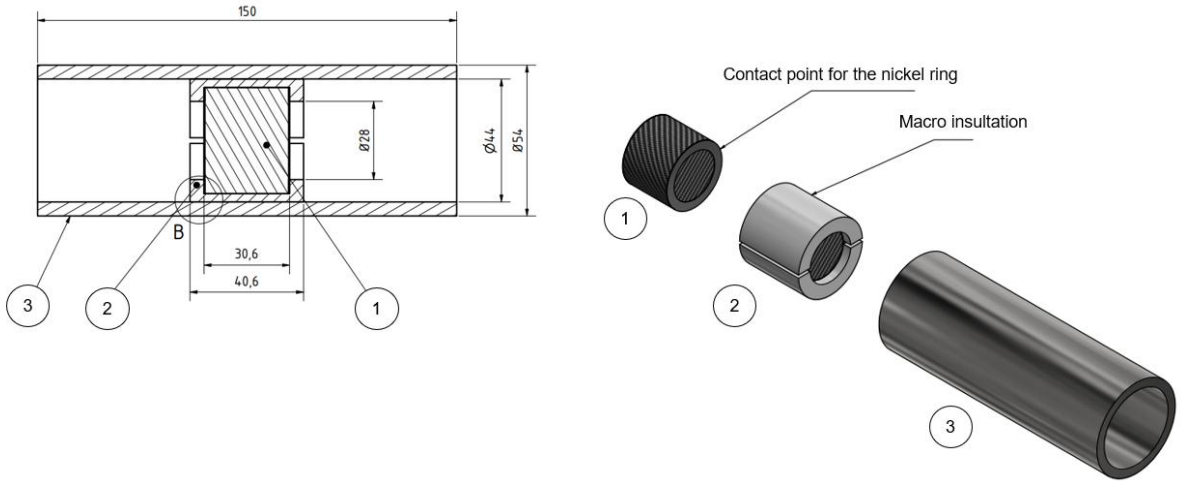

Figure 16. Technical illustration of the first DRH reactor concept, author: D. Kuntz

Figure 17. Images of the first concept using nickel rings instead of nickel plates, photographs: M. Kamienowska-Orsini

The initial tests demonstrated that the nickel rings were inadequate for maintaining a constant current flow throughout the process. Consequently, in the next step, they were replaced with nickel plates. A significant aspect of the design is the positioning of nickel plates on the sides of the sponge (Figure 18). These plates are pressed together using a macro-insulating material. This concept proved highly effective in

enabling a constant current flow through the sponge across the full temperature range, as detailed in Section 4.6.2.

Figure 18. Macro insulation with a nickel plate and wire (with ceramic insulation beads (OD: 1.5 mm) connected to a copper adapter (photograph: M. Kamienowska-Orsini)

The electrical resistance of a 20 PPI SiSiC sponge was measured at KIT Technik Haus and was found to be 10 Ohm cm. A zirconium foil was used to carefully position the ceramic sponge, along with the macro insulation material, into the reactor. This foil was placed between the reactor wall and the insulation and ensured that the macro material was not damaged during the insertion. The detailed scheme of this reactor concept is illustrated in Figure 19, and a photograph of the reactor is shown in Figure 20. The reactor was designed for a maximum overpressure of 0.5 barg.

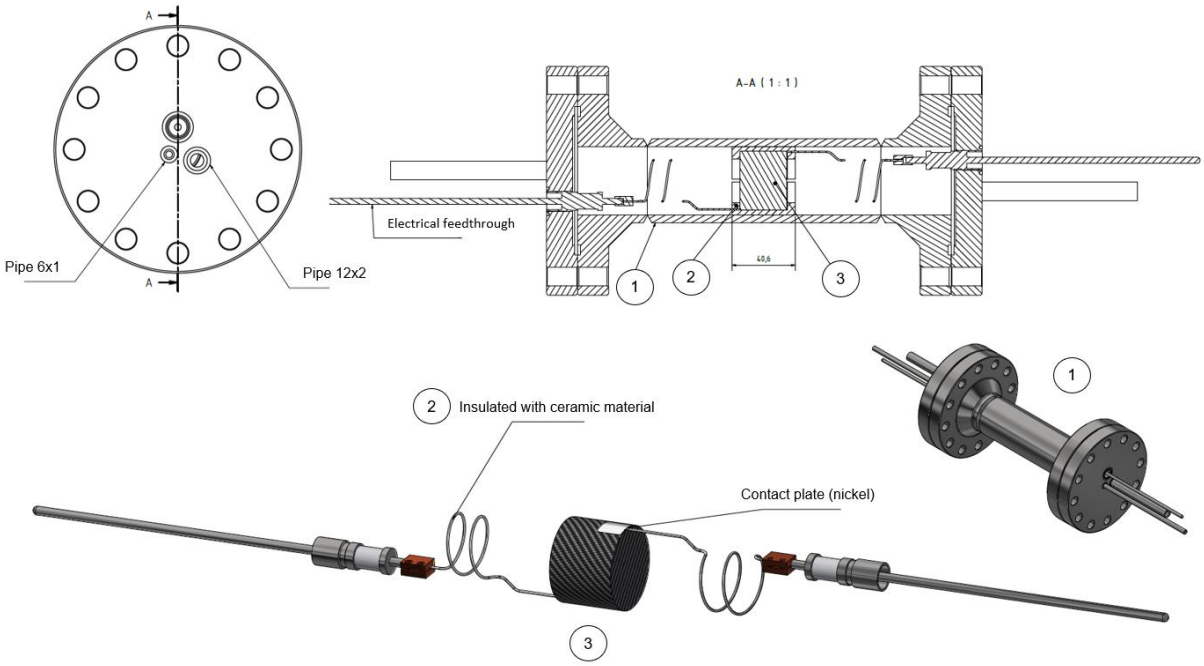

Figure 19. Technical illustration of the DRH reactor concept, author: D. Kuntz

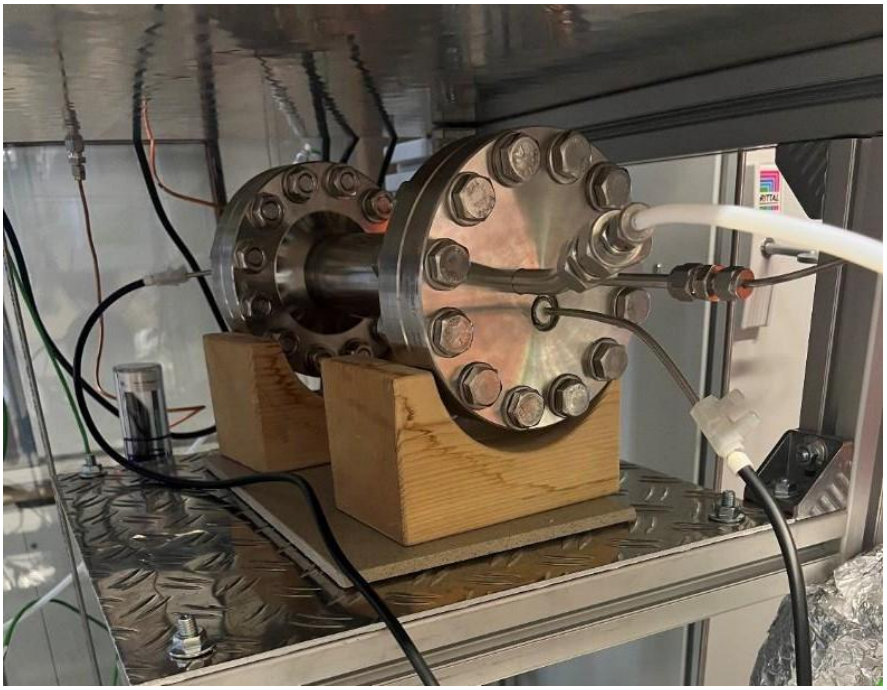

Figure 20. DRH reactor in the MEDENA mini-plant, photograph: M. Kamienowska-Orsini

4. EXPERIMENTAL TECHNIQUES AND EVALUATION

This chapter describes the experimental methods and evaluations carried out to establish the effectiveness of the proposed systems. It outlines the theoretical determination of the amount of evaporated sodium, followed by an investigation of sodium handling practices and material compatibility. The evaluation of sodium methoxide as an alternative catalyst is then presented. Subsequently, the principles of reactor design are elucidated. This is followed by an evaluation of the reaction temperature in the MEDENA mini-plant, focusing on how the temperature profile of the reactor changes under different operating conditions. Blank experiments were performed and described to analyze the temperature distribution within the reactor without a catalyst, using different methanol concentrations and flow rates. Lastly, the temperature evaluation for the direct resistance heating concept is discussed. This includes the determination of the resistivity of the sponges used in the system and blank experiments carried out to evaluate the temperature profile under an argon atmosphere using this heating method.

4.1 Methodology for the theoretical determination of the amount of evaporated sodium

A crucial aspect of this work is the quantification of the amount of sodium evaporated using the bubble column concept. These investigations are essential as no experimental verification of this type was previously carried out for this type of system. The Raoult-Dalton equation was used to estimate the amount of evaporated sodium. This equation describes the phase equilibrium between the liquid sodium phase and the molar fraction of sodium in the gas phase. It applies to ideal gases and liquid phases where $\tilde{x}_{i,Ph}$ represents the mole fraction of component i in the liquid phase, p^*_i is the equilibrium vapor pressure of the pure component, $\tilde{y}_{i,Ph}$ is the partial pressure of component i in the gas phase and p is the total vapor pressure of the solution. The equation is presented as follows (Eq. 1):

$$\tilde{x}_{i,Ph} \cdot p^*_i = \tilde{y}_{i,Ph} \cdot p \qquad \text{Eq. 1}$$

For the bubble column, the liquid phase consists of only one component; therefore, $\tilde{x}_{i,Ph} = 1$. Since $\tilde{y}_{i,Ph} \ll 1$, one can assume $\tilde{y}_{i,Ph} \approx \tilde{Y}_{i,Ph}$. The Raoult-Dalton equation therefore reduces to (Eq. 2):

$$\widetilde{Y}_{i,Ph} = \frac{p^*_i}{p} \qquad \text{Eq. 2}$$

The vapor pressure of a substance is a function of temperature. As the temperature increases, the vapor pressure generally increases exponentially. This is described by the Antoine equation (Eq. 3). For sodium, a relatively minor change in temperature can lead to a considerable change in vapor pressure. The equilibrium vapor pressure is determined by the following Antoine equation [43]:

$$\log p = 10.182516 - \left(\frac{5693.8766}{T}\right) - (1.0948 \log T) + 8.5874946 \times 10^{-5} T \qquad \text{Eq. 3}$$

The formula provides a value for the vapor pressure in kPa for temperatures between 300 and 2500 K. The molar flow of argon can be calculated from the volumetric flow using Eq. 4, where p_{Norm} is 101325 Pa, T_{Norm} = 273.15 K and $\widetilde{R}$ = 8.312 J mol^{-1} K^{-1}:

$$\dot{N}_{Ar} = \frac{p_{Norm} \cdot \dot{V}_{Ar}}{\widetilde{R} \cdot T_{Norm}} \qquad \text{Eq. 4}$$

The balance of moles in the bubble column is given in Eq. 5, in which $\dot{N}$ are the molar flows of sodium and argon, respectively:

$$\frac{d\dot{N}_{Na}}{dt} = 0 = \dot{N}_{Ar} \cdot \left(\widetilde{Y}_{Na,in} - \widetilde{Y}_{Na,out}\right) + \dot{N}_{Na} \qquad \text{Eq. 5}$$

It is assumed that the process in the column is in a steady state. As there is no sodium in the argon stream entering the bubble column, $\widetilde{Y}_{Na,in} = 0$. This gives (Eq. 6):

$$\dot{N}_{Na} = \dot{N}_{Ar} \cdot \widetilde{Y}_{Na,out} \qquad \text{Eq. 6}$$

Furthermore, assuming that $\widetilde{Y}_{Na,out} = \widetilde{Y}_{Na,Ph}$, since the loading of sodium in the gas phase at the interface is the same as the loading of sodium in the gaseous bulk phase, the mass flow of sodium ($\dot{m}_{Na}$) can be estimated with (Eq. 7):

$$\dot{m}_{Na} = \dot{N}_{Na} \cdot \widetilde{M}_{Na} \qquad \text{Eq. 7}$$

A description of the temperature changes in argon at the outlet of the bubble column is crucial for studying sodium evaporation from the bubble column. In the absence of an in-situ temperature measurement inside the bubble column, there is inevitable uncertainty with regard to the exact temperature of the sodium. In particular, since the argon outlet temperature only reaches 250 °C, it is concluded that mass transfer is unlikely to occur at the expected 500 °C. This conclusion holds even if the heating power is adequate and the theoretical energy ratio for both sodium and argon heating is met. The considerations are therefore as follows (Eq. 8):

$dh = c_p dT$ for a constant c_p value: $h - h_0 = c_p(T - T_0)$ Eq. 8

Under the assumption of a constant isobaric heat capacity over the considered temperature range, the specific enthalpy can be evaluated by Eq. 9, which leads to Eqs. 10 and 11:

$$h(p,T) = h_0(p,T_0) + c_p \cdot (T - T_0)$$ Eq. 9

$$\dot{H}(p,T) = h(p,T)\,\dot{m}$$ Eq. 10

$$\frac{dH_{\text{Bubble column}}}{dt} = \dot{Q}^{in} - \dot{Q}^{out} + \dot{H}^{in} - \dot{H}^{out}$$ Eq. 11

The sodium bubble column was continuously heated by a 700 W jacket. Eq. 12 is obtained in which η is an efficiency of an electric heater:

$$\dot{Q}^{in} = P_{el}\,\eta$$ Eq. 12

According to the first law of thermodynamics, Eq. 13 can be used to calculate the enthalpy flow entering the bubble column:

$$\Delta\dot{H}^{in} = \dot{m}_{Ar} \cdot (h_{Ar,0}(p,T_0) + c_{p,Ar}(T_{Ar}^{in}) \cdot [T_{Ar}^{in} - T_0] + \dot{m}_{Na}(h_{Na,0}(p,T_0) + c_{p,Na}(T_{Na}^{LV}) \cdot [T_{Na}^{LV} - T_0] + \Delta h_{Na}^{LV})$$ Eq. 13

The enthalpy flow leaving the bubble column consists of argon and evaporated sodium at equal temperatures (Eq. 14):

$$\Delta\dot{H}^{out} = \dot{m}_{Ar} \cdot (h_{Ar,0}(p,T_0) + c_{p,Ar}(T_{Ar-Na}^{out}) \cdot [T_{Ar-Na}^{out} - T_0]) + \dot{m}_{Na}(h_{Na,0}(p,T_0) + c_{p,Na}(T_{Ar-Na}^{out}) \cdot [T_{Ar-Na}^{out} - T_0]) + \dot{m}_{Ar-Na}\Delta h_{Ar-Na}^{Mix}$$ Eq. 14

When argon and sodium mix, molecular interactions cause the combined enthalpy flux of the individual streams to differ from that of the mixed stream. However, due to the negligible amount of sodium in the stream, this effect has been neglected. The heat flow leaving the system is equal to the heat loss of the column and the pipes (Eq. 15):

$$\dot{Q}^{out} = \sum_{losses} \dot{Q}$$ Eq. 15

This evaluation showed a very positive change in the enthalpy of the bubble column, implying that no further heat consumption to reduce the enthalpy, such as cooling of the sodium, occurs within the column. To further justify the temperature assumption, it is essential to consider the energy required to heat argon at a flow rate of 3 l min^{-1}. The energy input needed to raise the temperature of the argon from an inlet temperature of 150°C to the assumed temperature of 500°C is approximately 25 J s^{-1}.

The difference between the calculated and observed exit temperatures of argon highlights the many complexities of the system and the possible deviations from the theoretically predicted values. In the course of evaluating the dynamics of the system, it became noticeable that the argon outlet temperature consistently deviated from the initially predicted values. This led to an extension of the model used. To resolve this issue, mass transfer calculations were specifically performed using an adjusted reference temperature of 400 °C. This modified value is not only in agreement with the data obtained but is also supported by a number of experimental results, making it a highly plausible and representative scenario for further analysis. Considering the mass transfer of sodium into the argon bubbles, the evaporation rate is given by (Eq. 16), where A_B is the interfacial area between the sodium bubble and the argon, β is the mass transfer coefficient and c is the concentration of sodium vapor at the interface with the liquid phase and in the main argon stream.

$$\dot{N}_{Na} = A_B \, \beta \, (c_{Ph} - c_{B,\infty}) \qquad \text{Eq. 16}$$

The Sherwood number (Sh) was used to calculate the mass transfer coefficient (Eq. 31), where d_B is a bubble diameter.

$$Sh = \frac{\beta \cdot d_B}{D} \qquad \text{Eq. 17}$$

The diffusion coefficient (D) was calculated from Aref'yev's equation [87] (Eq. 18):

$$D = 1.05 \cdot 10^{-4} (T/723)^{1.65} \qquad \text{Eq. 18}$$

For a comprehensive analysis of the behavior and properties of sodium within the bubble column, the most important parameters, such as bubble diameter shape and regime were calculated. Table 4 provides values related to both the sodium bubble column itself and the bubbles formed within it. The presented results were calculated based on the equations listed in Ref. [88]. The equations used to evaluate the properties associated with the bubble column are shown in the following section.

Table 4. Relevant dimensionless numbers for the bubble column

Argon flow, l min^{-1}	**0.8**	**1.2**	**1.5**	**3**
Reynolds number of the orifice, -	173	260	325	650
Reynolds number of the bubble, -	26077	30349	33345	46333
Bubble diameter, mm	11.9	13.5	14.6	18.9
Ascent Velocity Mendelson, m·s^{-1}	0.30	0.31	0.31	0.34
Froude Number, -	0.78	0.72	0.69	0.61
Weber Number, -	6	7	7	11
Morton Number, -	$4.69 \cdot 10^{-16}$			
Eötvös Number, -	7	9	11	18
Regime, -	Constant frequency regime			
Shape, -	Nonspherical			

In the particular case of a sodium bubble column purged with different argon flows, the obtained parameters provide valuable insights into the behavior and performance of the system. A more detailed evaluation of the findings and their impact on the process is given:

- Argon flow rate: Changing the argon flow rate can affect the distribution and dispersion of bubbles within the sodium column. Higher flow rates can result in more vigorous mixing and dispersion of the bubbles, potentially affecting the overall heat and mass transfer characteristics of the system.
- Reynolds number of the orifice: This number characterizes the flow regime through the orifice shown in Eq. 19, where u_o is the velocity of the gas at the orifice, ρ_L is the density of the liquid sodium, d_o is the diameter of the orifice and η_L is the dynamic viscosity of the liquid sodium [89].

$$\mathrm{Re_o} = \frac{\mathrm{u_O \rho_L d_O}}{\mathrm{\eta_L}} \qquad \text{Eq. 19}$$

Reynolds numbers indicate differences in the degree of turbulence or laminar flow, which can influence bubble formation, size distribution and dispersion within the column [90].

- Bubble Reynolds number: This parameter provides an insight into the flow regime around the bubbles formed in the sodium column, as seen in Eq. 20, where u_B is the velocity of the bubble, d_B is the diameter of the bubble and ν_L is the kinematic viscosity of liquid sodium [89].

$$Re_B = \frac{u_B d_B}{\nu_L} \qquad \text{Eq. 20}$$

Higher Reynolds numbers indicate more turbulent flow around the bubbles, which can affect their behavior, residence time and coalescence within the column [61, 62].

- Bubble diameter: This value was calculated by means of the Gaddis and Vogelpohl equation, [93] (Eq. 21), where $\dot{V}_G$ is the volume flow of argon.

$$d_B = \left[\left(\frac{6 d_o \sigma_L}{\rho_L g}\right)^{\frac{4}{3}} + \left(\frac{81 \nu_L \dot{V}_G}{\pi g}\right) + \left(\frac{135 \dot{V}_G^2}{4\pi^2 g}\right)^{\frac{4}{5}}\right]^{\frac{1}{4}} \qquad \text{Eq. 21}$$

The change in bubble diameter can affect the surface area to volume ratio of the bubbles and, therefore, their heat and mass transfer characteristics. Larger bubbles may rise faster but may also coalesce more easily, altering the overall flow dynamics within the column [94].

- Ascent Velocity Mendelson: Bubble rising velocity was calculated using the Mendelson equation (Eq.22) [95], which is recommended for the nonspherical bubbles [88].

$$u_B = \sqrt{\frac{2\sigma_L}{d_B \rho_L} + \frac{g d_B}{2}} \qquad \text{Eq. 22}$$

The ascent velocity of the bubbles influences their residence time in the column and their interaction with the surrounding sodium [96]. Differences in ascent velocity can affect the distribution and mixing of the bubbles, thus affecting the efficiency of heat and mass transfer processes.

- Froude number: It helps to characterize the flow regime within the column as shown in Eq. 23 [89].

$$\mathrm{Fr_B} = \frac{u_B^2}{g d_B} \qquad \text{Eq. 23}$$

Changes in the Froude number indicate differences in the relative importance of inertial and gravitational forces, which can affect bubble rising velocities, bubble breakup and overall flow stability [97, 98]. When the Froude number is less than 1, the flow is classified as subcritical. In this case, the flow is characterized by a smooth flow pattern.

- Weber number: This reflects the importance of surface tension forces compared to inertial forces, as can be seen in Eq. 24, where σ_L is the surface tension of the liquid sodium.

$$\mathrm{We_B} = \frac{d_B u_B^2 \rho_L}{\sigma_L} \qquad \text{Eq. 24}$$

This parameter influences bubble deformation, breakup and coalescence behavior within the column, thereby affecting bubble size distribution and gas-liquid interface area [69, 70]. Bernadin et al. [101] categorized Weber numbers into three ranges: low (We < 30), medium (30 < We < 80) and high (We > 80). Research on low Weber numbers indicates that higher static contact angles are associated with lower wetting limit temperatures.

- Morton number: This relates buoyancy and surface tension effects to inertial forces [89], as shown in Eq. 25:

$$\mathrm{Mo} = \frac{\mu_L^4 \Delta\rho g}{\rho_L^2 \sigma_L^3} \qquad \text{Eq. 25}$$

Variations in the Morton number can affect bubble break-up and coalescence phenomena, which in turn affect bubble size distribution and flow stability within the column. Low Mo numbers are typical of liquid metal systems and yet no better approach for their calculation has been proposed [102].

- Eötvös number: This number reflects changes in the relative importance of gravitational and surface tension forces [89], as can be seen in Eq. 26:

$$\mathrm{Eo} = \frac{\Delta\rho g d_B^2}{\sigma_L} \qquad \text{Eq. 26}$$

In many fluid systems, particularly those on small scales or involving different phases, a low Eötvös number indicates a significant influence of surface tension. This can affect bubble shape, deformation and break-up behavior,

which, in turn, affects bubble rising velocities and residence times within the column [103].

In summary, the analysis shows that the bubbles formed in the sodium bubble column have nonspherical shapes, and that their formation occurs within a constant frequency range over different argon flow rates. This indicates stable and predictable behavior within this range of operating conditions.

4.2 Sodium handling and material compatibility

The handling of sodium in experimental and industrial facilities presents significant practical challenges due to its high chemical reactivity. Sodium's tendency to induce corrosion, as discussed in Section 2.2.2, contributes to these difficulties, particularly in systems in which material durability is critical. Initial experiments of sodium evaporation and condensation setup (Section 3.1) revealed inefficiencies in the operation of the bubble column, primarily due to the passivation of sodium. This passivation significantly hindered the system's performance, particularly impacting the reliability of the catalyst dosing unit. To address these challenges, several factors were systematically assessed, including trials of different sodium purity grades, the use of alternative gasket materials for the bubble column, and techniques to mitigate sodium passivation. In addition, the selection of appropriate valve types and pipeline coatings was studied. Sodium loading procedures and effective equipment cleaning protocols were also reviewed.

These investigations aimed to ensure optimal system performance, improve reliability, and prevent further passivation, thereby enhancing the overall corrosion resistance and functionality of the setup in high-temperature environments. This section provides a detailed analysis of the techniques identified and applied within the MEDENA mini-plant, emphasizing the lessons learned and the critical importance of maintaining system purity for long-term operational stability.

In the present dissertation, the choice of materials and purification techniques was based on previous research [29, 47, 49–51, 87, 104]. Firstly, the loading of sodium into the bubble column was always conducted within a glove box, maintaining an inert atmosphere. Furthermore, the sodium was consistently held in an argon environment in the mini-plant. Nevertheless, corrosion appeared and hindered the evaporation

process. The corrosion phenomena observed in this work can be divided into two categories:

- corrosion in pure sodium, primarily involving the dissolution of SS alloy constituents in liquid metal
- corrosion due to impurities acting on the SS alloy elements

The latter category is particularly important since oxygen dissolved in sodium can react with protective metal oxide layers on SS alloys, leading to the formation of metal oxides and deposits that compromise the integrity of the alloy. Two different levels of sodium purity were tested in the primary experiments. One was 99.8% pure sodium, supplied by Sigma-Aldrich, and the other had a higher purity, specifically an ER grade of 99.98%, supplied by Métaux Spéciaux. The use of these two grades of sodium allowed a comprehensive assessment of how different levels of purity might affect the evaporation process. The chemical compositions of the sodium used in these tests are detailed in Table 5 and provide valuable information for understanding how even the smallest amount of different impurities present in the sodium may affect the performance of the system.

Table 5. Chemical composition of the tested sodium

	Trial #1	**Trial #2**
Compound	S+ Grade	ER Grade
Na, %	99.80	99.98
Ca, ppm	< 400	< 10
K, ppm	< 300	< 10
Cl + Br, ppm	< 20	< 20

In order to identify the elements causing issues during the process, inductively coupled plasma (ICP) analyses of various sodium layers were carried out with the courtesy of the Institute of Catalysis Research and Technology (IKFT-KIT) (Figure 21). Elements such as Ca, K, Fr and Zn were detected in these measurements.

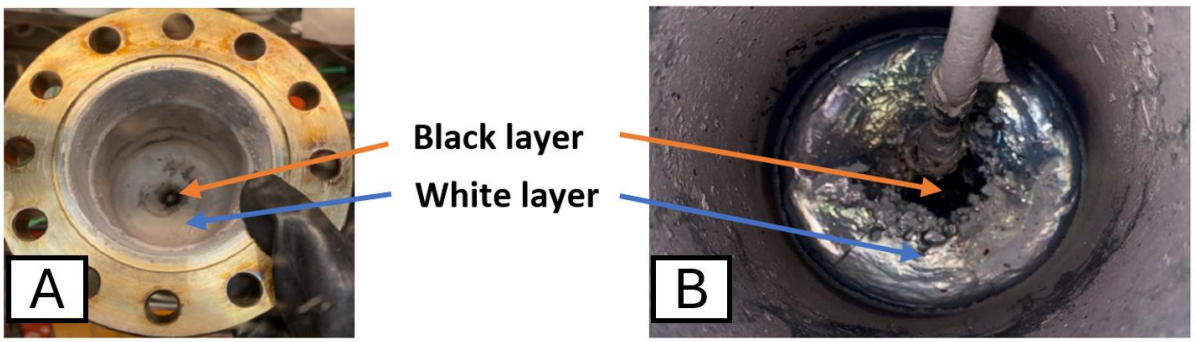

Figure 21. Images of sodium (Trial #1) in the bubble column after experiments before the implementation of Zr foil, photographs: M. Kamienowska-Orsini

The use of high-purity sodium with minimal amounts of calcium and potassium was critical for the evaporation process. Even small traces of impurities significantly affected the behavior of the sodium in the experimental setup (Figure 21: A – visible white oxide layer - melting temperature greater than 1000 °C). The presence of water and oxygen could lead to the formation of calcium oxide and calcium hydroxide by reacting with calcium. Similarly, reactions with potassium can produce potassium oxide and potassium hydroxide in the presence of impurities. Compounds of iron and zinc, from SS 316Ti components and the decomposition of the gasket material (Fe) were also observed (Figure 21: A and B – black layer).

In order to overcome the challenges posed by impurities, which hindered a stable evaporation process, a new gasket was introduced, made from nickel. This step was combined with the integration of zirconium foil as a sodium purifier agent [104]. The latter was selected on the basis of its ability to effectively remove impurities from sodium - Zr foil acts as a getter by chemically binding oxygen, thus reducing the oxygen concentration in the sodium, thereby ensuring a higher level of purity of both the sodium and the setup used for the experiments. After replacing the gasket, using ER Grade, and inserting three pieces of Zr foil (0.1mm thick, 99.98%), the sodium evaporation and condensation setup became operational. Nevertheless, the corrosive nature of sodium led to the replacement of several pipelines during the sodium evaporation and condensation experiments. Moreover, certain components, such as ball valves (e.g. Swagelok: SS-45TS12MM, SS-S63PS12MM) were found to be unsuitable due to their tendency to clog within minutes of operation. This resulted in a slowing down of experimental progress and the necessity for frequent adjustments. In order to ensure optimal functionality, certain valves were removed. The results of

the sodium evaporation and condensation tests conducted following the implementation of the aforementioned changes can be found in Section 5.1.

Following the successful completion of sodium evaporation and condensation experiments, the subsequent objective was to undertake material compatibility tests on 2.4856 for the sodium, methanol and argon stream mixture at elevated temperatures (600–900 °C). During trials, the carbon deposits blocked the reactor and the chemical wear on the reactor´s inner surface was visible. The scanning electron microscopy (SEM) analysis (Figure 22) of the deposits found at the outlet of the reactor was conducted after the initial material stability experiment.

Figure 22. SEM analysis of compounds at the outlet of the reactor

Table 6 provides a detailed summary of the elemental composition of the deposits, both in terms of mass percent and atomic percent. It can be concluded that the high levels of carbon (22.98 wt%) indicate the significant presence of carbon deposits. Given the high sodium content (31.02 wt%), it is plausible that oxygen reacted with sodium to form sodium oxide, a common occurrence in environments where sodium is exposed to atmospheric conditions. In addition, the presence of metals such as iron, chromium, nickel, copper and zinc in the deposits is an indication of corrosion. These metals are often components of the materials used in reactors and other experimental equipment.

Table 6. SEM results of the compounds at the outlet of the reactor

Element	Mass, %	Atom, %
C	22.98	35.25
O	30.41	35.02
Na	31.02	24.86
Al	0.14	0.10
Si	0.18	0.12
Cr	1.89	0.67
Fe	7.65	2.53
Ni	0.90	0.28
Cu	0.47	0.14
Zn	2.11	0.60
Mo	2.24	0.43
Total:	100.00	100.00

In view of the corrosive nature of sodium and the lessons learned from previous sodium experiments, the following materials were also tested: 1.4841, 2.4663 and 2.4856 with a SiSiC inner tube. All of these materials were found to have short service lives and were typically blocked by carbon deposits due to corrosion. This required the application of a protective coating to the reactor (2.4856) and other critical components of the system. A technique known as aluminizing was used to address this problem. In this process, aluminum is diffused into a base metal to form a protective coating that is resilient and does not spall or flake. This procedure was carried out by the company: Diffusion Alloys (UK) Ltd. The resulting aluminide layer imparts robust corrosion resistance to the base material. The reactor tubes, for example, were coated with this protective layer to a thickness of approximately 100 µm. A microscopy image of such a coated part is shown in Figure 23.

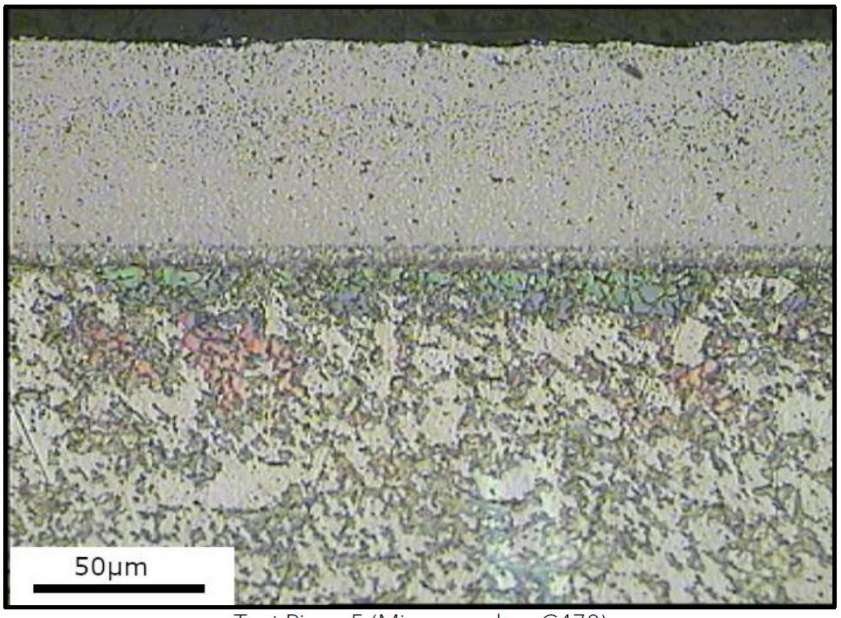

Figure 23. Microphotograph of a coated part, provided by a supplier

The choice of alumina as a coating was due to its chemical inertness [105]. This property makes it an effective barrier to sodium, preventing corrosion of the underlying materials. In addition, the hardness of alumina contributes to its resistance to abrasion and wear, which is particularly beneficial in demanding conditions. Another important attribute is its excellent thermal stability, which makes it suitable for use in environments subject to high temperatures or wide temperature variations [106]. Together, these properties ensure the longevity and integrity of reactor components under demanding experimental conditions. Trials of the coated reactor were successful, and corrosion in the area of the reactor was significantly reduced. The experimental results of the catalytic tests can be found in Section 5.3.

Overall, there is a potential risk when working with molten sodium in pipes and containers, as leaks can lead to spontaneous ignition if temperatures rise above 115 °C [42]. Rock wool or slag wool, with minimal free silica content, is the preferred material for the insulation of pipelines and vessels carrying sodium. For applications requiring higher temperatures, ceramic fibers are recommended. Insights made from molten materials, such as fibrous insulation, tend to absorb less moisture than their powdered or foamed counterparts, making them more favorable [61].

To sum up, the need to maintain an ultrapure environment is critical, as even trace amounts of oxygen and moisture react with sodium. The reaction with oxygen results

in the formation of an oxide layer on the surface of the sodium, with a melting temperature greater than 1000 °C [43], which prevents the effective evaporation of the sodium. In addition, the reactivity of sodium with certain system components, such as seals, led to corrosion of the bubble column. The enhancements such as the use of ER grade sodium, the insertion of Zr foil, the coating of the reactor and other SS316 elements are critical to the reliable operation of the sodium catalyst dosing unit.

4.3 Evaluation of sodium methoxide as the catalyst

Sodium methoxide was suggested and tested by Ruf [13] as a potential alternative catalyst to sodium vapor. To study this possibility in detail, thermogravimetric analysis (TGA) and differential scanning calorimetry (DSC) were conducted. The presentation of these test results was possible thanks to the support of the Institute of Catalysis Research and Technology (IKFT). TGA is an essential tool for assessment of the thermal stability of materials, allowing the temperature at which a material begins to decompose to be determined [107]. It enables the analysis of a material's composition by measuring weight loss at specific temperatures. TGA also provides insight into decomposition kinetics, which is essential for understanding process conditions and ensuring safety. The TGA curve of the sodium methoxide sample is shown below in Figure 24.

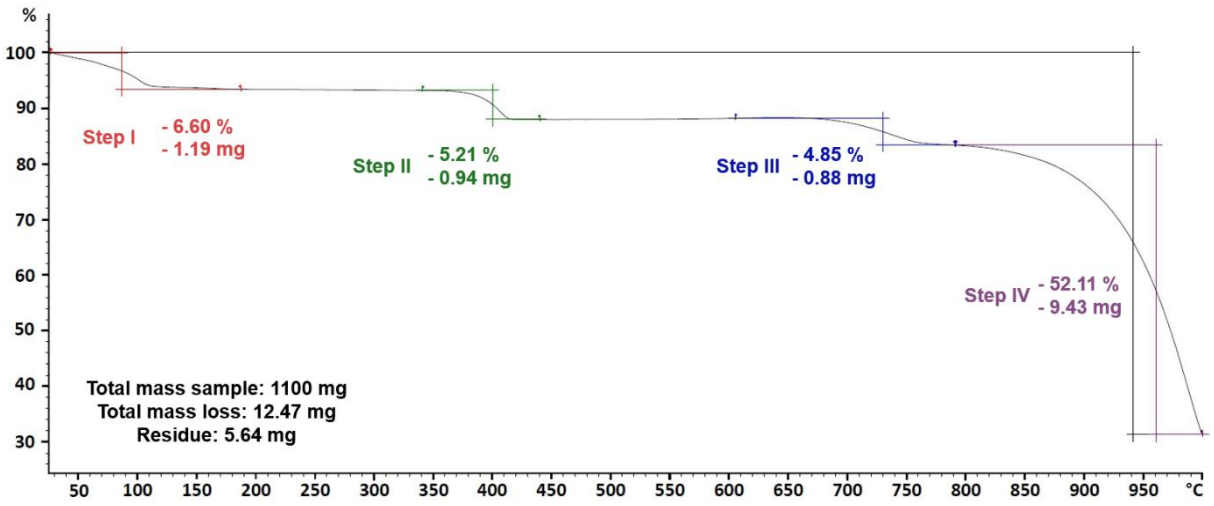

Figure 24. TGA of sodium methoxide

The analysis was conducted on 1100 mg of sodium methoxide under a nitrogen atmosphere. Four mass losses can be observed in the graph. The first mass loss is due to the evaporation of the alcohol produced by the reaction of sodium methoxide with water, which was absorbed from the environment during storage of the alcoholate

and during weighing of the sample. The reaction is not rapid due to the fact that the analysis was conducted in an inert gas atmosphere. At ca. 380 °C, there is the second mass loss, which is the decomposition of sodium methoxide (if the analysis had been conducted in an oxidizing gas atmosphere, this mass loss would have been observed in the lower temperature range). In this step, methane, ethane and propylene leave the test sample, while sodium carbonate, sodium hydroxide and carbon remain. [59]. These residues start to decompose at temperatures above 650 °C, with a rapid mass loss occurring at ca. 800°C. At 1000°C, the remaining material likely consists of sodium and other inorganic compounds, such as e.g., Na_2CO_3, Na_2O, NaOH, and C, which remain stable and do not decompose in an inert gas atmosphere at this temperature [42, 43].

DSC is a thermal analysis technique that measures how the heat capacity of a material changes with temperature [108]. It can detect transitions such as melting, crystallization and glass transition, which reflect changes in the physical properties of the material. DSC can also be used to investigate the purity of a substance by observing the melting range and estimating the energy associated with thermal transitions, providing valuable data for material evaluation. The DSC thermograph of sodium methoxide (4600 mg) is shown in Figure 25.

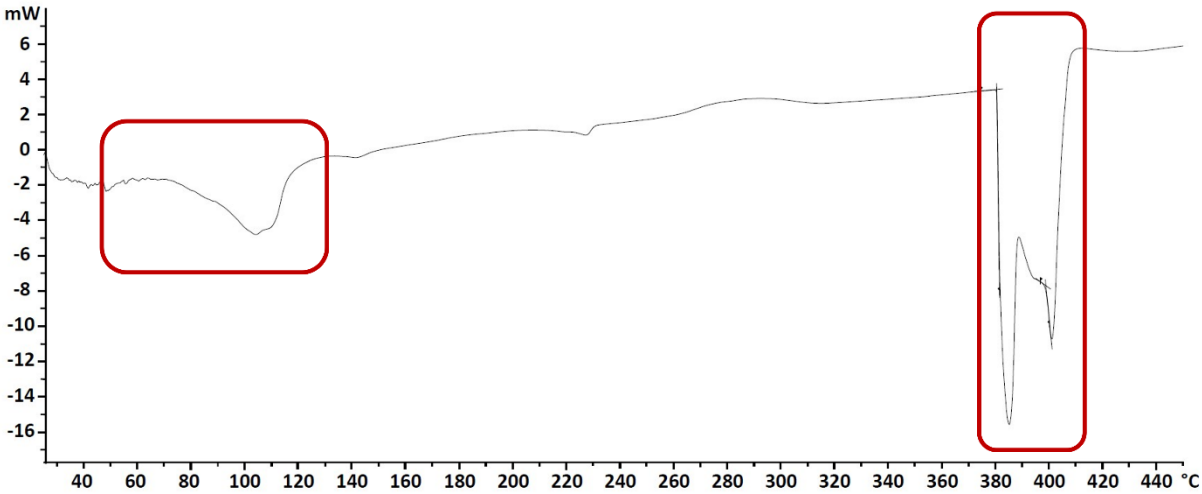

Figure 25. DSC thermogram of sodium methoxide

One small peak (ca. 100 °C) and sharp peaks at 381 and 398 °C can be observed. The endothermic transformation in the 80–120 °C range is the evaporation of the alcohol produced by the hydrolysis reaction of sodium methoxide with water (moisture absorbed from the environment during the storage of the alcoholate and during sample

weighing). The second endothermic transformation (between 380–410 °C) is the decomposition of sodium methoxide.

By combining the DSC and TGA data, it can be concluded that sodium methoxide is thermally stable in an inert gas atmosphere up to a temperature of 380 °C. Additionally, it is evident that sodium methoxide does not act as an active catalyst within the reaction temperature range, e.g., 500–1000 °C, as it decomposes before reaching this region. Therefore, it may be a sodium carbonate that shows activity when sodium methoxide is used as a catalyst (see Section 2.3).

4.4 Reactor design principle

The reactors tested in this dissertation are classified as tubular flow reactors (TFR) or plug flow reactors (PFR). The scheme is shown in Figure 26. The main characteristics of this reactor type, under ideal conditions, are discussed in the following section. In a PFR, the average concentration of reactants is higher than that in a continuous stirred tank reactor (CSTR) when both reactors operate at steady state with identical feed composition, flow rate, temperature, pressure, and target conversion. This difference arises from the absence of back mixing in PFR, which leads to a higher reaction rate and consequently a smaller reactor volume. It is one of the major advantages of a PFR. However, the PFR has limited temperature control, and unwanted temperature gradients can be formed within the reactor. In addition, deviations from ideal conditions can lead to unusual flow profiles and pressure drops within the reactor. As a result of these characteristics, PFRs are often used for reactions with short reaction times and high flow rates. These are mainly gas-phase reactions. PFRs are also used for high-temperature reactions and large-scale industrial production. Several examples of these applications include the high-pressure polymerization of ethylene, the combustion of sulfur dioxide and the synthesis of ammonia [109]. In addition to selecting the appropriate reactor type, several other design parameters are critical for optimizing reactor performance. These include determining the reactor dimensions, the operating temperature and pressure, the feed composition and the mass flow rate through the reactor. Each of these variables must be carefully calibrated to direct the reaction towards the desired product.

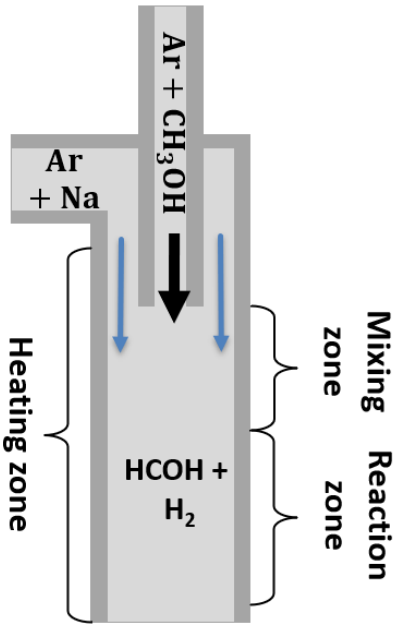

Figure 26. Simplified scheme of the reactor

This optimization process must adhere to fundamental principles of thermodynamics, chemical kinetics, fluid dynamics, and heat and mass transfer. Additionally, it is crucial to ensure that all variables comply with the constraints imposed by mass and energy balances, as this consistency is essential for the successful design and operation of the reactor.

In chemical kinetics, the reaction rate r is defined as the change of moles N over time t, typically per volume V (Eq. 27). The individual rates of the different reactants in a single reaction are related to each other by their stoichiometric coefficients ν (Eq. 28). As reactions are driven and controlled by the collisions and interactions of different particles, the reaction rate is dependent on temperature and concentration. This is given in Eq. 29. The concentration function is expressed as the product of all educts concentrations C with exponents representing the order of the reaction for a single reactant α. The sum of all exponents is the total order of the reaction n. The factor k is dependent on the temperature T and the reactions activation energy E_a. This is demonstrated by Arrhenius' law (Eq. 30), where k_0 is the pre-exponential factor and R is the gas constant [10].

$$r_j = \frac{1}{V} \cdot \frac{dN_j}{dt} \qquad \text{Eq. 27}$$

$$-\frac{r_A}{\nu_A} = \frac{r_P}{\nu_P} \quad \text{Eq. 28}$$

$$r_j = k \cdot \prod C_{A,j}^{\alpha_j} \; ; \; \sum \alpha_j = n \quad \text{Eq. 29}$$

$$k(T) = k_0 \cdot e^{-\left(\frac{E_a}{R \cdot T}\right)} \quad \text{Eq. 30}$$

To further describe a given chemical process, it is necessary to determine the conversion, selectivity and yield [110]. The conversion X_A of a reactant is defined as the fraction of reactant that has reacted out of the original amount (Eq. 31). Furthermore, in the case of multiple reactions, the selectivity $S_{P,A}$ is the ratio between the moles of desired product formed and the moles of reactant consumed (Eq. 32). The yield $Y_{P,A}$ is the ratio between the moles of the desired product formed and the moles of the reactant fed into the reactor (Eq. 33).

$$X_A = \frac{N_{A,0} - N_A}{N_{A,0}} \quad \text{Eq. 31}$$

$$S_{P,A} = \frac{\nu_A}{\nu_P} \cdot \frac{N_P - N_{P,0}}{N_{A,0} - N_A} \quad \text{Eq. 32}$$

$$Y_{P,A} = \frac{\nu_A}{\nu_P} \cdot \frac{N_P - N_{P,0}}{N_{A,0}} \quad \text{Eq. 33}$$

In continuous-flow reactors, the space time τ and its reciprocal, the space velocity s, are used to measure performance instead of the reaction time and velocity. For a steady flow, the space-time is defined as the ratio between the reactor volume V_R and the volumetric feed rate $\dot{V}_0$ (Eq. 34) [111]:

$$\tau = \frac{V_R}{\dot{V}_0} \quad \text{Eq. 34}$$

The mass balance of a PFR is carried out via a differential volume element dV (Figure 27). The feed is equal to the sum of the amount of the reacted substance and the

accumulation, and the latter is assumed to be 0 in the ideal case. This leads to Eq. 35. By integration and transformation, Eq. 36 is obtained.

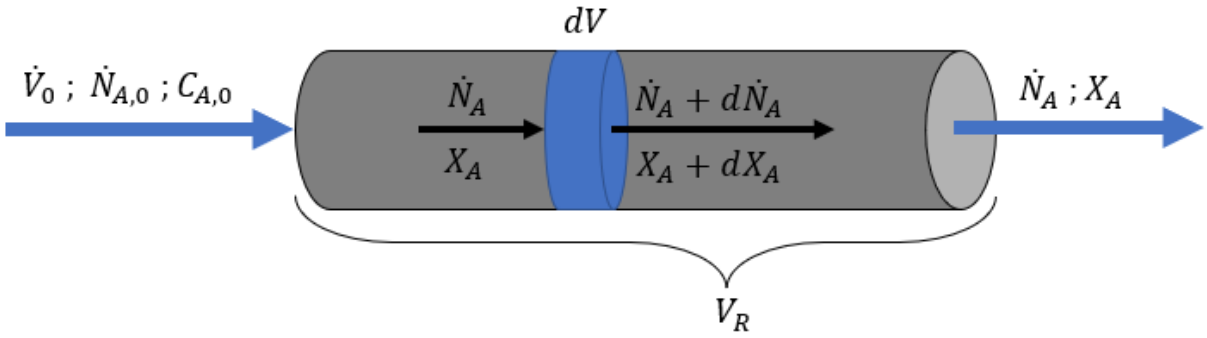

Figure 27. Material balance for a PFR; scheme prepared by [15], adapted from [111]

$$\dot{N}_A = \left(\dot{N}_A + d\dot{N}_A\right) + (-r_A)dV \qquad \text{Eq. 35}$$

$$\tau = C_{A,0} \cdot \int \frac{dX_A}{-r_A} \qquad \text{Eq. 36}$$

In the context of gas-phase reactions, two important parameters must be considered: the volume change due to the reaction, represented by the factor ε_A (as described in Eq. 37), and the changes due to temperature and pressure, p, with the compressibility factor z of the real gases, expressed by the factor π (shown in Eq. 38). These considerations lead to Eq. 39, which describes the relationship between the concentration of the reactants inside the reactor and their concentration at the entry point. Furthermore, when considering the reaction rate for gas-phase reactions, Eq. 29 is applied, which is based on the assumption of an irreversible, first-order reaction involving only educt A. This equation for the reaction rate is then integrated into Eq. 36, leading to the derivation of Eq. 40.

$$\varepsilon_A = \frac{\dot{V}(X_A = 1) - \dot{V}(X_A = 0)}{\dot{V}(X_A = 0)} \qquad \text{Eq. 37}$$

$$\pi = \frac{z_0 \cdot T_0 \cdot p}{z \cdot T \cdot p_0} \qquad \text{Eq. 38}$$

$$\frac{C_A}{C_{A,0}} = \frac{1 - X_A}{1 + \varepsilon_A X_A} \cdot \pi \qquad \text{Eq. 39}$$

$$k \cdot \tau \cdot \pi = -(1 + \varepsilon_A) \cdot \ln(1 - X_A) - \varepsilon_A X_A \qquad \text{Eq. 40}$$

This set of equations and the incorporation of various factors, such as ε_A and π, provide a comprehensive mathematical framework for analyzing and understanding the behavior of reactants and the progress of reactions within a gas-phase reactor, taking into account the intricate interplay of volume, temperature, pressure and reaction kinetics.

The MEDENA mini-plant was designed in accordance with the principles of engineering practice and the specific requirements of the methanol dehydrogenation reaction, as well as the relevant safety standards (e.g. material selections, maximum gas velocities). The main aim was to ensure the controlled flow of argon, sodium and methanol. Overall, the reactor can operate at temperatures up to 950 °C and pressures up to 1.5 bara. The system is also capable of handling total flow rates of up to 20 l min^{-1} under standard temperature and pressure (STP) conditions, with a maximum methanol throughput of 120 g h^{-1}. The design process involved careful consideration of the required ratio of inert gas to methanol and the amount of catalyst needed. This was also based on prior experimental studies and a comprehensive literature review (Section 2.1.2). A critical factor for optimizing the system's performance is the minimization of the residence time in the reactor. This is essential for achieving the desired reaction rates and for maximizing product selectivity. The following sections present the results of experimental trials conducted to test methanol concentrations ranging from 5 to 50 mol% (5–20 mol% are typical values cited in the literature as for example in [9, 17, 40]) The quantity of catalyst was estimated on the basis of the study by Ruf [29], thereby providing a reliable baseline for the operating parameters. The dehydrogenation reactions were conducted across a typical temperature range of 600 to 900 °C, in both atmospheric or slightly pressurized conditions (up to 1.5 bara). Given that residence time is inversely proportional to flow velocity within the reactor, a series of experiments were conducted to evaluate the impact of varying methanol and argon flow rates on the overall process efficiency and product yield.

4.5 Reaction temperature control evaluation in MEDENA mini-plant

In order to accurately determine the residence time and reaction zone in the MEDENA mini-plant, it was necessary to investigate the temperature profile of the reactor. For this purpose, a series of experiments and temperature measurements were carried out

in a '12 mm' Inconel reactor. First, a standard distribution was established with a pre-test using a pure argon stream. This was followed by blank reactions with methanol concentrations of 5 and 10 mol% in the argon stream. During these tests, the temperature in the heating oven was varied between 500 °C and 900 °C at 50 °C intervals to observe the effects of different temperatures on the reaction.

For accurate measurement of the temperature distribution, thermocouples encased in protective sheath were inserted into the reactor pipe, which was sealed with a Teflon gasket to prevent gas leakage. The thermocouples were positioned at defined intervals along the reactor axis, from the top of the reactor at 0 mm, 100 mm, 150 mm, 250 mm, 300 mm, 400 mm, 450 mm, and 550 mm, enabling precise determination of temperature gradients within the heated zone. The total length of the reactor was 600 mm. To ensure optimum reactor performance during testing, thermal insulation was applied above and below the heating oven to minimize heat loss and maintain a stable temperature within the reactor. The experimental setup is shown in Figure 28.

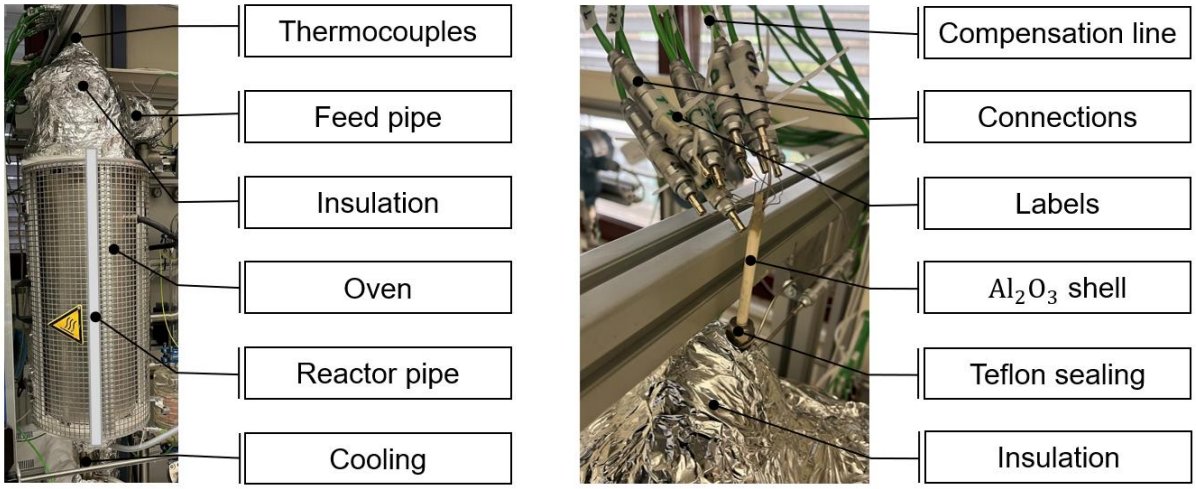

Figure 28. MEDENA setup used for the temperature distribution tests, photographs: M. Kamienowska-Orsini

Blank experiments

The principal objective of these tests is to demonstrate that the inlet gas stream can be heated to the designated temperature in an appropriate timeframe and to determine the length of the reaction zone within the reactor. To characterize the temperature distribution within the '12 mm' reactor without a catalyst, blank tests were carried out under varying conditions. A preliminary trial was carried out using a stream of pure argon at a flow rate of 1 l min^{-1}. This was followed by tests with 2 different methanol

concentrations in order to determine the basic methanol concentration influence on temperature distribution. Throughout all these tests, the pressure in the system was maintained at 1.1 bara. These varying test conditions were chosen to provide a comprehensive understanding of how different methanol concentrations and flow rates affect the temperature distribution during the reaction, thereby enabling a more detailed analysis of the reactor's performance under different operating scenarios.

The experimental procedure was carried out with the oven preheated to 600 °C. Measurements were performed and recorded over a period of approximately five minutes. Subsequently, the oven temperature was increased by 25 °C. The parameters were monitored until they stabilized, typically after approximately 15 minutes, at which time data points were collected again. The data used for acquisition included temperature measurements taken with thermocouples inside the reactor, as well as other temperature measurements at the relevant positions, pressures and flow rates. This process was repeated incrementally until a temperature of 900 °C was reached, which was the maximum operating temperature achievable with the furnace. The data were automatically recorded every second, and averages were calculated for each temperature plateau. Subsequent tests were carried out using argon flows containing 5 mol% methanol (8 g h^{-1} methanol and 1.9 l min^{-1} of argon), as shown in Figure 29, and 10 mol% methanol (10 g h^{-1} methanol and 1 l min^{-1} of argon), as presented in Figure 30.

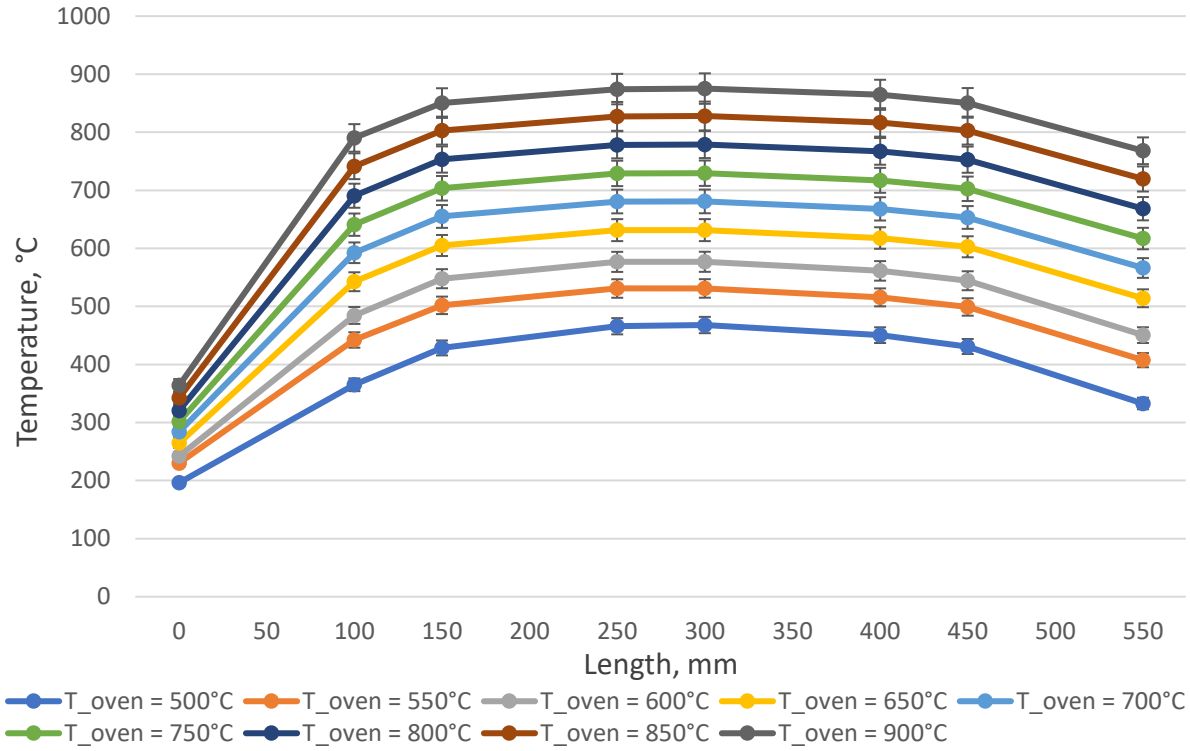

Figure 29. Temperature measurements during blank tests for 5 mol% MeOH [23][1]

The plots of the temperature profiles for the different experimental parameters show similar trends. Each graph shows a sharp increase in temperature immediately after the gas stream entered the heated zone of the reactor. This increase then gradually levels off to reach a peak temperature approximately at the center of the heated zone. It is noticeable that these peak temperatures are very close to the target temperatures of the oven. The largest deviation observed was 34 K below the set temperature of the furnace, which occurred in the test with a 5 mol% methanol concentration at a furnace temperature of 500 °C. In other scenarios, the temperature differences were approximately 20 K, with small fluctuations of up to 5 K. Overall, the presented results demonstrate a high degree of consistency and provide a solid foundation for further analysis of methanol concentrations and argon flows at varying levels.

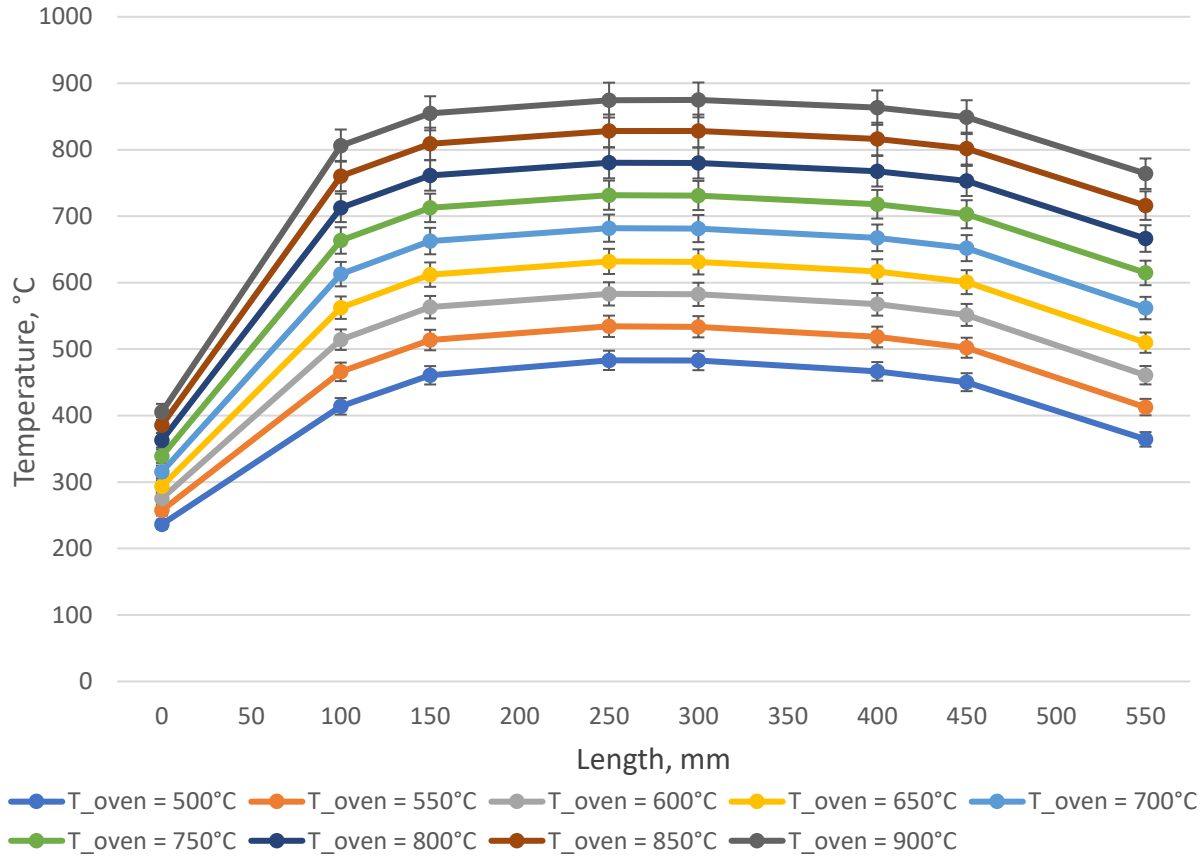

Figure 30. Temperature measurements during blank tests for 10 mol% MeOH [23][1]

For a more direct comparison of these temperature trends under different conditions, Figure 31 shows the graphs for the different cases but all at the same furnace temperature. According to the comparative analysis presented in the data, it is observed that the inlet temperature for the 5 mol% methanol is the lowest, while that of the pre-test with pure argon is the highest. This variation is attributed to the higher flow rate of the 5 mol% methanol stream, which results in a more significant initial cooling effect than that of the pure argon stream. Despite these initial temperature differences, the graphs converge towards similar maximum temperatures in the middle of the heated zone. This convergence indicates that, regardless of the initial inlet temperature and flow rate, the heating system is effective enough to bring all streams to nearly the same peak temperature at the center of the heated zone. However, after these peak temperatures are reached, the cooling patterns diverge slightly. The streams containing methanol had a slightly faster cooling rate than the pure argon stream. The space-time curve was calculated only for the reaction zone where the temperature was above 700 °C.

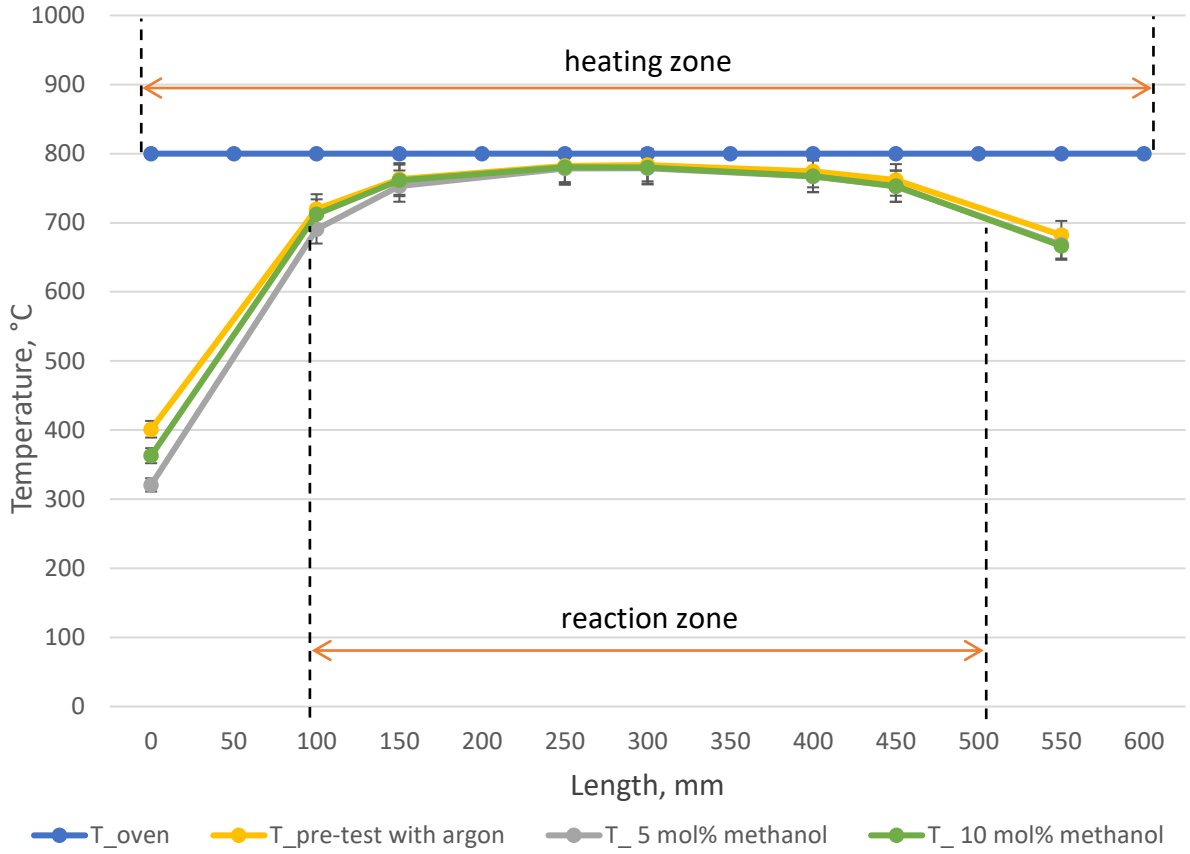

Figure 31. Temperature profiles of the reactor for the pre-tests with argon, 5 mol% and 10 mol% at 800 °C

Figure 31 also shows that for a furnace temperature of 800 °C, the reaction zone has a length of approximately 400 mm, which is 2/3 of the length of the heated zone. Using this length and the speed of the reaction temperature, the space-time (Table 7) can be calculated. All of the values are less than the desired 1 s (as explained in Section 2.1.2) and should result in obtaining a high yield of formaldehyde.

Table 7. Estimated space-time in the reaction zone

Case	$\tau\ (s)$
'12 mm' blank	0.304
'12mm' + TC & blank	0.133
'12mm' & catalyst	0.304

To sum up, these experiments proved that the inlet stream can be heated to the desired temperature of over 700 °C within the specified time frame, thus enabling the high conversion of methanol and high selectivity of formaldehyde, when the catalyst is

applied. The experimental results and analyses of the catalytic tests are described in Section 5.3.

4.6 Reaction temperature control evaluation in direct resistance heating concept

The implementation of the DRH concept in the Medena mini-plant required studies of temperature distribution. Initial tests focused on evaluating the resistivity of the sponges, with the aim of gaining a basic understanding of the effect of the number of pores per inch (PPI) on the electrical resistivity of the sponge. Following these tests, the basic temperature profile within the DRH system was analyzed. The goal of this study was to determine the range of the temperatures that could be achieved within the reactor, providing crucial data for optimizing the conditions for the dehydrogenation process.

4.6.1 Determination of the resistivity of the sponges

Initially, the resistance of the sponges in air was measured to estimate the power at 12 V (the maximum capacity of the electrical test equipment). The current was applied directly to the surface of the sponge via the cables from a power supply. The results are presented in Table 8, and the values were calculated by applying Joule's first law (Eq.41) [69]:

$$P = R \cdot I^2 \qquad \text{Eq. 41}$$

Table 8. Conditions and results of resistivity tests on ceramic materials for the DRH concept

Material	Voltage, V	Current, I	Resistance, Ω	Power, W
10 PPI sponge	12	10	1.2	120
20 PPI sponge	12	7.0	1.7	84
30 PPI sponge	12	4.5	2.7	54
Sponge partially impregnated with Na_2CO_3 (20 PPI)	12	4.0	3.0	48
SiSiC pipe (12 x 1.5 mm)	12	5.0	2.4	60

It can be concluded that the lower the PPI number, the higher the power that can be achieved, as the electrical resistance of the material is lower (owing to the thicker struts [112]). Furthermore, it is evident that the impregnation of the sponge with Na_2CO_3 resulted in a higher resistivity in comparison to the unimpregnated sponge. Given that sodium carbonate functions as an insulator, this increase in resistance is likely a consequence of the Na_2CO_3 filling the pores and creating barriers to electron flow within the ceramic structure. For the purpose of comparison, the resistance of a SiSiC pipe was also determined. The SiSiC pipe is characterized by a solid structure that provides a continuous path for electrical current. Thus, a concept using an electrically heated pipe could also be developed. However, the direct heating of the catalyst body is more advantageous in terms of heat efficiency.

Moreover, it should be noted that additional factors may also contribute to the observed resistivity, including material composition and microstructure etc. [113]. To illustrate, the silicon content of SiSiC materials can influence their electrical conductivity. A higher silicon (Si) content typically results in a lower resistivity, due to an increased concentration of charge carriers. This is attributed to the fact that Si acts as a dopant in SiC [112]. This phenomenon can be further explained by the formation of shallow donor levels in the SiC band structure, which increases the number of charge carriers. The relationship between Si content and resistivity is likely to follow a non-linear trend due to saturation effects at higher doping levels. The exact Si content in the pipe and the sponges was not disclosed by the supplier, therefore it is not possible to account for some of the trends in resistivity.

To conclude, the preliminary tests provided valuable insights into the electrical properties of the sponges, confirming the viability of utilizing them in DRH concept.

4.6.2 Blank experiments

The objective of the blank experiments was to demonstrate the proof of concept that SiSiC sponges are capable of providing sufficient heat to the reactor, and to examine the temperature distribution. The initial experiments evaluated the concept of DRH in an argon atmosphere shown in Figure 32 (T3 – temperature measured in front of the sponge, T4 – temperature measured behind the sponge). The mean temperature derived from the measurements of T3 and T4 was used to present and analyze the

results in the following parts of this dissertation. The procedure involved gradually increasing the electrical current to heat the reactor. Initially, the reactor was heated at 15 A for 30 minutes. The current was then increased to 20 A for an additional 30 minutes. The mean temperature of the reactor reached 525 °C after one hour. The reactor was then subjected to a current of 30 A for the next six hours; the maximum average temperature reached was ca. 670 °C.

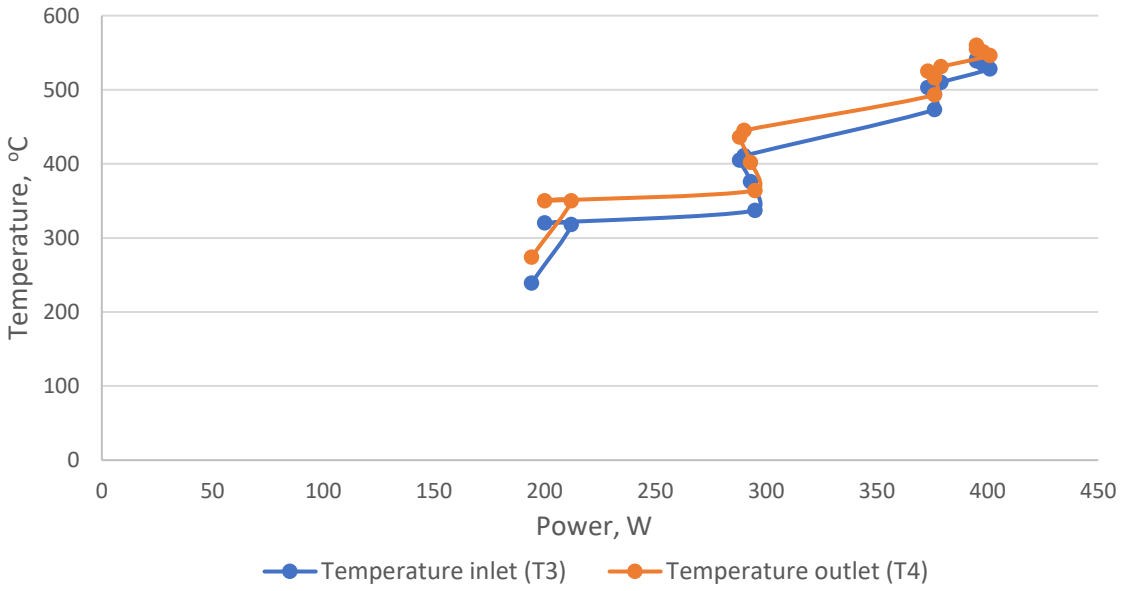

Figure 32. Power vs. temperature correlation in 20 PPI SiSiC sponge tests

These tests conclusively demonstrated the feasibility of using the DRH concept to achieve the required temperatures in a controlled and efficient manner. It should also be noted that the design of the apparatus proved to be reliable and able to withstand high temperatures without any decrease in heating efficiency. It also confirmed that even though the resistivity of SiSiC sponges decreases with temperature [113], it does not affect the operation of the reactor.

5. TEST PROCEDURE AND RESULTS OF SODIUM VAPOR AS THE CATALYST

This section presents the results of the investigation of sodium vapor as a catalyst. It begins with evaporation and condensation trials, followed by blank experiments and catalyzed reaction tests. Each step contributes to a deeper understanding of the potential of sodium vapor as an effective catalyst.

5.1 Sodium evaporation and condensation experiments

The effectiveness of a bubble column is closely related to its design and operating parameters. This investigation aimed to identify and quantify the specific parameters that influence the performance of an argon-fed sodium bubble column. Through systematic experimentation and analysis, key variables were identified and measured, providing the basis for improved process understanding and potential scale-up. The selected flow rates, temperatures, and pressures to be tested were primarily based on the investigation described in Section 4.1, as well as on the experimental results presented in [17, 29]. The main objective was to define parameters that would enable a sodium flow ranging from approximately 0.03 g h^{-1} up to ca. 0.3 g h^{-1}. Nevertheless, it can be stated that the catalyst dosing unit operational range would permit the conduction of catalytic tests with up to 120 g h^{-1} of methanol.

In the evaporation and condensation experiments with highly pure sodium (ER Grade), the initial conditions were set to a flow rate of 1.9 l min^{-1}, an evaporation temperature of 450 °C and a pressure of 1.1 bar. Under these conditions, the sodium evaporation rate was approximately 0.065 g h^{-1}, as shown in Figure 33. Further experiments involved increasing the temperature to 500 °C and running tests at four different argon flow rates, all of which were maintained at a pressure of 1.2 bar. A noticeable trend emerged from these experiments: the evaporation rate of sodium increased as the argon flow rate increased. The results obtained at the minimum flow rate (0.8 l min^{-1}) were particularly significant. These results are crucial for direct methanol dehydrogenation tests, especially considering the goal of minimizing argon consumption on an industrial scale. At this flow rate, two experiments were run for three hours each, and a third was run for six hours. The sodium evaporation rates recorded in these tests were 0.11, 0.115 and 0.118 g h^{-1}, respectively.

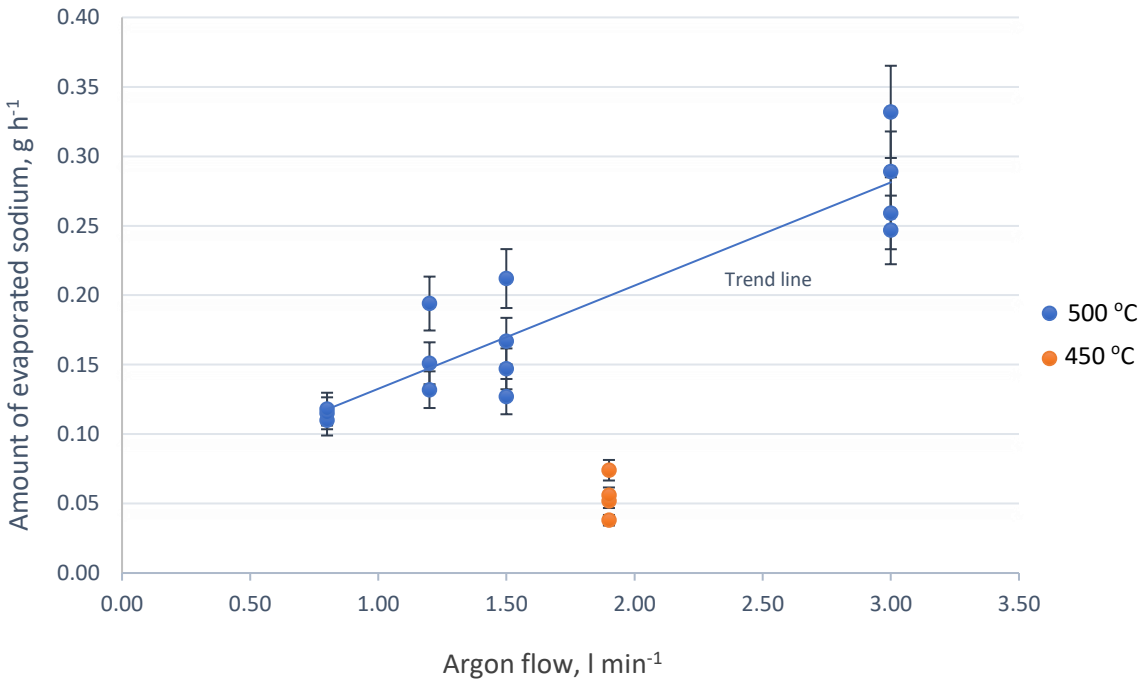

Figure 33. Experimentally determined amounts of sodium in the sodium evaporation and condensation tests (temperature of bubble column set at 500 and 450 °C)

Figure 34 presents data from the experimental trials (mean values) and the amount of sodium determined by mass balance evaluations. In this work, the observed deviation between the average experimental results at an argon flow rate of 3 l min^{-1} and the theoretical predictions (according to Eq. 30) is attributed primarily to a mixture of experimental inaccuracies and particular operating conditions. The experiments revealed a phenomenon in which a high argon flow may have caused the displacement of liquid sodium from the bubble column, an aspect not considered in the mass balance calculations. This aspect is likely to be a significant factor, contributing to the discrepancies observed in the results.

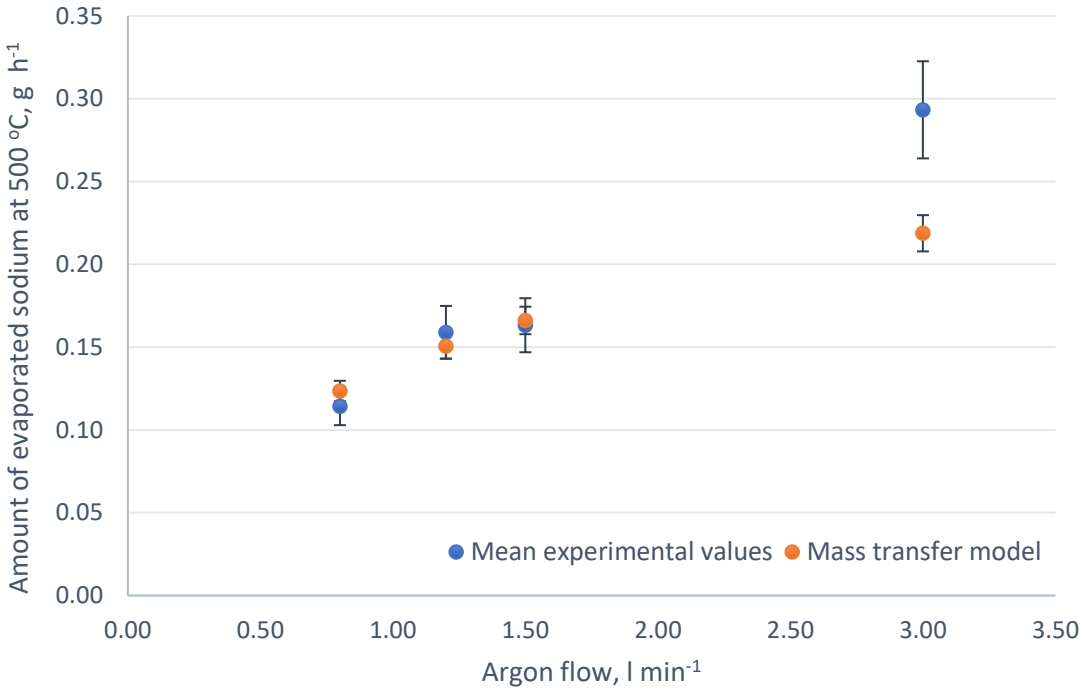

Figure 34. Comparison of experimental mean values with calculated amounts of sodium using the mass transfer model

The results of the study highlight the need for further research, particularly in larger units, to deepen the understanding of these experiments. The additional studies are essential for validating these findings and ensuring their applicability in larger, more complex systems. However, as far as the scale of the mini-plant is concerned, the constant evaporation of sodium was found to be sufficiently reliable and the catalyst dosing unit could be used in the Medena setup.

5.2 Uncatalyzed reaction

These trials were conducted to evaluate the conversion of methanol in the absence of a catalyst, thereby providing insight into the thermal decomposition behavior of methanol under specific conditions. By examining methanol conversion at various temperatures, the impact of thermal energy alone on the reaction can be determined, thus allowing for a comparison with catalyzed reactions. Experiments were carried out to determine the conversion of methanol (with a molar concentration of 10%) in the absence of a catalyst at a pressure of 1.15 bar. The total flow rate for these experiments was set at 1.2 l $min^{-1,}$ and the experiments were carried out at different temperatures: 700 °C, 750 °C, 800 °C, 850 °C and 900 °C. The results showed that the thermal decomposition of methanol starts at 700 °C. As the temperature increased,

the conversion rate of methanol also increased significantly. At 700 °C, the conversion rate was 1% and increased progressively with each temperature increase: 2% at 750 °C, 4% at 800 °C and 50% at 850 °C, reaching 98% at 900 °C. The main products of the thermal decomposition of methanol were hydrogen and carbon monoxide. Very small amounts of formaldehyde were detected. The observed conversion rate in the blank measurements can be attributed to the thermal decomposition of methanol. It is well established that methanol decomposes into formaldehyde and hydrogen when exposed to high temperatures, even in the absence of a catalyst [114]. It is also presented in the literature that the thermal decomposition starts from 700 °C, however, it also depends on specific process parameters such as residence time and pressure [31, 115, 116]. Furthermore, as outlined in Section 2.1.2, the experimental results clearly demonstrate that the thermal decomposition of methanol depends primarily on reaction kinetics rather than thermodynamic equilibrium.

5.3 Catalytic tests

After successful sodium evaporation and condensation experiments, as well as uncatalyzed reaction tests, a series of catalytic tests were carried out. The objectives of these tests were to determine the effectiveness of the concept by evaluating the conversion of methanol and the selectivity and yield of formaldehyde. Several experiments were carried out for various methanol and sodium flows and varying temperatures. The results are shown in Table 9. Without a catalyst, a conversion rate of 2% was observed at a temperature of 700 °C with a 10 mol% methanol flow. This conversion increased significantly to 95% with the introduction of the catalyst, resulting in a 68% yield of formaldehyde, as shown in Figure 35. At a higher temperature of 800 °C and with sodium as the catalyst, the methanol conversion was almost complete, with a 70% yield of formaldehyde and hydrogen as the main by-product.

Table 9. Reaction conditions and results of catalytic tests with sodium vapor

Reaction temperature, °C	MeOH flow, g h^{-1}	Argon flow, g h^{-1}	Sodium flow, g h^{-1}	MeOH conversion, %	CH_2O selectivity, %	CH_2O yield, %	Gaseous products
700	10	237	-	2	x	x	H_2, CO, HCOOH
550	10	237	0.114	50	45	22	H_2, CO, MeFo
700	10	237	0.032	95	72	68	H_2, CO, CH_2O, MeFo
800	10	237	0.012	95	63	60	H_2, CO, CH_2O, MeFo
800	10	153	0.018	99	70	70	H_2, CO, CH_2O
800	20	143	0.018	84	70	58	H_2, CO, CH_2O

However, it should be noted that as the methanol concentration in the stream increased, the yield decreased. It is therefore essential to optimize the system to use higher methanol concentrations without compromising the conversion or selectivity. Higher methanol concentrations may lead to secondary or competing reactions that negatively impact formaldehyde production. Furthermore, these side reactions may have different kinetics, potentially increasing their rates faster than the desired reaction, thus reducing selectivity. Interestingly, during the experiments sodium was found in its metallic state at the gas scrubber inlet, indicating the possibility of its partial or complete recovery. Nevertheless, the design and tests of a catalyst recovery system were beyond the scope of this work and therefore no attempts were made in this regard.

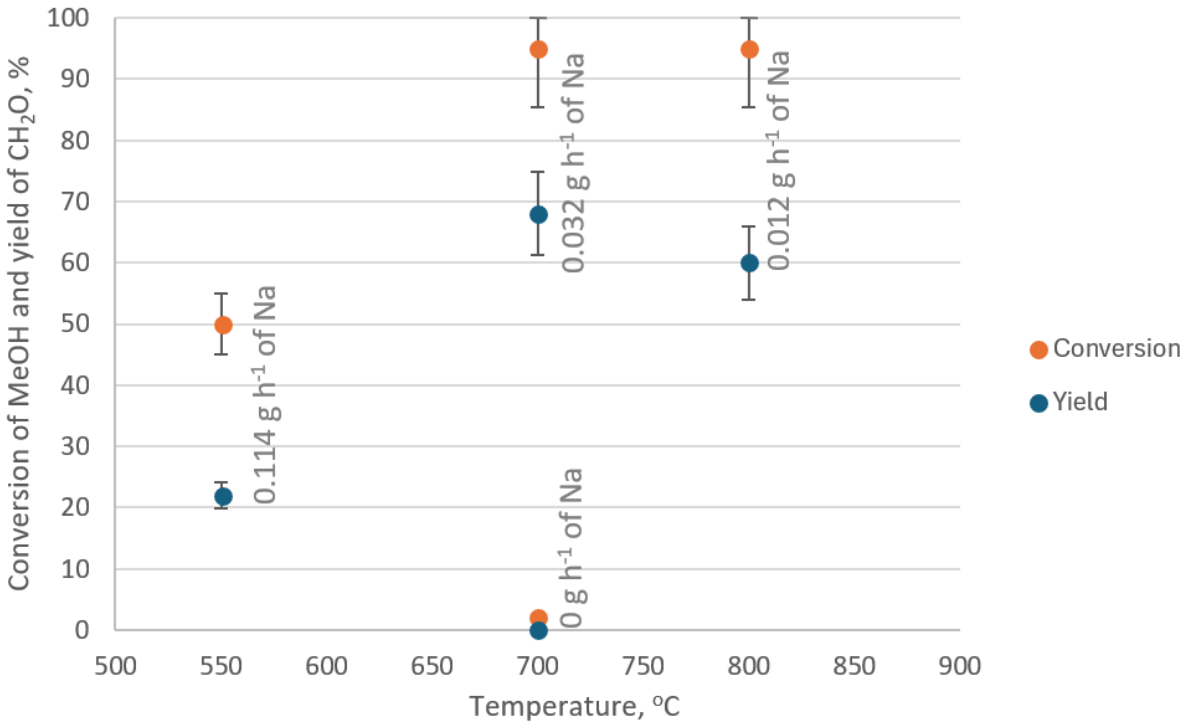

Figure 35. Experimental results showing the temperature dependence of the conversion and yield of 5 mol% MeOH

In summary, the catalytic tests successfully demonstrated that sodium vapor can be effectively used as a catalyst for the dehydrogenation of methanol to formaldehyde process. The experiments showed promising results with high methanol conversion and formaldehyde yield. In addition, almost complete conversion was achieved at higher temperatures and the possibility of catalyst recovery was revealed. This gives potential for further scale-up of the process. However, optimization of the methanol concentration is necessary to avoid reduced selectivity and competing side reactions.

Assessment of the experimental results

As discussed in the Sections 2.1.2 and 2.2, sodium compounds were tested across various experimental setups and concepts. The comparison of the selected results obtained from the tests conducted within this thesis's framework and those reported in the literature is presented in Table 10. It is important to note that the experimental results listed below were measured using different reactor concepts (except for study [13]), which makes direct comparison challenging due to variations in residence time, reactor volume, and other operational parameters. It is also relevant that in both studies [13] and [17] sodium was introduced into the reactor in the vapor phase.

Table 10. Comparison of results for sodium vapor-based catalysts

Catalyst/Conditions	Temperature, °C	X_{MeOH}, %	S_{CH2O}, %	Ref.
$Li_{0.5}Na_{0.5}AlO_2$ m_{cat} = 2.41 g, t = 24 h 10 mol% CH_3OH + N_2	900	98	74	[39]
10 mol% CH_3OH + N_2 (2.35 l min^{-1}) Na 0.15 g h^{-1}	785	95	83	[13]
10 mol% methanol + N_2 Na vapor 0.0115 g h^{-1}	827	97	80	[17]
8 mol% MeOH + Ar (1.03 l min^{-1}) + Na vapor 0.032 g h^{-1}	800	99	70	Own work

In the study of [39], in which a $Li_{0.5}Na_{0.5}AlO_2$ catalyst was used at 900°C high conversion was achieved due to the diffusion of Li+ and Na+ from the catalyst to the walls of a corundum reactor. In comparison, the approach of using sodium vapor as a catalyst at a lower temperature of 800 °C resulted in a methanol conversion of 99% and a selectivity for formaldehyde of 70%, indicating a high efficiency, although with a slight compromise in selectivity compared to the mixed oxide catalyst. It can be observed that the use of sodium vapor as a catalyst makes it possible to lower the reaction temperature and still achieve high levels of methanol conversion with regard to mixed oxide catalysts. Compared to the results reported in [13], the experiment detailed in Table 10 used approximately 4.5 times less catalyst for a comparable conversion rate, although with an impact on formaldehyde selectivity. Sodium vapor was also tested in a microstructure reactor system, in which a high selectivity of formaldehyde at ca. 825 °C was also obtained, using 0.0115 g h^{-1} sodium vapor flow [17]. Nevertheless, while microstructured reactors offer numerous advantages, the process of scaling them up to an industrial level can be complex, as maintaining the same level of mixing efficiency and residence time distribution is challenging [117].

In conclusion, the results presented in this work are in close agreement with those previously reported in the literature [13, 14, 47]. Despite the notable differences and their potential reasons discussed above, the overall consistency of the experimental results with existing studies strengthens the reliability of the procedures employed in this research. In addition, it shows that the design of the sodium dosing system was performed successfully, and can be used to further develop this approach.

6. TEST PROCEDURE AND RESULTS OF THE DIRECT RESISTANCE HEATING CONCEPT

This chapter provides a comprehensive overview of the DRH reactor concept tests. It begins with the results of uncatalyzed tests on ceramic sponges, with a focus on assessing the performance of the DRH reactor in the absence of a catalyst. Then, a description of the catalyst preparation method, particularly the materials used and the procedural steps involved, is presented, Next, the results of the catalytic tests are discussed, including both conventional and 3D printed ceramic sponges. The discussion includes an analysis of the stability tests to evaluate the performance over time. The subsequent section focuses on regeneration experiments, providing insights into the reusability and durability of the catalyst materials. Finally, the chapter concludes with an evaluation of the DRH reactor concept, comparing the performance and durability of different sponges and materials, and discussing the overall feasibility of the system.

6.1 Uncatalyzed tests conducted on ceramic sponges

In order to establish reference points for the evaluation of the thermal decomposition of methanol, uncatalyzed tests were conducted. Moreover, an additional objective was to judge the behavior of the sponges in the absence of a catalyst under the specified experimental conditions. To assess the performance of the sponges, tests on both a 20 PPI SiSiC sponge and a 20 PPI 3D-printed sponge under similar conditions without catalysts were carried out. The results are shown in Table 11. Regarding the 20 PPI SiSiC sponge, the thermal decomposition of methanol started at ca. 455 °C, and at 609 °C methanol conversion of 75% was reached. For the 3D-printed sponges, the results showed that the thermal decomposition began at 443 °C, and at 617 °C the conversion rate was 60%.

Table 11. Conditions and results of the uncatalyzed tests for a 20 PPI SiSiC conventional sponge and a 20 PPI 3-D printed SiSiC sponge

No	Sponge	MeOH, mol% Total flow, l min^{-1}	Current, A Voltage, V Power, W	Mean reaction temperature, °C	X_{MeOH}, %	Products
1	Conventional	9 1.3	I = 22.0 U = 8.8 P = 194	456	2	H_2, CO
2			I = 29.6 U = 12.2 P = 361	609	75	H_2, CO, CH_2O≤10%
3	3-D printed	10 1.4	I = 25.4 U = 9.3 P = 236	443	2	H_2, CO
4			I = 31.6 U = 10.5 P = 332	617	60	H_2, CO, CH_2O≤10%

It can be concluded that both types of sponges behave similarly under the conditions described, while the 20 PPI SiSiC sponge achieved a higher methanol conversion rate (75%) at a temperature of 609 °C compared to the 20 PPI 3D-printed sponge which achieved a conversion rate of 60% at 617 °C. The given temperature is only an indicator of the conditions in the reactor at a distance of 3 cm from the sponge, as described in Section 4.6.2. Therefore, it is also worth mentioning that the power input was slightly higher (361 W) for the SiSiC sponge, compared to 332 W for the 3D-printed sponge, which also influenced the final conversion rate. In addition, the observed performance of the two sponges may be attributed to differences in their internal structures, such as porosity, surface area and pore size distribution. Overall, the experiments indicated that ceramic sponges, in general, are promising as heat carriers in the proposed reactor model for dehydrogenation of methanol.

6.2 Catalyst preparation method

Impregnation is a widely used method for catalyst preparation, in which an active material is deposited on a porous support to enhance catalytic performance [118,119]. Therefore, this method was chosen to apply Na_2CO_3 to ceramic sponges for subsequent catalytic testing. Based on the results presented in 4.6, the 20 and 30 PPI

sponges were selected for impregnation due to their resistivity and potential power output.

Before impregnation, the sponges were carefully washed in an ultrasonic bath for three hours. Both 20 PPI and 30 PPI standard sponges were impregnated with a 3 mol of Na_2CO_3 solution (500 ml) and with 25 ml of ethylene glycol (to increase the viscosity of the solution and enhance the dispersion of the active component). Following each impregnation cycle, five in total, the sponges were dried at 250 °C for 45 minutes. The fully impregnated sponge (20 PPI) did not conduct electricity because Na_2CO_3 acts as an insulator. The active material on the outer surface of the sponge was dissolved, resulting in a sponge mass of 10.182 g after partial removal of the washcoat and subsequent drying at 250 °C for two hours. This process made the sponge suitable for further testing (Figure 36), and the masses of the active material on the sponge are listed in Table 12.

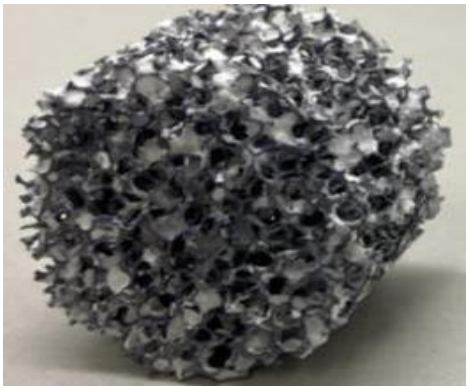

Figure 36. Impregnated SiSiC sponge, photograph: M. Kamienowska-Orsini

The 3D-printed sponge was also impregnated with 3 mol of Na_2CO_3 solution (500 ml) and a small amount of ethylene glycol (25 ml). The sponge was dried at 250 °C for 45 minutes after each series of impregnations (10 times in total). Partial removal of the washcoat was not necessary for the 3D-printed sponge. An electric current was passed through the sponge (Figure 37).

Figure 37. 3D-printed impregnated sponge, photograph: M. Kamienowska-Orsini

Table 12 presents the masses of the sponges before and after impregnation. The conventional 20 PPI sponge and the 3D-printed sponge were selected for the catalytic tests based on the impregnation results, as they exhibited the largest amount of material deposited. For the 30 PPI sponge, however, this amount may prove insufficient for the experiments in the DRH reactor, and thus it was not further examined. Furthermore, it is important to acknowledge that the insertion of the sponge into the reactor may result in minor weight loss.

Table 12. Summary of the masses of the sponges before and after the impregnation processes

Type of sponge	Conventional	3D-printed	Conventional
PPI	20	20	30
Sponge mass, g	9.56	40.92	11.14
Sponge mass after impregnation, g	11.90	44.05	12.53
Difference in mass, g	2.35	3.13	1.42
Sponge mass after partial removal of the washcoat, g	10.182	-	-
Difference in mass, g	0.625	-	-

In conclusion, the sponges were successfully impregnated and prepared for further testing. Confirmation of the effectiveness of this procedure is provided in Section 6.6, in which the analysis of the deposited material before and after impregnation, as well as post-testing, is presented.

6.3 Catalytic tests

The experimental tests were carried out to prove that the DRH concept can be used for the dehydrogenation of methanol to anhydrous formaldehyde and for hydrogen production. The main objectives of these experiments were to determine the durability of the reactor elements in the presence of methanol and sodium carbonate and to find the optimum values of the applied electric current required to perform the endothermic reaction. Furthermore, several different mass flows of methanol and its content in the stream were tested. One of the objectives was to achieve high methanol conversion with sufficient selectivity towards formaldehyde. As already mentioned in Section 2.1.2, formaldehyde is unstable and tends to decompose, therefore various gas velocity rates were investigated to minimize this process. Catalytic tests were carried out using both 20 PPI conventionally manufactured and 20 PPI 3D-printed impregnated ceramic sponges to facilitate comparison and a comprehensive analysis of their performance. Detailed experimental findings are described in the following.

The conventional sponge impregnated with Na_2CO_3 was tested in the DRH reactor. The selected results are presented in Table 13.

Table 13. Results of impregnated standard sponges in DRH setup

No.	Amount of Na_2CO_3 on the sponge, g	MeOH, Mol % Total flow l min^{-1}	Current, A Voltage, V Power, W	Mean reaction temperature, °C	X_{MeOH}, %	S_{CH2O}, %	Y_{CH2O}, %
1	0.6	15 0.95	I = 25 U = 9.2 P = 230	478	85	40	38
2	0.3	10 1.4	I = 27 U = 8.8 P = 238	525	80	56	46
3		15 0.95	I= 27 U = 8.8 P = 238	515	70	49	34
4		10 2.1	I = 30 U = 8.8 P = 264	523	52	58	30

Firstly, it is evident that with a power input of 238 W, an 80% methanol conversion was achieved, whereas under similar flow conditions during the uncatalyzed tests, 75%

conversion was reached at 361 W (Section 6.1). This clearly demonstrates that when the sponge is impregnated with sodium carbonate, the activation energy of the reaction decreases significantly, and formaldehyde production is enhanced. Furthermore, an increased mass flow rate and methanol content in the stream require a higher temperature to achieve comparable conversion. However, as shown in Experiment no. 4, as the gas velocities increased, the selectivity of formaldehyde improved, but a moderate conversion of MeOH was obtained. This phenomenon might also be indicative of a partial deactivation of the catalyst. Nevertheless, the optimization of the catalyst amount as well as flow rates is necessary in order to maintain high formaldehyde yield. In addition, traces of CO_2, CH_4, HCOOH and $HCOOCH_3$ were detected in most of the experiments. Presumably, water was also produced but the analytical equipment was unable to detect it. After the experiments, some carbon deposits were found on the sponge. In conclusion, the results of the tests demonstrated that the dehydrogenation reaction is indeed occurring on the impregnated conventional sponge in the DRH reactor.

The 3D printed sponge impregnated with 3.1 g of Na_2CO_3 was also subjected to catalytic tests in the DRH reactor. The selected results are presented in Table 14.

Table 14. Results of impregnated 3D-printed sponge for the DRH setup

No.	MeOH, Mol % Total flow, l min^{-1}	Current, A Voltage, V Power, W	Mean reaction temperature, °C	X_{MeOH}, %	S_{CH2O}, %	Y_{CH2O}, %
1	8.5 1.7	I = 29.9 U = 8.2 P = 245	617	99	53	53
2	10 1.4	I = 29.6 U = 8.3 P = 246	539	77	57	44
3	5 2.3	I= 30.1 U = 7.8 P = 235	525	91	58	53
4	10 2.3	I = 31.6 U = 8.3 P = 262	591 627	92 95	60 45	55 44

It is clearly demonstrated that with a power input of 246 W, a 77% methanol conversion was reached in contrast to uncatalyzed tests under identical flow conditions, in which 60% of methanol was converted at 332 W (Section 6.1). This

highlights the effectiveness of the impregnated 3D printed sponge in achieving high conversion and selectivity rates. Furthermore, as evidenced in experiments 2 and 4, increasing the gas velocity resulted in a slight improvement in methanol conversion, up to 92%, and formaldehyde selectivity, up to 60%. However, an increase in temperature led to a decrease in selectivity to 45%, while the conversion rate increased to 95%. It can be concluded that higher gas velocities positively influence formaldehyde production, although the conversion rate may be affected as a consequence. Traces of CO_2, CH_4, HCOOH and $HCOOCH_3$ were also found in most of the experiments, as in the case of the standard sponge. Some carbon deposits were also present on the sponge after the trials. Nevertheless, these results suggest that optimizing the flow conditions and power input can further improve selectivity and conversion, offering potential pathways for enhanced process efficiency.

The 3D-printed impregnated sponge (2.5 g of Na_2CO_3) was also subjected to catalytic tests which investigated higher concentration of methanol flows. The selected results are presented in Table 15.

Table 15. Results of 3D-printed impregnated sponge for the DRH setup during high concentrations methanol trials

No.	MeOH, mol % Total flow, l min^{-1}	Power, W	Mean reaction temperature, °C	X_{MeOH}, %	S_{CH2O}, %	Y_{CH2O}, %
1	30 1.2	310	606	84	35	28
2	40 0.9		610	76	34	25
3	50 0.7		610	72	30	22

The findings suggest that a higher temperature/power input is required to thoroughly examine the reaction with increased methanol flow rates. It is important to note that the primary products observed were hydrogen and carbon monoxide. Furthermore, modifications to the sponge's geometry, potentially including an elongated structure, and an increase in the electric current may facilitate selectivity towards formaldehyde production. Nevertheless, further in-depth experimental and theoretical investigations

are required to gain a more comprehensive understanding of this topic and to identify potential optimization opportunities for the sponge and reactor geometry.

Based on the experiments conducted, specific features were identified for both the 3D-printed ceramic sponge and that produced by a replication method. These characteristics are presented in Table 16. A comparison of the standard sponge and 3D-printed one showed that while both types of sponges have similar levels of potential to achieve good catalytic results, the 3D-printed one has significant advantages that render it a more viable option for future applications. A key feature of the 3D-printed sponge is the integration of a solid layer around it. As a result, the nickel plates remain undamaged throughout the testing process, even when exposed to high temperatures. This durability is a significant improvement over that of standard sponges. Furthermore, a pressure drop analysis for the DRH setup is discussed in the Appendix (Section 9.3), addressing key factors affecting fluid flow within the reactor.

Table 16. Comparison of standard and 3D-printed ceramic sponges

Conventional SiSiC	3D-printed SiSiC
Higher electrical resistance	Lower electrical resistance
Catalyst loading ca. 1 g	Catalyst loading ca. 3 g
Not suitable for nickel plates	Suitable for nickel plates
Lower pressure drop	Higher pressure drop

In conclusion, the 3D-printed sponge was selected as the primary object of interest for further investigation due to its ability to accommodate higher catalyst loadings and its compatibility with the reactor design incorporating nickel plates.

6.4 Stability tests

Stability assessment is crucial for evaluating the durability and functional lifespan of the proposed catalyst body concept. The chemical stability of the impregnated 3D-printed sponge was tested over time in a series of experiments. The sponge was exposed to the reaction temperature for more than 30 hours, during which seven different sets of experiments were performed. Throughout these tests, the assembly,

including the catalyst, demonstrated consistent stability for at least 2.5 hours (Table 17).

Table 17. Stability test results for the DRH setup

No.	MeOH, mol % Total flow, l min^{-1}	Power, W	Mean reaction temperature, °C	X_{MeOH}, %	S_{CH2O}, %	Y_{CH2O}, %	Time, h
1	8.5 1.7	P = 240	560	87	54	47	3
2		P = 242	566	95	54	51	3
3		P = 245	571	99	53	53	2.5
4	5.0 2.3	P = 235	567	88	58	51	4
5		P = 235	570	91	58	53	4

These results indicate the sponge's potential for applications requiring high chemical stability and temperature resistance. Formaldehyde yield remained stable over the course of the tests. Moreover, these findings are in line with previous tests which showed that the higher the temperature, the higher the conversion. It is important to note that even a small difference power input and average reaction temperature leads to a varying conversion (3 and 5). It was expected that a lower methanol content in the stream would result in greater methanol conversion at lower temperatures (as described in Section 2.1.2). This could indicate that catalyst deactivation may have influenced the results in the experiments (4 and 5), indicating a potential area for further investigation and optimization. For this reason, regeneration tests were carried out on the catalyst body and are described in the following section.

6.5 Regeneration of the catalyst

Regeneration experiments of the catalyst body were carried out by using a mixture of 2.5 vol% oxygen in argon. The process involved heating the reactor from 200 °C to 450 °C for a 2.5-hour period, followed by maintaining the temperature at 500 °C for a further hour. The total regeneration time was 3.5 hours and was stopped only when trace amounts of CO_2 and CO were present in the gas stream. Although the post-regeneration catalytic tests were successful, a notable decrease in selectivity and yield

was observed (Table 18). One of the possible reasons for this decline may be changes in the catalyst structure before the regeneration attempt, potentially limiting the active material available for effective catalytic performance in subsequent tests. Additional detailed investigation is necessary to better understand the influence of the regeneration process on possible changes in the catalyst's structure and its impact on its activity. Nevertheless, these trials confirmed the feasibility of regeneration of the catalyst by means of oxygen gas without affecting the reactor components.

Table 18. Regeneration test results for the DRH setup

No.	Power, W	Mean reaction temperature, °C	Products	X_{MeOH}, %	S_{CH2O}, %	Y_{CH2O}, %
Before regeneration	P = 235	570	H_2, CO, CH_2O	91	58	53
After regeneration	P = 284	587	H_2, CO, CH_2O	86	42	36

6.6 Catalyst analysis

The basic criteria for all effective catalysts are high selectivity, stability and activity [120]. Therefore, the fresh (after impregnation) and spent catalysts used for the stability tests, after regeneration and further tests (sections 6.1 and 6.5) were analyzed by the X-ray photoelectron spectroscopy[2] (XPS) in order to gain insight into the characteristics of Na_2CO_3 as a catalyst in the DRH concept. XPS measurements were performed using a K-Alpha+ XPS spectrometer (ThermoFisher Scientific). The Thermo Avantage software was used for data acquisition and processing. All samples were analyzed using a microfocused, monochromated Al Kα X-ray source (400 µm spot size). The K-Alpha+ charge compensation system was employed during analysis, using electrons of 8 eV energy, and low-energy argon ions to prevent any localized charge build-up. The spectra were fitted with one or more Voigt profiles (BE uncertainty: ±0.2 eV) and Scofield sensitivity factors were applied for quantification [121]. All spectra were referenced to the C 1s peak (C-C, C-H) at 285.0 eV binding

[2] The presentation of the XPS results was possible on account of the courtesy of the Surface and Interface Analysis team at KIT, with special thanks to Vanessa Trouillet.

energy controlled by means of the well-known photoelectron peaks of metallic Cu, Ag, and Au, respectively.

Figure 38 illustrates XPS spectra comparing the O 1s signals of Na_2CO_3 in three different states: as a commercial powder reference, in a fresh catalyst and in the catalyst after the reaction. Figure 39 provides XPS spectra evaluating C 1s. The peaks shown correspond to the binding energies of the photoelectrons detected, which are characteristic of different oxygen-containing functional groups, as well as for carbon-carbon and carbon-hydrogen species. Some key highlights can be reported from these spectra:

- The Na_2CO_3 reference shows the carbonate peak in O 1s at 531.3 eV [122], stoichiometrically corresponding to the C 1s at 289.6 eV, as well as the Na 1s peak at 1071.2 eV (not shown here) attributed to Na_2CO_3. The CO_3^{2-} peak at 531.3 eV, associated with carbonate ions, is present both in the fresh catalyst and in the catalyst after the reaction, accompanied by the Si-O species.
- The peak at around 532.7 eV, corresponding to oxygen in a silicon-oxygen (Si-O) bond [123], is only seen in the fresh and spent catalysts due to impurities from the ceramic sponge. The corresponding SiO_2 can also be observed in Si 2p3/2 at 103.1 eV (not shown here).
- Besides Na 1s, the presence of sodium in the samples can also be followed by the appearance of the Na KLL Auger line of sodium at around 536 eV [124].
- A carbon black peak (sp2) is present in C 1s at 283.4 eV [125], indicating that some reduced carbon species were formed on the spent catalyst, which had an influence on the activity of the catalyst. It should be noted that these species are more conductive than the other carbon species present and appear with a very low binding energy (-1 eV) after the necessary referencing to (C-C, C-H) for the whole sample. However, this is a known effect observed when both conductive and non-conductive species are present in a sample.

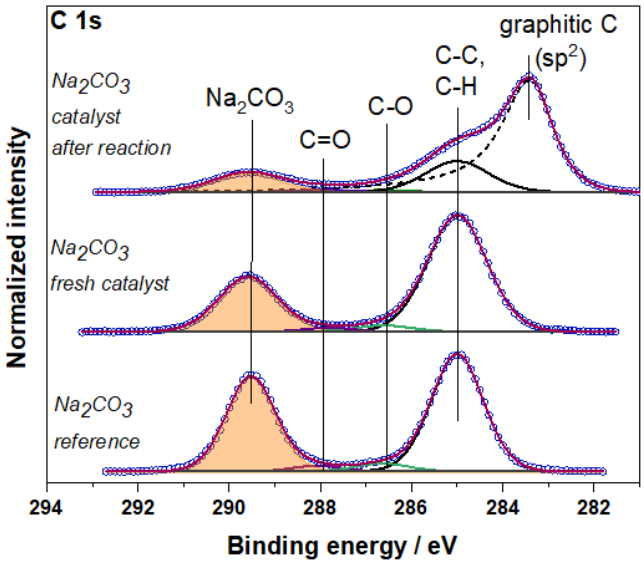

Figure 38. XPS results for fresh and spent catalyst – C 1s, author: V. Trouillet

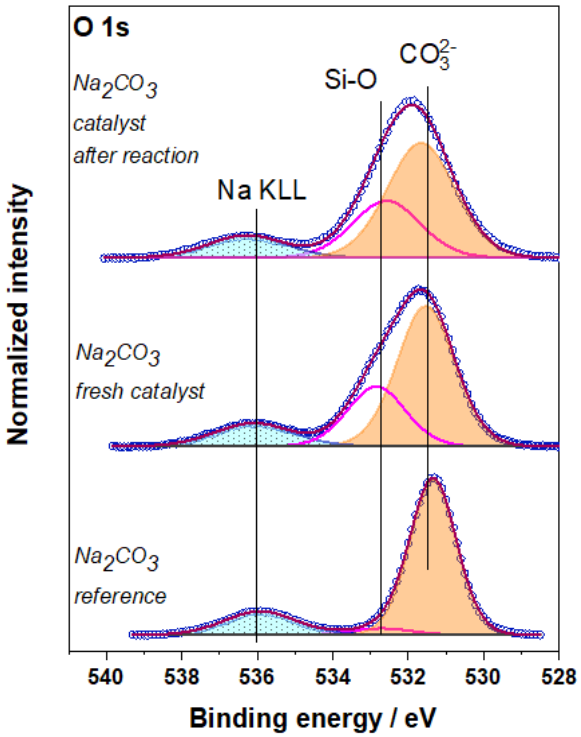

Figure 39. XPS results for fresh and spent catalyst – O 1s, author: V. Trouillet

In summary, it can be concluded that the impregnation process was successful, as evidenced by the minimal differences observed between the XPS results of the Na_2CO_3 reference and the fresh catalyst, indicating that the catalyst's chemical integrity was largely preserved after the impregnation process. The analysis of the spent catalyst shows that there are the changes in its structure and further investigation is required to elucidate the extent to which the regeneration process

affects the active material. In addition, the formation of carbon deposits on the spent catalyst, as evidenced by both XPS analysis and visual inspection, is a clear indicator of the reduction in catalytic performance. This is consistent with the coking phenomenon, which can block active sites and hinder the catalyst's functionality (Section 2.4). To maintain long-term catalytic efficiency, emphasis should be placed on catalyst regeneration and strategies to minimize carbon deposition.

6.7 Assessment of the direct resistance heating reactor

As demonstrated in the experimental trials, the DRH reactor was successfully designed for the simultaneous production of anhydrous formaldehyde and hydrogen gas. The reactor can incorporate both 3D-printed and conventional sponges impregnated with sodium carbonate, which serve the dual purpose of functioning as catalysts and heating elements. A significant feature of this design is the reactor's capacity to withstand the elevated temperatures required for the endothermic dehydrogenation of methanol, while ensuring the structural integrity of its components over extended operational periods. The combination of thermal management and catalyst efficiency constitutes the basis of the reactor's advanced performance.

The photographs in Figure 40 and Figure 41 show the condition of the DRH elements after approximately 30 hours of experimental use. The parts were found to be largely intact. This suggests that these components withstood the experimental conditions well and were in a satisfactory condition for further testing. The resistance of the nickel plate to methanol corrosion and its engineering design, in particular, its thin profile and precise welding of the nickel wire, are key factors in this concept.

Figure 40. 3D-printed sponge after the experiments, photograph: M. Kamienowska-Orsini

Figure 41. Macro insulation with nickel plates and wires connected to the copper adapter after the experiments, photo: M. Kamienowska-Orsini

The demonstrated durability of the system indicates the applicability of the DRH approach for the production of anhydrous formaldehyde in parallel with the co-generation of hydrogen gas in the mini-plant scale. Adequate temperatures to allow the endothermic reaction were achieved, up to 665 °C for the conventional sponge and 650 °C for its 3D-printed equivalent. It is apparent that the DRH concept brings a new perspective to this sort of catalyst and is a promising concept that needs to be further developed. Table 19 shows the results reported in the literature and some selected findings presented in this thesis.

Table 19. Comparison of results for sodium carbonate-based catalysts

Catalyst	Temperature, °C	X_{MeOH}, %	S_{CH2O}, %	Ref.
Na_2CO_3 10% MeOH + N_2	700	56	65	[14]
Na_2CO_3 + In_2O_3 (1 mol %) 10% MeOH + N_2	650	60	75	[14]
Na_2CO_3 + 20%C 4.7% CH_3OH (0.2 l min^{-1}) m_{cat} = 0.1g	690	72	70	[15]
Na_2CO_3 (sponge) – DRH 10 mol% MeOH, 12 g h^{-1}	511*	80	56	Own work
Na_2CO_3 (3D sponge) – DRH 5 mol% MeOH, 10 g h^{-1}	575*	91	58	Own work

Compared to the results given in the literature [14, 15] which are also described in Section 2.1.2, the use of a sponge as both a catalyst support and heating medium significantly increased the methanol conversion rates, while maintaining satisfactory levels of selectivity. Yet, there is still chance for improvement in the modification of the

catalyst to increase the selectivity towards formaldehyde. For example, by adding additional active substances to the catalyst or by modifying the design of the reactor to minimize the decomposition of formaldehyde. Such modifications may also include optimizing the surface area of the sponge to facilitate catalyst distribution or altering the flow dynamics within the reactor to reduce the exposure time of formaldehyde to conditions that promote its decomposition. To conclude, when compared to traditional fixed-bed experimental setups, the DRH system appears to offer significant advantages, particularly in terms of thermal efficiency and its potential to contribute to the electrification of the chemical industry which aims to reduce reliance on fossil fuels and thus achieve lower carbon emissions. The DRH approach allows for more precise control of temperature distribution within the reactor, leading to improved heat transfer and reduced energy losses. This increased heat efficiency not only enhances reaction rates but also minimizes the overall energy consumption of the process. The heat demand analysis for the DRH setup is provided in the Appendix (Section 9.2), offering insights into the thermal requirements of the system.

In addition, while contrasting the sodium vapor (selected results are shown in Table 10, see page 88) and sodium carbonate catalysts, the notable differences can be observed in reaction temperatures, methanol conversion rates, and selectivity towards CH_2O production. When operated in the temperature range of 800 to 900°C, sodium dosed in its vaporized form demonstrates higher methanol conversion rates, typically between 95% and 99%. Additionally, it shows greater selectivity for CH_2O production, which ranges from 70% to 83%. A direct comparison of sodium vapor and sodium carbonate catalysts is challenging due to many factors e.g. different effectiveness of cooling system, residence times etc.

In conclusion, the DRH reactor with sodium carbonate as a catalyst and the system utilizing sodium vapor dosed via a bubble column concept revealed some differences in performance parameters. Nevertheless, each system has its own specific strengths and limitations. Sodium vapor system exhibits higher catalytic activity, but issues such as corrosion, stability of the evaporation process and industrial feasibility need to be addressed. Conversely, the DRH system is characterized by efficient heat management, ensuring better thermal control throughout the process, but faces challenges in terms of catalyst stability and reactor design. Both approaches show

significant potential, but further research and optimization are required to enable successful scale-up for pilot plant implementation.

7. SUMMARY AND OUTLOOK

7.1 Summary

Formaldehyde is used extensively in various industrial applications. Consequently, there is a demand for production methods that provide a balance between efficiency and environmental sustainability. This thesis investigates the gas phase dehydrogenation of methanol to formaldehyde and hydrogen, with a particular focus on sodium-based catalysts. The objective of this work was to demonstrate the feasibility of this process on a mini-plant scale, extending previous investigations conducted on a laboratory scale. Therefore, the MEDENA mini-plant was designed and constructed, and two core concepts were tested: continuous sodium vapor dosing by means of a bubble column and the implementation of a direct resistance heating (DRH) reactor with the incorporation of a 3D-printed SiSiC sponge impregnated with Na_2CO_3. This particular approach for the formaldehyde production process has been proposed and experimentally validated for the first time in this work.

Firstly, the findings derived from the sodium evaporation and condensation setup, as well as the catalytic tests with sodium vapor as the catalyst, showed that this concept enabled almost complete methanol conversion at 800 °C, with a formaldehyde yield of 70% and hydrogen as the main by-product. The results were consistent with the established literature and confirmed observations from related studies in which sodium metal catalysts were applied. The research also draws attention to the design of the catalyst dosing unit, as its operation is critical to the performance of the mini-plant.

Secondly, the results presented in this dissertation demonstrated that the utilization of the DRH concept combined with the impregnation of the ceramic sponge with sodium carbonate is a promising method to obtain high yields of formaldehyde and hydrogen. The use of Na_2CO_3 as a catalyst at 480 °C resulted in 30% methanol conversion, compared with only 10% without a catalyst. At approximately 600 °C, methanol conversion with the catalyst increased to over 85%, compared to around 60% in the absence of a catalyst. Moreover, the DRH system demonstrated a 92% methanol conversion and 60% selectivity towards formaldehyde under operating conditions of 31.6 A, 8.3 V and 262 W. To conclude, the concept of a directly heated, impregnated ceramic sponge showed significant potential as an innovative solution to meet the

growing demand for electrification in the chemical industry, providing a promising pathway for enhanced process efficiency and more sustainable chemical production.

In summary, this thesis presents the experimental demonstration of the production of anhydrous formaldehyde. The findings encourage further investigation of sodium-based catalysts for the dehydrogenation of methanol to formaldehyde and valuable hydrogen gas.

7.2 Outlook

The outcomes presented herein have led to the identification of both experimental and theoretical research questions, along with the corresponding future work. In particular, the following issues need to be addressed:

- Development of analytical techniques and appropriate experimental setups for comprehensive studies of the reaction mechanisms associated with the use of sodium vapor as the catalyst.
- A scale-up of a sodium bubble column system. Further extensive experimental tests, with a particular focus on the temperature distribution, should be conducted. Next, a pilot-scale demonstration is important to ensure that the system's purity can be maintained and that constant evaporation is possible. Future studies involving varying methanol and sodium vapor concentrations are required to optimize the catalytic process.
- Research into the behavior of the catalyst in the case of the DRH concept and its modification, for example, via doping with activated carbon or other metals such as Fe or Ni.
- A scale-up of a DRH reactor concept. Future work should focus on addressing technical limitations (maximum size and required power input). The primary objective shall be to ensure high selectivity toward formaldehyde when using a highly concentrated methanol stream, which is an essential criterion for the practical application of this technology on an industrial scale.

8. BIBLIOGRAPHY

[1] Global Formaldehyde Industry. ReportLinker. Available at: https://www.reportlinker.com/p05817774/Global-Formaldehyde-Industry.html. Accessed October 21, 2023.

[2] Transport and mobility. Available at: https://www.eea.europa.eu/en/topics/in-depth/transport-and-mobility. Accessed October 21, 2023.

[3] NAMOSYN. Available at: http://namosyn.de/. Accessed October 21, 2023.

[4] D.S. Mallapragada, Y. Dvorkin, M.A. Modestino, D.V. Esposito, W.A. Smith, B.-M. Hodge, M.P. Harold, V.M. Donnelly, A. Nuz, C. Bloomquist, K. Baker, L.C. Grabow, Y. Yan, N.N. Rajput, R.L. Hartman, E.J. Biddinger, E.S. Aydil, A.D. Taylor, Decarbonization of the chemical industry through electrification: Barriers and opportunities, Joule 7(1) (2023) 23–41. 10.1016/j.joule.2022.12.008.

[5] K.M. Van Geem, B.M. Weckhuysen, Toward an e-chemistree: Materials for electrification of the chemical industry, MRS Bulletin 46(12) (2021) 1187–96. 10.1557/s43577-021-00247-5.

[6] F. deLlano-Paz, A. Calvo-Silvosa, S. Iglesias Antelo, I. Soares, The European low-carbon mix for 2030: The role of renewable energy sources in an environmentally and socially efficient approach, Renewable and Sustainable Energy Reviews 48 (2015) 49–61. 10.1016/j.rser.2015.03.032.

[7] H.-J. Li, A.C. Lausche, A.A. Peterson, H.A. Hansen, F. Studt, T. Bligaard, Using microkinetic analysis to search for novel anhydrous formaldehyde production catalysts, Surface Science 641 (2015) 105–11. 10.1016/j.susc.2015.04.028.

[8] M. Deitermann, Z. Huang, S. Lechler, M. Merko, M. Muhler, Non-Classical Conversion of Methanol to Formaldehyde, Chemie Ingenieur Technik 94(11) (2022) 1573–90. 10.1002/cite.202200083.

[9] J. Sauer, G. Emig, The catalyzed dehydrogenation of methanol to formaldehyde at high temperatures: New insights by modelling of transport phenomena and reaction, Chemical Engineering & Technology 18(4) (1995) 284–91. 10.1002/ceat.270180410.

[10] N.Y. Usachev, I. Krukovsky, S.A. Kanaev, The nonoxidative methanol dehydrogenation to formaldehyde: (A review), Petroleum Chemistry 44 (2004) 379–94.

[11] P. Zaza, A. De la Torre, A. Renken, Direct dehydrogenation of methanol to formaldehyde in a circulating fluidized bed, Chemie Ingenieur Technik (1991). 10.1002/cite.330630624.

[12] A.G. Chowdhury, U. Arnold, K. Garbev, M. Bender, J. Sauer, Direct dehydrogenation of methanol to formaldehyde over ZnO–SiO2-based catalysts, Catal. Sci. Technol. 14(17) (2024) 4958–67. 10.1039/D4CY00541D.

[13] S. Ruf, A. May, G. Emig, Anhydrous formaldehyde by sodium catalysis, Applied Catalysis A: General 213 (2001) 203–15. 10.1016/S0926-860X(00)00904-2.

[14] A. Meyer, A. Renken, Sodium compounds as catalysts for methanol dehydrogenation to water-free formaldehyde, Chemical Engineering & Technology 13(1) (1990) 145–9. 10.1002/ceat.270130120.

[15] S. Su, M.R. Prairie, A. Renken, Promoting effect of active carbons on methanol dehydrogenation on sodium carbonate: hydrogen spillover, Applied Catalysis A: General 95(1) (1993) 131–42. 10.1016/0926-860X(93)80202-2.

[16] S. Su, M.R. Prairie, A. Renken, Reaction mechanism of methanol dehydrogenation on a sodium carbonate catalyst, Applied Catalysis A: General 91(2) (1992) 131–42. 10.1016/0926-860X(92)85072-J.

[17] R. Maurer, A. Renken, Dehydrogenation of Methanol to Anhydrous Formaldehyde in a Microstructured Reactor System, Chemical Engineering Research and Design 81(7) (2003) 730–4. 10.1205/026387603322302896.

[18] A.W. Franz, H. Kronemayer, D. Pfeiffer, R.D. Pilz, G. Reuss, W. Disteldorf, A.O. Gamer, A. Hilt, Formaldehyde, Ullmann's Encyclopedia of Industrial Chemistry, John Wiley & Sons, Ltd, 2016, pp. 1–34.

[19] H.I. Mahdi, N.N. Ramlee, D.H. da S. Santos, D.A. Giannakoudakis, L.H. de Oliveira, R. Selvasembian, N.I.W. Azelee, A. Bazargan, L. Meili, Formaldehyde production using methanol and heterogeneous solid catalysts: A comprehensive review, Molecular Catalysis 537 (2023) 112944. 10.1016/j.mcat.2023.112944.

[20] G.J. Millar, M. Collins, Industrial Production of Formaldehyde Using Polycrystalline Silver Catalyst, Ind. Eng. Chem. Res. 56(33) (2017) 9247–65. 10.1021/acs.iecr.7b02388.

[21] H. Sperber, Herstellung von Formaldehyd aus Methanol in der BASF, Chemie Ingenieur Technik 41(17) (1969) 962–6. 10.1002/cite.330411705.

[22] M. Qian, M.A. Liauw, G. Emig, Formaldehyde synthesis from methanol over silver catalysts, Applied Catalysis A: General 238(2) (2003) 211–22. 10.1016/S0926-860X(02)00340-X.

[23] D. Mertens, Determination of the flow properties in the reactors used in the process of direct dehydrogenation of methanol to formaldehyde. Bachelor Thesis, KIT, 2022.

[24] H. Topsoe, Å. Trulsson, H. Karlsson, By-Products from production of Formaldehyde, 2015.

[25] J. Thrane, U.V. Mentzel, M. Thorhauge, M. Høj, A.D. Jensen, A Review and Experimental Revisit of Alternative Catalysts for Selective Oxidation of Methanol to Formaldehyde, Catalysts 11(11) (2021) 1329. 10.3390/catal11111329.

[26] A.M. Bahmanpour, A. Hoadley, A. Tanksale, Critical review and exergy analysis of formaldehyde production processes, Reviews in Chemical Engineering 30(6) (2014) 583–604. 10.1515/revce-2014-0022.

[27] M. Rellán-Piñeiro, N. López, The Active Molybdenum Oxide Phase in the Methanol Oxidation to Formaldehyde (Formox Process): A DFT Study, ChemSusChem 8(13) (2015) 2231–9. 10.1002/cssc.201500315.

[28] C.J. Sebastian, F.N. Adhyaksa, M.T. Kamal, V.E. Susanto, Optimization of Energy Consumption in Formaldehyde Production Process Using Reboiled Absorption Process, J. Chem. Eng. Res. Prog. 1(1) (2024) 11–23. 10.9767/jcerp.20094.

[29] S. Ruf, Die Natrium-katalysierte Dehydrierung von Methanol zu wasserfreiem Formaldehyd. Der Technischen Fakultät der Universität Erlangen-Nürnberg, Erlangen, 1998.

[30] S. Su, P. Zaza, A. Renken, Catalytic dehydrogenation of methanol to water-free formaldehyde, Chemical Engineering & Technology 17(1) (1994) 34–40. 10.1002/ceat.270170106.

[31] J. Sauer, Methanol-Dehydrierung zu Formaldehyd im Wandreaktor. Available at: https://publikationen.bibliothek.kit.edu/18494. Accessed November 5, 2023.

[32] H. Imai, T. Tagawa, K. Nakamura, Dehydrogenation of methanol to formaldehyde over titanium alloys, React Kinet Catal Lett 43(2) (1991) 355–9. 10.1007/BF02064697.

[33] P.J. Oliver, S.C. Earle, Preparation of concentrated formaldehyde. US3321527A, 1967.

[34] F. Notheisz, A.G. Zsigmond, M. Bartók, The static microreactor technique a new, simple method for determination of kinetic parameters of gas-phase heterogeneous catalytic reactions, Reaction Kinetics and Catalysis Letters 6(4) (1977) 481–7. 10.1007/BF02078732.

[35] G.-M. Schwab, A.M. Watson, A comparison of the flow and pulse technique for the dehydrogenation of methanol, Journal of Catalysis 4(5) (1965) 570–6. 10.1016/0021-9517(65)90161-2.

[36] A. Meyer, A. Renken, New catalysts for the dehydrogenation of methanol to water-free formaldehyde, Proceedings 9th International Congress on Catalysis 4 (1988) 1898–905.

[37] H. Imai, K. Nakamura, Kinetic study of formaldehyde formation in methanol dehydrogenation over FeTiZn alloy, React Kinet Catal Lett 49(2) (1993) 305–10. 10.1007/BF02067696.

[38] A. Music, J. Batista, J. Levec, Gas-phase catalytic dehydrogenation of methanol to formaldehyde over ZnO/SiO2 based catalysts, zeolites, and phosphates, Applied Catalysis A: General 165(1) (1997) 115–31. 10.1016/S0926-860X(97)00195-6.

[39] G. Wiesgickl, H.P. Beck, G. Emig, Appl. Catal. (59) (1990) L1–7.

[40] S. Ruf, G. Emig, Pure dehydrogenation of methanol to formaldehyde a homogeneously sodium-catalysed vapour-phase reaction, Applied Catalysis A: General 161(1) (1997) L19–24. 10.1016/S0926-860X(97)00127-0.

[41] P. Zaza, H. Randall, R. Doepper, A. Renken, Dynamic kinetics of catalytic dehydrogenation of methanol to formaldehyde, Catalysis Today 20(3) (1994) 325–34. 10.1016/0920-5861(94)80129-0.

[42] M.K. Anke, Sodium, Elements and Their Compounds in the Environment, John Wiley & Sons, Ltd, 2004, pp. 497–519.

[43] A. Klemm, G. Hartmann, L. Lange, Sodium and Sodium Alloys, Ullmann's Encyclopedia of Industrial Chemistry, John Wiley & Sons, Ltd, 2000, p. .

[44] N. Greenwood, A. Earnshaw, Chemie der Elemente,1st ed., Verlag Chemie, Weinheim, Germany, 1988.

[45] Sodium Metal Market Size, Share, Growth, Forecast, 2032. Available at: https://www.businessresearchinsights.com/market-reports/sodium-metal-market-109163. Accessed August 15, 2024.

[46] Sodium - Chemical Properties, Reactions, Uses | Britannica. Available at: https://www.britannica.com/science/sodium/Chemical-properties. Accessed May 13, 2024.

[47] R. Maurer, Dehydrogenation of methanol to anyhdrous formaldeyhde using microsystems. Ecole Polytechnique Federale de Lausanne, 2001.

[48] W. M. Haynes, CRC Handbook of Chemistry and Physics 95th Edition, 2014

[49] H.U. Borgstedt, G. Frees, H. Schneider, Corrosion and Creep of Pressurized Stainless-Steel Tubes in Liquid Sodium at 873 and 973 K, Nuclear Technology 34(2) (1977) 290–8. 10.13182/NT77-A39703.

[50] Y. Dai, X. Zheng, P. Ding, Review on sodium corrosion evolution of nuclear-grade 316 stainless steel for sodium-cooled fast reactor applications, Nuclear Engineering and Technology 53(11) (2021) 3474–90. 10.1016/j.net.2021. 05.021.

[51] V. Ganesan, V. Ganesan, Corrosion of annealed AISI 316 stainless steel in sodium environment, Journal of Nuclear Materials 256(1) (1998) 69–77. 10.1016/S0022-3115(98)00041-5.

[52] M. Rivollier, J.-L. Courouau, M. Tabarant, C. Blanc, F. Jomard, M.-L. Giorgi, Further insights into the mechanisms involved in the corrosion of 316L(N) austenitic steel in oxygenated liquid sodium at 550 °C, Corrosion Science 165 (2020) 108399. 10.1016/j.corsci.2019.108399.

[53] J. Courouau, F. Balbaud Celerier, V. Lorentz, T. Dufrenoy, Corrosion by liquid sodium of materials for sodium fast reactors: the CORRONa testing device, 2011.

[54] A.W. Thorley, C. Tyzack, Corrosion and mass transport of steel and nickel alloys in sodium systems, 1973.

[55] W. Faes, S. Lecompte, Z.Y. Ahmed, J. Van Bael, R. Salenbien, K. Verbeken, M. De Paepe, Corrosion and corrosion prevention in heat exchangers, Corrosion Reviews 37(2) (2019) 131–55. 10.1515/corrrev-2018-0054.

[56] V.V. Alekseev, Y.A. Kuzina, A.P. Sorokin, Conceptual issues of the cold filter trap development for the sodium coolant purification in fast-neutron reactors, Nuclear Energy and Technology 6(2) (2020) 105–11. 10.3897/nucet.6.55220.

[57] Y. El-Kattan, J. McAtee, B. Bessieres, Sodium Methoxide, Encyclopedia of Reagents for Organic Synthesis, John Wiley & Sons, Ltd, 2006.

[58] S. Namwong, V. Punsuvon, Biodiesel Production from Used Vegetable Oil Using Ethanol and Sodium Methoxide Catalyst, KEM 723 (2016) 551–5. 10.4028/www.scientific.net/KEM.723.551.

[59] K. Chandran, M. Kamruddin, P.K. Ajikumar, A. Gopalan, V. Ganesan, Kinetics of thermal decomposition of sodium methoxide and ethoxide, Journal of Nuclear Materials 358(2) (2006) 111–28. 10.1016/j.jnucmat.2006.07.003.

[60] J.F.O. Granjo, N.M.C. Oliveira, Process Simulation and Techno-Economic Analysis of the Production of Sodium Methoxide, Ind. Eng. Chem. Res. 55(1) (2016) 156–67. 10.1021/acs.iecr.5b02022.

[61] C. Thieme, Sodium Carbonates, Ullmann's Encyclopedia of Industrial Chemistry, John Wiley & Sons, Ltd, 2000.

[62] T. Eggeman, Sodium Carbonate, Kirk-Othmer Encyclopedia of Chemical Technology, John Wiley & Sons, Ltd, 2011, pp. 1–11.

[63] S. Su, Catalytic dehydrogenation of methanol to formaldehyde on sodium carbonate. Swiss Federal Institute of Technology, Lausanne, 1991.

[64] J.-W. Kim, H.-G. Lee, Thermal and carbothermic decomposition of Na2CO3 and Li2CO3, Metallurgical and Materials Transactions B 32 (2001). 10.1007/s11663-001-0003-0.

[65] M. Sakr, S. Liu, A comprehensive review on applications of ohmic heating (OH), Renewable and Sustainable Energy Reviews 39 (2014) 262–9. 10.1016/j.rser.2014.07.061.

[66] N. Abas, A. Kalair, N. Khan, Review of fossil fuels and future energy technologies, Futures 69 (2015) 31–49. 10.1016/j.futures.2015.03.003.

[67] J. Li, M.C. Paul, P.L. Younger, I. Watson, M. Hossain, S. Welch, Characterization of biomass combustion at high temperatures based on an upgraded single particle model, Applied Energy 156 (2015) 749–55. 10.1016/j.apenergy.2015.04.027.

[68] L.D. Smoot, L.L. Baxter, Fossil Fuel Power Stations—Coal Utilization, in: R. A. Meyers (Ed.), Encyclopedia of Physical Science and Technology (Third Edition), Academic Press, New York, 2003, pp. 121–44.

[69] S. Lupi, Direct Resistance Heating, in: S. Lupi (Ed.), Fundamentals of Electroheat: Electrical Technologies for Process Heating, Springer International Publishing, Cham, 2017, pp. 287–352.

[70] B.-A. Behrens, S. Hübner, L. Albracht, E. Farahmand, Resistance Heating by Means of Direct Current for Resource-Saving CO_2-Neutral Hot Stamping, KEM 926 (2022) 2363–70. 10.4028/p-99k4fg.

[71] L. Astráin-Redín, S. Ospina, G. Cebrián, I. Álvarez-Lanzarote, Ohmic Heating Technology for Food Applications, From Ohmic Systems to Moderate Electric Fields and Pulsed Electric Fields, Food Eng Rev 16(2) (2024) 225–51. 10.1007/s12393-024-09368-4.

[72] N. Kaur, A.K. Singh, Ohmic Heating: Concept and Applications—A Review, Critical Reviews in Food Science and Nutrition 56(14) (2016) 2338–51. 10.1080/10408398.2013.835303.

[73] I. Eryazici, N. Ramesh, C. Villa, Electrification of the chemical industry—materials innovations for a lower carbon future, MRS Bulletin 46(12) (2021) 1197–204. 10.1557/s43577-021-00243-9.

[74] B. Dietrich, Thermische Charakterisierung von keramischen Schwammstrukturen für verfahrenstechnische Apparate. 10.5445/KSP/1000021167.

[75] B. Dietrich, Pressure drop correlation for ceramic and metal sponges, Chemical Engineering Science 74 (2012) 192–9. 10.1016/j.ces.2012.02.047.

[76] B. Dietrich, G. Schell, E.C. Bucharsky, R. Oberacker, M.J. Hoffmann, W. Schabel, M. Kind, H. Martin, Determination of the thermal properties of ceramic sponges, International Journal of Heat and Mass Transfer 53(1) (2010) 198–205. 10.1016/j.ijheatmasstransfer.2009.09.041.

[77] A. Ortona, S. Gianella, D. Gaia, SIC Foams for High Temperature Applications, Advances in Bioceramics and Porous Ceramics IV, John Wiley & Sons, Ltd, 2011, pp. 153–61.

[78] P. Colombo, Conventional and novel processing methods for cellular ceramics, Philos Trans A Math Phys Eng Sci 364(1838) (2006) 109–24. 10.1098/rsta.2005.1683.

[79] L.C. Hwa, S. Rajoo, A.M. Noor, N. Ahmad, M.B. Uday, Recent advances in 3D printing of porous ceramics: A review, Current Opinion in Solid State and Materials Science 21(6) (2017) 323–47. 10.1016/j.cossms.2017.08.002.

[80] I. Karakurt, L. Lin, 3D printing technologies: techniques, materials, and post-processing, Current Opinion in Chemical Engineering 28 (2020) 134–43. 10.1016/j.coche.2020.04.001.

[81] S. Meille, M. Lombardi, J. Chevalier, L. Montanaro, Mechanical properties of porous ceramics in compression: On the transition between elastic, brittle, and cellular behavior, Journal of the European Ceramic Society 32(15) (2012) 3959–67. 10.1016/j.jeurceramsoc.2012.05.006.

[82] Y. Katoh, L.L. Snead, Silicon carbide and its composites for nuclear applications – Historical overview, Journal of Nuclear Materials 526 (2019) 151849. 10.1016/j.jnucmat.2019.151849.

[83] L. Zheng, M. Ambrosetti, F. Zaio, A. Beretta, G. Groppi, E. Tronconi, Direct electrification of Rh/Al2O3 washcoated SiSiC foams for methane steam reforming: An experimental and modelling study, International Journal of Hydrogen Energy 48(39) (2023) 14681–96. 10.1016/j.ijhydene.2022.12.346.

[84] E. Meloni, E. Saraceno, M. Martino, A. Corrado, G. Iervolino, V. Palma, SiC-based structured catalysts for a high-efficiency electrified dry reforming of methane, Renewable Energy 211 (2023) 336–46. 10.1016/j.renene.2023.04.082.

[85] R. Röttenbacher, G. Willmann, SisiC — A Material for High Temperature Ceramic Heat Exchangers, in: Ceramics in Advanced Energy Technologies, Springer Netherlands, Dordrecht, 1984, pp. 231–49.

[86] G. Tuci, Y. Liu, A. Rossin, X. Guo, C. Pham, G. Giambastiani, C. Pham-Huu, Porous Silicon Carbide (SiC): A Chance for Improving Catalysts or Just Another Active-Phase Carrier?, Chem. Rev. 121(17) (2021) 10559–665. 10.1021/acs.chemrev.1c00269.

[87] T. Kumada, R. Ishiguro, Y. Kimachi, Diffusion Coefficients of Sodium Vapors in Argon and Helium, Nuclear Science and Engineering 70(1) (1979) 73–81. 10.13182/NSE79-A18929.

[88] T.G. Geißler, Methanpyrolyse in einem Flüssigmetall-Blasensäulenreaktor, Verlag Dr. Hut, 2017.

[89] R. Clift, J.R. Grace, M.E. Weber, Bubbles, Drops, and Particles, Courier Corporation, 2005.

[90] F.C. Johansen, R.V. Southwell, Flow through pipe orifices at low Reynolds numbers, Proceedings of the Royal Society of London. Series A, Containing Papers of a Mathematical and Physical Character 126(801) (1997) 231–45. 10.1098/rspa.1930.0004.

[91] L. Amaya-Bower, T. Lee, Single bubble rising dynamics for moderate Reynolds number using Lattice Boltzmann Method, Computers & Fluids 39(7) (2010) 1191–207. 10.1016/j.compfluid.2010.03.003.

[92] V. Roig, M. Roudet, F. Risso, A.-M. Billet, Dynamics of a high-Reynolds-number bubble rising within a thin gap, Journal of Fluid Mechanics 707 (2012) 444–66. 10.1017/jfm.2012.289.

[93] E.S. Gaddis, A. Vogelpohl, Bubble formation in quiescent liquids under constant flow conditions, Chemical Engineering Science 41(1) (1986) 97–105. 10.1016/0009-2509(86)85202-2.

[94] A. Cihan, M.Y. Corapcioglu, Effect of compressibility on the rise velocity of an air bubble in porous media, Water Resources Research 44(4) (2008). 10.1029/2006WR005415.

[95] H.D. Mendelson, The prediction of bubble terminal velocities from wave theory, AIChE Journal 13(2) (1967) 250–3. 10.1002/aic.690130213.

[96] E. Strumpf, Experimental study on rise velocities of single bubbles in liquid metal under the influence of strong horizontal magnetic fields in a flat vessel, International Journal of Multiphase Flow 97 (2017) 168–85. 10.1016/j.ijmultiphaseflow.2017.08.001.

[97] W. Zhang, M. Liu, D.Z. Zhu, N. Rajaratnam, Mean and Turbulent Bubble Velocities in Free Hydraulic Jumps for Small to Intermediate Froude Numbers, Journal of Hydraulic Engineering 140(11) (2014) 04014055. 10.1061/(ASCE)HY.1943-7900.0000924.

[98] G. Hanyang, G. Liejin, Modeling of bubble shape in horizontal and inclined tubes, Progress in Nuclear Energy 89 (2016) 88–101. 10.1016/j.pnucene.2016.02.011.

[99] V. Duke-Walker, B.J. Musick, J.A. McFarland, Experiments on the breakup and evaporation of small droplets at high Weber number, International Journal of Multiphase Flow 161 (2023) 104389. 10.1016/j.ijmultiphaseflow.2023.104389.

[100] G. Strotos, I. Malgarinos, N. Nikolopoulos, M. Gavaises, Predicting droplet deformation and breakup for moderate Weber numbers, International Journal of Multiphase Flow 85 (2016) 96–109. 10.1016/j.ijmultiphaseflow.2016.06.001.

[101] A. Riswanda, I. Pranoto, Deendarlianto, Indarto, T. Wibowo, Study on the effect of Weber Number to heat transfer of multiple droplets on hot stainless steel surface, MATEC Web Conf. 154 (2018) 01114. 10.1051/matecconf/201815401114.

[102] T. Haas, C. Schubert, M. Eickhoff, H. Pfeifer, A Review of Bubble Dynamics in Liquid Metals, Metals 11(4) (2021) 664. 10.3390/met11040664.

[103] N. Brauner, The prediction of dispersed flows boundaries in liquid–liquid and gas–liquid systems, International Journal of Multiphase Flow 27(5) (2001) 885–910. 10.1016/S0301-9322(00)00056-2.

[104] F.A. Kozlov, V.V. Alexeev, Yu.P. Kovalev, V.Ya. Kumaev, V.V. Matyuchin, E.A. Orlova, E.P. Pirogov, A.P. Sorokin, S.I. Shcherbakov, Studies validating a sodium purification system for fast reactors, At Energy 112(1) (2012) 21–8. 10.1007/s10512-012-9519-4.

[105] T. Dursun, C. Soutis, Recent developments in advanced aircraft aluminium alloys, Materials & Design (1980-2015) 56 (2014) 862–71. 10.1016/j.matdes.2013.12.002.

[106] F. Czerwinski, Thermal Stability of Aluminum Alloys, Materials (Basel) 13(15) (2020) 3441. 10.3390/ma13153441.

[107] S. Ebnesajjad, 4 - Surface and Material Characterization Techniques, in: S. Ebnesajjad (Ed.), Surface Treatment of Materials for Adhesion Bonding, William Andrew Publishing, Norwich, NY, 2006, pp. 43–75.

[108] J.O. Hill, THERMAL ANALYSIS | Temperature-Modulated Techniques, in: P. Worsfold, A. Townshend, C. Poole (Eds.), Encyclopedia of Analytical Science (Second Edition), Elsevier, Oxford, 2005, pp. 22–9.

[109] Encyclopedia of Physical Science and Technology - 3rd Edition. Available at: https://shop.elsevier.com/books/encyclopedia-of-physical-science-and-technology/meyers/978-0-08-091795-5. Accessed January 8, 2024.

[110] J.R.H. Ross, Chapter 5 - Catalytic Reactors and the Measurement of Catalytic Kinetics, in: J. R. H. Ross (Ed.), Heterogeneous Catalysis, Elsevier, Amsterdam, 2012, pp. 97–121.

[111] O. Levenspiel, Chemical Reaction Engineering, John Wiley & Sons, 1998.

[112] W. Wei, X. Cao, C. Tian, J. Zhang, The influence of Si distribution and content on the thermoelectric properties of SiC foam ceramics, Microporous and Mesoporous Materials 112(1) (2008) 521–5. 10.1016/j.micromeso.2007.10.032.

[113] M.S. Anwar, S.Z.A. Bukhari, J.-H. Ha, J. Lee, I.-H. Song, Y.-W. Kim, Controlling the electrical resistivity of porous silicon carbide ceramics and their applications: A review, International Journal of Applied Ceramic Technology 19(4) (2022) 1814–40. 10.1111/ijac.14034.

[114] C.J.M. Fletcher, C.N. Hinshelwood, The thermal decomposition of formaldehyde, Proceedings of the Royal Society of London. Series A, Containing Papers of a Mathematical and Physical Character 146(857) (1997) 357–62. 10.1098/rspa.1934.0160.

[115] D. Aronowitz, D.W. Naegeli, I. Glassman, Kinetics of the pyrolysis of methanol, J. Phys. Chem. 81(25) (1977) 2555–9. 10.1021/j100540a037.

[116] F. Eichner, Untersuchungen zur oxidativen Dehydrierung von Methanol zu Formaldehyd - Betrachtungen auf Katalysator- und Prozessebene. KIT-Bibliothek, Karlsruhe, 2024.

[117] Z. Dong, Z. Wen, F. Zhao, S. Kuhn, T. Noël, Scale-up of micro- and milli-reactors: An overview of strategies, design principles and applications, Chemical Engineering Science: X 10 (2021) 100097. 10.1016/j.cesx.2021.100097.

[118] M. Komiyama, Design and Preparation of Impregnated Catalysts, Catalysis Reviews 27(2) (1985) 341–72. 10.1080/01614948508064738.

[119] A. Lekhal, B.J. Glasser, J.G. Khinast, Impact of drying on the catalyst profile in supported impregnation catalysts, Chemical Engineering Science 56(15) (2001) 4473–87. 10.1016/S0009-2509(01)00120-8.

[120] Industrial Catalysis | Wiley Online Books. Available at: https://onlinelibrary.wiley.com/doi/book/10.1002/9783527684625. Accessed March 20, 2024.

[121] J.H. Scofield, Hartree-Slater subshell photoionization cross-sections at 1254 and 1487 eV, Journal of Electron Spectroscopy and Related Phenomena 8(2) (1976) 129–37. 10.1016/0368-2048(76)80015-1.

[122] A. Shchukarev, D. Korolkov, XPS Study of group IA carbonates, Open Chemistry 2(2) (2004) 347–62. 10.2478/BF02475578.

[123] T.P. Nguyen, S. Lefrant, XPS study of SiO thin films and SiO-metal interfaces, J. Phys.: Condens. Matter 1(31) (1989) 5197. 10.1088/0953-8984/1/31/019.

[124] A. Barrie, F.J. Street, An Auger and X-ray photoelectron spectroscopic study of sodium metal and sodium oxide, Journal of Electron Spectroscopy and Related Phenomena 7(1) (1975) 1–31. 10.1016/0368-2048(75)80052-1.

[125] X. Chen, X. Wang, D. Fang, A review on C1s XPS-spectra for some kinds of carbon materials, Fullerenes, Nanotubes and Carbon Nanostructures 28 (2020) 1–11. 10.1080/1536383X.2020.1794851.

[126] F.Y. Oliva, E.P.M. Leiva, G. Lener, D.E. Barraco, J.C. Trincavelli, Study of the spontaneous oxidation of sodium in air by EPMA and Monte Carlo simulations, Applied Surface Science 480 (2019) 1093–9. 10.1016/j.apsusc.2019.02.181.

[127] B. Dietrich, W. Schabel, M. Kind, H. Martin, Pressure drop measurements of ceramic sponges—Determining the hydraulic diameter, Chemical Engineering Science 64(16) (2009) 3633–40. 10.1016/j.ces.2009.05.005.

[128] J. Große, B. Dietrich, H. Martin, M. Kind, J. Vicente, E.H. Hardy, Volume Image Analysis of Ceramic Sponges, Chemical Engineering & Technology 31(2) (2008) 307–14. 10.1002/ceat.200700403.

[129] S. Meinicke, Understanding transport phenomena in consolidated, highly porous media – a pore-scale CFD approach. Karlsruher Instituts für Technologie, 2020.

9. APPENDIX

9.1 Measurement uncertainty

The studies conducted in this thesis are also subject to measurement uncertainties due to the experimental methods and equipment used. In this study, the most important measurement errors include those related to:

- Accuracy of used equipment: e.g. flow controllers, scale, thermocouples
- Fluid properties: purity, changes in volume, density and mass (in the case of sodium due to oxidation)
- Operator error: e.g. weighting procedure of evaporated sodium

Important information regarding key equipment is listed in Table 20.

Table 20. Accuracy of equipment

Equipment	Accuracy[3]	Short name
Gas flow controllers F-201CV-2K0-PGD-33-K	±0.5 %	(GFC)
Methanol flow controllers ML120V00-PGD-33-0-S-DA-000	±0.2 %	(MFC)
Scale BTG-303	±0.003 g	(m)
Thermoelement Typ K Classe 1 IEC 60584	±1,5 °C	(T)
Pressure controller P-502C-1K1R-PGD-39	±0.5 %	(PC)
Pressure indicator Rosemount 2051 In-Line Pressure Transmitter	±0.1 %	(p)

Gas chromatograph measurement

Determining the uncertainty of a gas chromatography (GC) analysis with a thermal conductivity detector (TCD), a methaniser and a flame ionization detector (FID) is a process involving several variables:

[3] Values form data sheet of manufactures

- Variability in the amount of sample introduced into the GC. A flow controller was used in order to provide a constant flow of 10 ml for the GC sampling loop. However, due to the changing composition of the gas, the measurement of the flow controller has lower accuracy
- Separation of the components on the columns (depending on the concentration of components)
- Detectors response (depending on the concentration of components)
- Accuracy of calibration standards and the linearity of the calibration curve
- Temperature and pressure fluctuations can affect gas flow rates and detector responses.

The standard uncertainty $u(y_i)$ of the measured molar fraction y of gas component is:

$$u(y_i)^2 = u(y_{i,rept})^2 + u(y_{i,lin})^2 + u(y_{i,cal})^2 \quad \text{Eq. 42}$$

where:

- $u(y_{i,rept})$ standard uncertainty due to repeatability
- $u(y_{i,lin})$ standard uncertainty due to linearity
- $y(_{i,cal})$ standard uncertainty due to calibration gas uncertainty

Composition of different mixtures entering the GC for 1 l min^{-1} are shown in Table 21:

Table 21. Composition of mixture I, II and III

Compound	Mass Fraction		
	Mixture I	Mixture II	Mixture III
Argon	0.80	0.90	0.80
Hydrogen	0.04	0.02	0.05
Carbon monoxide	0.04	0.02	0.05
Carbon dioxide	0.01	0.00	0.00
Methanol	0.03	0.02	0.10
Methane	0.01	0.00	0.00
Formaldehyde	0.07	0.04	0.00

Calculated properties for the mixtures of 1 l min^{-1} at 140 ^{o}C and 1.2 bar are presented in Table 22.

Table 22. Calculated properties for the example mixtures entering the GC

	Mass flow, kg hr^{-1}	Density, kg m^{-3}	Thermal conductivity, W m^{-1} K^{-1}	Viscosity, cP
Mixture I	0.046	0.767	0.087	0.025
Mixture II	0.059	0.995	0.061	0.027
Mixture III	0.042	0.704	0.097	0.024

From the provided example calculations, it can be seen that the higher level of uncertainty must be considered for the flow controller placed in front of the gas chromatograph. This is the result of variations in flow characteristics due to differences in composition and volume introduced into the gas chromatography column.

Total uncertainty of dehydrogenation of methanol tests

Total uncertainty $u(t)$ is calculated as a sum of uncertainties of temperature, pressure flow and GC measurements, it is as follows:

$$\mathrm{u(t)}^2 = \mathrm{u(T)}^2 + \mathrm{u(p)}^2 + \mathrm{u(GC)}^2 + \mathrm{u(FC)}^2 \quad \text{Eq. 43}$$

where:

- $\mathrm{u(T)}$ standard uncertainty due to total temperature measurement uncertainty (1.72 %)
- $\mathrm{u(p)}$ standard uncertainty due to total pressure measurement uncertainty (0.22 %)
- $\mathrm{u(GC)}$ standard uncertainty due to total GC measurement uncertainty (8.5 % & 14 %)
- $\mathrm{u(FC)}$ standard uncertainty due to total flow measurement uncertainty (3.5 % & 5.5 %)

The total uncertainty of dehydrogenation of methanol tests was estimated to be ±10% with a confidence level of 95% and for the trials with the higher methanol content in the stream (≥15 mol%) the total uncertainty was determined to be ±15% with a confidence level of 95%.

Total uncertainty of sodium evaporation and condensation tests

Total uncertainty u(t) is calculated as the sum of uncertainties of weight, temperature, pressure, flow measurement, oxidation rate and operator error. It is as follows:

$$u(t)^2 = u(m)^2 + u(T)^2 + u(p)^2 + u(OR)^2 + u(FC)^2 + u(OE)^2 \quad \text{Eq. 44}$$

where:

- $u(m)$ standard uncertainty due to weight measurement uncertainty (0.10 %)
- $u(T)$ standard uncertainty due to total temperature measurement uncertainty (0.82 %)
- $u(p)$ standard uncertainty due to total pressure measurement uncertainty (0.12 %)
- $u(OR)$ standard uncertainty due to oxidation rate of sodium uncertainty (ca. 0.64 %)
- $u(FC)$ standard uncertainty due to total flow measurement uncertainty (1.3 %)
- $u(OE)$ standard uncertainty due to total operator error uncertainty (5.0 %)

Sodium reacts rapidly with air due to its reaction with the oxygen and moisture present in the atmosphere. Therefore its change of mass was possible during the weighting procedure. This is why it was crucial to determine the measurement uncertainty due to the oxidation of sodium. The oxidation rate was studied by Oliva et al [126]. Their simulations showed that sodium oxidation in atmospheric air proceeds in two stages:

1. Na_2O formation is indicated by a linear growth rate of $2 \cdot 10^{-5}$ cm s^{-1}, from 0 until 6.5 s
2. Na_2O_2 formation from 6.5 s characterized by a diffusion coefficient of oxygen in the peroxide phase of the order of $1 \cdot 10^{-9}$ cm^2

Based on these equations the estimated mass growth for 1 cm^3 of sodium is ca. 0.001425 g for 6.5 s.

In the case of total operator error, two factors were taken into account: the different total time taken to transfer the sample from the condenser to the balance to the scale (average time 5 – 10 s) and the possibility of some sodium materials remaining in the pipes of the condenser.

The total uncertainty of sodium evaporation and condensation tests was estimated to be ±10 % with a confidence level of 95 %.

9.2 Heat demand analysis for direct resistance setup

This section presents a simulation conducted in Aspen Plus V14, with a focus on the net heat duty values based on MEDENA mini-plant with the DRH reactor concept. The graphical representation of the simulation is shown in Figure 42. It illustrates the heating and chemical reaction of CH_3OH in the presence of Ar, a non-reactive gas. The simulation considers only the main components, namely CH_3OH, CH_2O, CO and H_2.

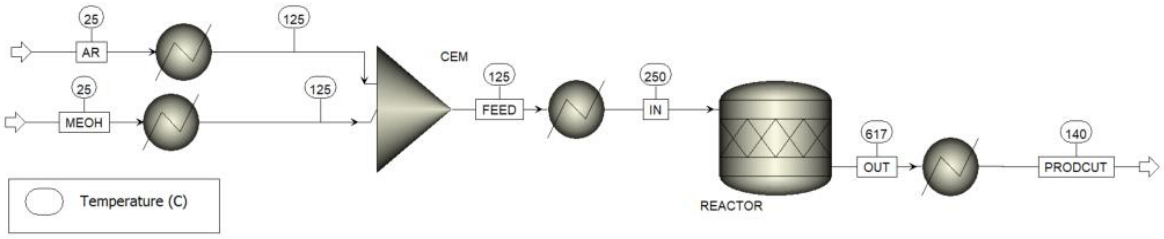

Figure 42. The DRH simulation scheme in Aspen Plus

A detailed description of the process shown in the diagram is given:

1. Ar (161 g h^{-1}) and CH_3OH (12 g h^{-1}) are introduced into the system at a starting temperature of 25 °C.
2. Both streams are preheated separately to 125 °C.
3. After preheating, the argon and methanol streams are mixed in the CEM.
4. The combined stream is then further heated to 250 °C before entering the reactor.
5. The reactor operates at a temperature of 617 °C and pressure of 1.3 bar where the chemical reaction takes place, converting the methanol into other chemical products.
6. The output from the reactor is cooled from 617 °C to 140 °C before leaving the system as the final product.

The simulation was set based on the results of the experiment (no. 1) shown in Table 14, the detailed results are as follows:

- Power = 245 W
- Mean reaction temperature = 617 °C
- Conversion of methanol = 99 %
- Yield of formaldehyde = 53 %

To approximate actual results, the stoichiometric reactor was used with methanol and formaldehyde fractional conversions set at 99% and 0.45, respectively, as shown in Figure 43:

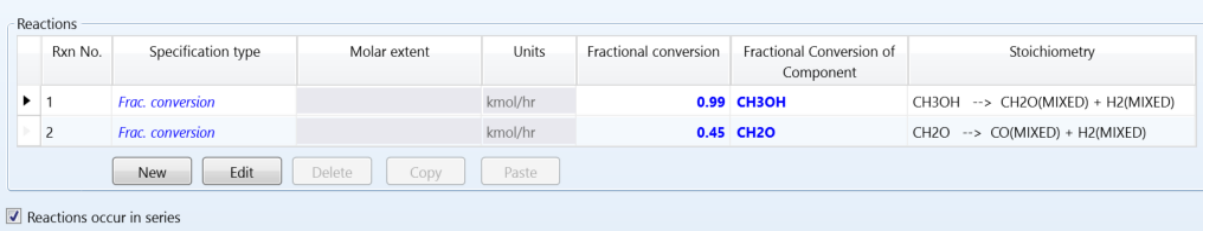

Figure 43. Results of the stoichiometric reactor in Aspen Plus

The heat of reaction for given conditions as well as reaction extent were calculated and are shown in Figure 44.

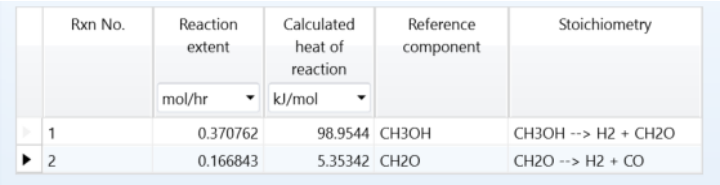

Figure 44. Calculated heat of reactions in Aspen Plus

The total heat demand of the reactor (heating the reactants and for the reaction itself) is 33 W, as indicated in Table 23.

Table 23. The net heat duty for the DRH system

Temperature °C	Net heat duty, W					
	Argon	Methanol	Feed	Reactor	Reaction	Cooling
25–125	2.3	4.4	-	-	-	-
125–250	-	-	3.6	-	-	-
250–617	-	-	-	22.6	-	-
617					10.4	
617–140	-	-	-	-	-	-15.3

The total heat demand of the reactor (heating the reactants and the reaction itself) is 33 W. The heat generated by the DRH reactor is 245 W. From this energy analysis it can be seen that only about 14% is used for heating the reactants and producing formaldehyde. Since the sponge is the only heating medium for the entire reactor (described in Section 2.5), approximately 338 W are required to raise the temperature of the reactor from 25 °C to 619 °C in one hour, assuming no losses to the environment. It can therefore be concluded that most of the heat is used to maintain the temperature in the reactor and that heat loss by radiation can be significant. In

addition, heat loss can be minimized by using materials with better thermal properties for reactor insulation. For the larger reactors, a heat recovery system should be used due to the necessity of cooling the product.

9.3 Pressure drop in the direct resistance heating setup

In systems where ceramic sponges are used, such as burners and catalytic reactors, accurate prediction of pressure drop is critical to achieving optimum operating efficiency [75]. Sponges, made from materials such as alumina or silicon carbide, present specific challenges due to their complex porous structures that can significantly affect fluid dynamics. In this section, a brief comparison of some mean experimental data with available computational methods is presented. The pressure drop is determined as the average of the difference between the pressure readings in front of and behind the reactor. The results are shown in Table 24.

Table 24. Pressure drop in the DRH reactor

Total flow	Pressure drop, barg	
l min^{-1}	Conventional sponge	3D-printed sponge
1.4	0.007	0.011
1.7	n/a	0.041
2.1	0.008	n/a
2.2	n/a	0.081

Dietrich et al. [127] developed a correlation to predict fluid behavior in open-cell foams under varying operational conditions. They adapted an Ergun-type approach to address the characteristics of these materials. The resulting correlation was derived by minimizing the square of errors across more than 400 experimental data points. The specific formula (Eq. 45) provided is as follows:

$$\frac{\Delta p}{\Delta L} = 110 \cdot \frac{\eta}{\psi d_h^2} \cdot u + 1.45 \cdot \frac{\rho}{\psi^2 d_h} \cdot u^2 \qquad \text{Eq. 45}$$

where ψ is total porosity and d_h hydraulic diameter.

The hydraulic diameter formula is the specific surface area per unit volume (Eq. 46):

$$d_h = 4\frac{\psi}{S_v} \qquad \text{Eq. 46}$$

This specific surface area, which is crucial for characterization of the sponge structure, can be accurately measured using imaging techniques such as computer tomography (CT) scans or magnetic resonance imaging (MRI), as described by Große et al [128]. The conventional sponge had values of 0.84 for porosity and ca. 1000 m^{-1} for surface area, whereas the 3D-printed sponge showed 0.75 and ca. 1450 m^{-1} respectively. The calculated pressure drop values are shown in Table 25.

Table 25. Calculated pressure drop values

Total flow	**Pressure drop, barg**	
l min^{-1}	**Conventional sponge**	**3D-printed sponge**
1.4	0.0011	0.005
1.7	n/a	0.007
2.1	0.0016	n/a
2.2	n/a	0.008

The 3D-printed sponge, which has a Voronoi lattice structure, exhibits a higher pressure drop than calculated. This can be primarily attributed to the amount of catalyst that was used. Typically, lattice structure SiSiC sponges have lower pressure drop values in comparison to standard 20 PPI SiSiC sponges [129]. This is attributed to the lattice structure which has more efficient layout and enhances fluid dynamics through the sponge. This design reduces flow resistance and improves the streamline of the flow through the porous medium, effectively decreasing the pressure drop across the structure.

10. LIST OF FIGURES

11. LIST OF TABLES

Bachelor thesis supervised at ITES related to this work

- D. Mertens, “Determination of the flow properties in the reactors used in the process of direct dehydrogenation of methanol to formaldehyde,” Bachelor Thesis, KIT, 2022.

Publication and patent within the framework of this study

- Kamienowska, M., Deutschmann, M.P., Bender, M., Stoppel, L., Daubner, M., Wetzel, T. and Niedermeier, K. (2024), Experimental Demonstration of the Production of Hydrogen and Water-Free Formaldehyde Using Sodium Vapor. Chemie Ingenieur Technik. https://doi.org/10.1002/cite.202400007
- Submission for European Patent no. PF230711 (230711WO01, PCT/EP2024/083548), titled: Catalyst body for anhydrous formaldehyde production (with 59% share, other inventors Dr Michael Bender, BASF, Dr.-Ing. Klarissa Niedermeier, Prof. Dr.-Ing. Thomas Wetzel, Peter Miodek, Daniel Kuntz, Joachim Konrad and Christoph Hofberger (all KIT))

Presentations at conferences within the framework of this study

1. Poster-Presentation: Annual Meeting of ProcessNet the Subject Division Heat and Mass Transfer, Erfurt, 12-13 March 2020: Synthesis of anhydrous formaldehyde, M. Kamienowska, L. Stoppel, K. Niedermeier, M. Bender, T. Wetzel
2. Poster-Presentation: 13th European Congress of Chemical Engineering (ECCE 13) and 6th European Congress of Applied Biotechnology (ECAB 6), online, 20-23 September 2021: Experimental setup for the production of formaldehyde using sodium vapour, M. Kamienowska, K. Niedermeier, L. Stoppel, M. Bender, T. Wetzel
3. Poster-Presentation, Annual Meeting on Reaction Engineering and ProcessNet Subject Division Heat and Mass Transfer 2022, 18-20 January 2022, Würzburg: Development of Sodium Catalyst Dosing Method for Water-Free Formaldehyde Production, M. Kamienowska, K. Niedermeier, M. Daubner. L. Stoppel, M. Bender, T. Wetzel.
4. Poster-Presentation, The Role of Catalysis for the Energy-Transition, DGMK Conference 5-7 October 2022, Ludwigshafen: Production of anhydrous formaldehyde with co-generation of hydrogen, M. Kamienowska, K. Niedermeier, M. Bender, T. Wetzel.